

**DIAGNOSTIC STUDIES OF EXTRATROPICAL INTRASEASONAL
VARIABILITY IN THE NORTHERN HEMISPHERE**

A Thesis
Presented to
The Academic Faculty

by

Dennis P. Robinson

In Partial Fulfillment
of the Requirements for the Degree
Doctor of Philosophy in the
School of Earth and Atmospheric Sciences

Georgia Institute of Technology
May 2006

COPYRIGHT © 2006 BY DENNIS P. ROBINSON

**DIAGNOSTIC STUDIES OF EXTRATROPICAL INTRASEASONAL
VARIABILITY IN THE NORTHERN HEMISPHERE**

Approved by:

Dr. Robert X. Black, Advisor
School of Earth and Atmospheric Sciences
Georgia Institute of Technology

Dr. Rong Fu
School of Earth and Atmospheric
Sciences
Georgia Institute of Technology

Dr. Derek M. Cunnold
School of Earth and Atmospheric Sciences
Georgia Institute of Technology

Dr. John A. Knox
Department of Biological and
Agricultural Engineering
University of Georgia

Dr. Robert E. Dickinson
School of Earth and Atmospheric Sciences
Georgia Institute of Technology

Date Approved: March 30, 2006

This one is for you, Allison. We made it!

ACKNOWLEDGEMENTS

With the exception of this section in the thesis, I never use first-person, because reaching this point would not have been possible without the help of others. I would like to thank my advisor, Rob Black. I can not express how much I appreciate his support over the last six years. He provided a perfect balance of freedom and guidance during the course of my study. I thank my office mate, Brent McDaniel. From untangling computer snags to discussing scientific issues, Brent was there for me on several occasions. I appreciate the support from the other members of my reading committee: Drs. Bob Dickinson, Rong Fu, John Knox, and Derek Cunnold. I would also like to acknowledge the countless people responsible developing the GCMs used in this study. These models served as a framework for enhancing my graduate education.

I thank my fellow graduate students for their empathy and humor through graduate school, especially some of my close pals: Brent McDaniel, Benton Whitesides, Ray Mooring, Ping Jing, Kari and Joe Meier, Jim and Janine Captain, Lauren and Evan Schwimmer, Rick Peltier, Amy Sullivan, Nathan Schlientz, Colin Thomas, Rob Snodgrass, Brian Cafaro, and Daniel Arnett. Soccer, bowling, softball and several other sports, poker nights, weddings, road trips, and just hanging around, I think about my time with everyone at Georgia Tech, and the memories bring a smile to my face.

Reaching this point in my life would not have been possible without the unconditional love of my parents. I thank them and the rest of my family for always being there for me: Mike, Joe, Wendy, Bruce, Ashley, and Mary.

I especially treasure the support, inspiration, and patience from the love of my life, Allison. She is a blessing to me.

TABLE OF CONTENTS

DEDICATION	iii
ACKNOWLEDGEMENTS	iv
LIST OF TABLES	vii
LIST OF FIGURES	ix
SUMMARY	xiii
I BACKGROUND	1
1.1 Introduction	1
1.2 Midlatitude subseasonal variability	3
1.2.1 Synoptic eddies, storm tracks, and baroclinic development	3
1.2.2 Midwinter suppression	5
1.2.3 Large-scale weather regimes	7
1.3 Subseasonal variability and GCMs	8
1.4 Summary	9
II DATASETS AND GENERAL METHODOLOGY	11
2.1 Observational datasets	11
2.2 Model datasets	11
2.3 Characterizing subseasonal variability	12
2.4 Barotropic dynamical diagnostics	14
2.5 Baroclinic dynamical diagnostics	15
III COMPARATIVE STUDY OF MIDLATITUDE SUBSEASONAL VARIABILITY: STATISTICS AND STRUCTURES	16
3.1 Winter Mean Circulation	16
3.2 Climatological Storm Tracks	18
3.2.1 Synoptic Eddy Diagnostics	18
3.2.2 Midwinter Suppression	25
3.3 Large-scale weather regimes	27
3.3.1 North Pacific composites	30
3.3.2 North Atlantic composites	39

3.4	Summary	46
IV	COMPARATIVE STUDY OF BAROCLINIC DEVELOPMENT	48
4.1	Methodology	49
4.2	Winter mean characteristics	50
4.3	Seasonal stratification	60
4.4	Summary	68
V	DIAGNOSES OF THE NORTH PACIFIC MIDWINTER SUPPRESSION	70
5.1	Methodology	70
5.2	Lag regression analyses	72
5.3	Statistical analyses	82
5.3.1	Monte Carlo testing	82
5.3.2	Upstream Siberian indices	83
5.4	Summary	90
VI	CONCLUSION AND CLOSING REMARKS	96
	REFERENCES	101

LIST OF TABLES

1	Average energy conversions for (a) anticyclonic and (b) cyclonic Pacific persistent flow anomalies for the NCEP-NCAR reanalyses and NASCAR and NSIPP models. Each values is time-averaged during the maintenance phases of the PFAs and areally-averaged from 20°N–90°N, 160°E–280°E.	36
2	Average (a) baroclinic energy conversions at 700 <i>hPa</i> and (b) barotropic energy conversions at 300 <i>hPa</i> for the composite anticyclonic PFAs for the NCEP-NCAR reanalyses, NASCAR and NSIPP models, and the swapped energy conversions.	37
3	Same as Table 2 except for Pacific cyclonic PFA cases.	37
4	The winter-mean, areally-average (a) 700 <i>hPa</i> baroclinic and (b) 300 <i>hPa</i> barotropic energy conversions for Pacific cyclonic cases at Day –1 for the NCEP-NCAR reanalyses, NASCAR and NSIPP models, and the swapped energy conversions. The averaging region for the Pacific cases is 20°N–60°N, 110°E–230°E.	58
5	As in Table 4 except for Pacific anticyclonic cases.	59
6	The winter-mean, areally-average (a) 700 <i>hPa</i> baroclinic and (b) 300 <i>hPa</i> barotropic energy conversions for Atlantic cyclonic cases at Day –1 for the NCEP-NCAR reanalyses, NASCAR and NSIPP models, and the swapped energy conversions. The averaging region for the Atlantic cases is 30°N–70°N, 240°E–360°E.	60
7	As in Table 6 except for Atlantic anticyclonic cases.	61
8	The left column lists selected percentiles of the area coverage (units: m^2) of significance derived from 1000 random cases. For each random case, the magnitude of mature cyclonic events in the Pacific storm track core during midwinter are regressed onto the unfiltered geopotential height anomaly field over Asia for randomly selected days. The right column lists the area coverage and associated percentile derived from regressing the events onto the unfiltered height field over Asia at 7 days preceding the event.	83
9	The area coverage and percentile of significant regions derived from a Monte Carlo technique during EL and MW at 7, 5, and 3 days preceding strong cyclonic events in the core of the storm track associated with regressions onto the (a) unfiltered, (b) highpass-filtered, and (c) lowpass-filtered geopotential height anomaly field over Asia.	84

10 Monte Carlo results during EL and MW for the value of the (a) P2 and (b) E2 indices for selected lags from days with anomalously enhanced levels of baroclinic wave activity. The percentiles are compiled from 1000 cases of hypothesis testing, where the null hypothesis assumes no difference between the selected mean and a random sample mean of the indices. The null hypothesis is rejected with 99% confidence and the percentile represents the percent of cases in which the null hypothesis is rejected. 89

LIST OF FIGURES

1	The climatological zonal wind (shading: $m \cdot sec^{-1}$) and stationary wave field (contour intervals: 50 m) at 300 hPa for (a) NCEP-NCAR reanalysis, and (b) NASCAR and (c) NSIPP models. The climatologies are derived from the AMIP-II time period for the 90-day winter (DJF).	17
2	Vertical profiles of the areal-averaged eddy kinetic energy for each dataset derived from (a) unfiltered, (b) high-pass filtered, and (c) low-pass filtered anomalies. The averaging region includes all grid points north of 20°N. . .	19
3	The rms high-pass filtered geopotential height anomalies (shaded regions: units m) superposed on the climatological height field (contour intervals: 200 m) at 300 hPa for (a) NCEP-NCAR reanalyses and (b) NASCAR and (c) NSIPP GCMs. The E vectors associated with the 300 hPa HP eddies are plotted for each dataset with a scale vector provided. The threshold vector length is $15 m^2 \cdot sec^{-2}$	21
4	The height anomaly field regressed onto the time series of the 500 hPa HP-filtered meridional wind anomaly at 42°N, 170°W. The regressed height field (contour intervals: 10 m) at 500 hPa is displayed for the (a) NCEP-NCAR reanalyses and (b) NASCAR and (c) NSIPP models. (d)-(f) The vertical cross sections of the regressed height field at 42°N for each respective dataset. Positive values are darkly shaded, and negative values are lightly shaded. .	23
5	The height anomaly field regressed onto the time series of the 500 hPa HP-filtered meridional wind anomaly at 48°N, 305°W. The regressed height field (contour intervals: 10 m) at 500 hPa is displayed for the (a) NCEP-NCAR reanalyses and (b) NASCAR and (c) NSIPP models. (d)-(f) The vertical cross sections of the regressed height field at 48°N for each respective dataset. Positive values are darkly shaded, and negative values are lightly shaded. .	24
6	Synoptic eddy heat flux vectors (units: $K \cdot m \cdot sec^{-1}$) superposed on the climatological temperature field (contour intervals: 5 K) at 700 hPa for (a) NCEP-NCAR reanalyses and (b) NASCAR and (c) NSIPP models. A scale vector is provided for the eddy heat flux. Gray shaded regions mark the winter-averaged baroclinic energy conversions greater than $5 \times 10^{-5} K^2 \cdot sec^{-1}$	26
7	The annual cycle of the climatological average 300 hPa rms of the envelope function (shaded contour intervals: 15 m) longitudinally averaged across the core region of the (a)-(c) Pacific storm tracks and (d)-(f) Atlantic storm tracks for the NCEP-NCAR reanalyses and NASCAR and NSIPP models, respectively. A vertical axis marking 1-Jan is plotted.	28
8	The regional frequency distribution (shading units: number of events per AMIP-2 period) of persistent flow anomalies at 500 hPa for (a) NCEP-NCAR reanalyses and (b) NASCAR and (c) NSIPP models. Events are selected using a 10 day, 100 m anomaly threshold. The key points marking the highest frequency of events are marked with an "X".	29

9	The difference in the total number of PFA events between the NCEP-NCAR reanalyses and (a) NASCAR and (b) NSIPP models (contour intervals: 3 cases per AMIP-2 period). Light (dark) shading indicates regions where the model exhibits positive (negative) biases that are significant at the 95% confidence level.	30
10	The composite height anomalies at 300 <i>hPa</i> (contour interval: 30 <i>m</i>) and 1000 <i>hPa</i> (color shaded regions) for anticyclonic PFA cases over the Pacific key region of the (a) NCEP-NCAR reanalyses and (b) NASCAR and (c) NSIPP models.	32
11	Same as Figure 10 except for Pacific cyclonic PFA cases.	33
12	(a)-(c) Heat flux vectors (units: $K \cdot m \cdot s^{-1}$) overlaying the winter-averaged temperature field (contour intervals: 5 K) at 700 <i>hPa</i> and (d)-(f) E_{LP} vectors (units: $m^2 \cdot s^{-2}$) overlaying the winter-averaged zonal wind field (threshold: 25 $m \cdot s^{-1}$; contour intervals: 5 $m \cdot s^{-1}$) at 300 <i>hPa</i> computed from the anticyclonic Pacific PFAs for the NCEP-NCAR reanalyses and NASCAR and NSIPP models, respectively. Scale vectors are provided. Regions with baroclinic (barotropic) conversions greater than $1 \times 10^{-4} m^2 \cdot s^{-3}$ ($3 \times 10^{-3} K^2 \cdot s^{-1}$) are shaded in gray.	34
13	Same as Figure 12 except for Pacific cyclonic PFA cases.	35
14	Same as Figure 10 except for Atlantic anticyclonic PFA cases.	41
15	Same as Figure 12 except for Atlantic anticyclonic PFA cases.	42
16	Same as Figure 10 except for Atlantic cyclonic PFA cases.	44
17	Same as Figure 12 except for Atlantic cyclonic PFA cases.	45
18	Composite height anomalies at 300 <i>hPa</i> (contour interval: 30 <i>m</i>) and 1000 <i>hPa</i> (color shaded regions) for (a) anticyclonic and (b) cyclonic PFA cases at the point 42.5°N, 42.5°W for NCEP-NCAR reanalyses. The key point used for the original composite of Atlantic PFAs in the reanalyses is 52.5°N, 25.5°W.	46
19	Vertical profiles of the areally-averaged eddy kinetic energy for each dataset derived from the winter-averaged unfiltered anomalies for (a) Pacific cyclonic, (b) Pacific anticyclonic, (c) Atlantic cyclonic, and (d) Atlantic anticyclonic cases. The averaging region is 20°N–60°N, 110°E–230°E for the Pacific cases and 30°N–70°N, 240°E–360°E for the Atlantic cases.	51
20	Winter-averaged composite height anomalies at 300 <i>hPa</i> (contour intervals: 20 <i>m</i>) and 700 <i>hPa</i> [orange (blue) shaded regions greater (less) than 20 (–20) <i>m</i> at 20 <i>m</i> intervals] for Pacific cyclonic cases at Day –1 for the (a) NCEP-NCAR reanalyses and (b) NASCAR and (c) NSIPP models. Day 0 is defined as when the synoptic eddies are at maximum amplitude in the core of the regional storm track.	53
21	As in Figure 20 except for Pacific anticyclonic cases.	54
22	As in Figure 20 except for Atlantic cyclonic cases.	56

23	As in Figure 20 except for Atlantic anticyclonic cases.	57
24	Composite height anomalies at 300 <i>hPa</i> (contour intervals: 20 <i>m</i>) and 700 <i>hPa</i> [orange (blue) shaded regions greater (less) than 20 <i>m</i> (–20) at 20 <i>m</i> intervals] for Pacific cyclonic cases at Day –1 for the NCEP-NCAR reanalyses during the (a) early, (b) middle, and (c) late stage of the northern Pacific cool season. The early stage is taken to be November and December, midwinter is taken to be January and February, and late stage is taken to be March and April.	63
25	As in Figure 24 except for the NASCAR model.	64
26	As in Figure 24 except for the NSIPP model.	66
27	The rms highpass-filtered geopotential height anomalies for the winter average (contour intervals: 10 <i>m</i>) and the difference between the midwinter period and an average of the early and late periods (blue shaded regions: units <i>m</i>) at 300 <i>hPa</i> during the Pacific cool season for the (a) NCEP-NCAR reanalyses, (b) NASCAR dataset, (c) NSIPP dataset, and (d) during the Atlantic cool season for the NSIPP model. The early stage of the Atlantic cool season is taken as December through 15–January, midwinter 16–January through Feb., and late stage March through 15–April.	67
28	The annual cycle of the climatological-average of (a) the 500 <i>hPa</i> Eady parameter longitudinally averaged across the baroclinic region of the Pacific storm track and (b) the 300 <i>hPa</i> envelope function longitudinally averaged across the zonal extent of the North Pacific storm track. A vertical axis marking 1–January is plotted.	71
29	Regressed intraseasonal height anomalies (contour intervals: 20 <i>m</i>) at 300 <i>hPa</i> for Day –7 for (a) the average of the early and late stages and (b) the middle stage of the North Pacific cool season. Positive (negative) height anomalies significant at the 95% confidence level are shaded in orange (blue), which is based on a two-tailed Student’s <i>t</i> -test derived from 300 cyclonic events for <i>each</i> stage). The ageostrophic flux vectors are plotted and a scale vector provided.	74
30	As in Figure 29 except for Day –5.	75
31	As in Figure 29 except for Day –3. The cyclone positioned at 130°E propagates to the core point of the Pacific storm track by Day 0.	76
32	As in Figure 29 except for regressed lowpass height anomalies at Day –7.	78
33	As in Figure 29 except for regressed lowpass height anomalies at Day –5.	79
34	As in Figure 29 except for regressed lowpass height anomalies at Day –3.	80
35	The rms highpass-filtered geopotential height anomalies for the DJF average (contour intervals: 10 <i>m</i>) and the difference between the middle period and an average of the early and late periods (color shaded regions: units <i>m</i>) at 300 <i>hPa</i> . Shaded regions less than zero signify a decrease in the standard deviation of high-frequency eddies during midwinter.	81

36	The first two EOF patterns of the 300 <i>hPa</i> geopotential height anomalies (shaded contour intervals: 30 <i>m</i>) over Asia for (a)–(b) EL and (c)–(d) MW. The percent variance associated with each EOF pattern is provided.	86
37	The probability distribution function of the standardized highpass-filtered geopotential height anomaly in the core of the Pacific storm track for 5–8 days after positive (blue line with diamonds) and negative (red line) values of the PS index for (a) EL and (b) MW. The PS index is derived by projecting the Day –7 low-frequency pattern in Figure 32b onto the unfiltered geopotential height anomaly field over Asia.	91
38	As in Figure 37 but for the E2 index. The E2 index is derived from the second EOF of unfiltered geopotential height anomaly over Asia.	92
39	A histogram representing each days when the envelope function anomaly in the core of the MW storm track is greater than zero distributed over values of the PS index preceding the events by one week. The red curve represents a least-squares Gaussian fit to the histogram of the PS index based upon randomly selected dates. A null hypothesis (H_o) is defined as no difference between the mean of the two curves. In this case, the null hypothesis is rejected ($H_o = 1$) with 99% confidence (significance ; 0.01). The sample mean and 99% confidence levels are listed.	93
40	Composite maps of the 300 <i>hPa</i> envelope function anomaly (shaded contour intervals: $10^3 m^2$ during EL (left column) and MW (right column) for values of the P2 index values (a)–(b) $\geq 1\sigma$, (c)–(d) $\leq -1\sigma$, and (e)–(f) between $\pm 1\sigma$. For reference, core values of the Pacific storm track are approximately $140 \times 10^3 m^2$ depending on the stage of the cool season.	94
41	As in Figure 40 except for the E2 index.	95

SUMMARY

A comprehensive analysis of midlatitude intraseasonal variability in extended integrations of NASA GSFC General Circulation Models (GCMs) is conducted in the first part of this thesis. This is approached by performing a detailed intercomparison of the representation of the storm tracks and anomalous weather regimes occurring during wintertime in the (Atmospheric Model Intercomparison Project) AMIP-type simulations in both the NASA/NCAR (NASCAR) and a version of the Aries model used in NASA's Seasonal-to-Interannual Prediction Project (NSIPP) models. The statistics, three-dimensional structure, and dynamical characteristics of such intraseasonal phenomena are diagnosed and directly compared to parallel observational analyses.

Results indicate that several aspects of simulated intraseasonal phenomenon are linked to errors in the zonally asymmetric circulation. Discrepancies are observed in the magnitude and location of the planetary stationary waves and climatological jet streams. In both models, the Pacific stationary ridge is shifted westward relative to observations with a corresponding upstream shift in the location of the Pacific jet exit region. Furthermore, this feature is anomalously strong (weak) in the NSIPP (NASCAR) simulation. Over the Atlantic region, the stationary ridges are well positioned but anomalously strong (weak) in the NASCAR (NSIPP) model. For the NASCAR model, the magnitude of the maximum zonal wind in the jet core regions are slightly larger than observations, while the local zonal wind maxima in the NSIPP model are typically $5\text{--}10 \text{ m} \cdot \text{sec}^{-1}$ greater in the core of the Pacific and Atlantic jets.

Profiles of the areally-averaged eddy kinetic energy indicate that levels of subseasonal eddy activity in the GCMs are relatively weak throughout the mid to upper troposphere, particularly for synoptic-scale eddies. These deficiencies in subweekly fluctuations are also reflected in the magnitude of the simulated storm tracks, especially over the Pacific region. Composite studies of large-scale weather regimes indicate that low-frequency variability

in the Pacific jet exit region in the GCMs are more strongly driven by baroclinic dynamics. The westward displacement of the barotropic deformation zones in the Pacific jet exit region in the models is identified as one factor leading to the anomalously weak barotropic conversions.

Despite anomalously weak storm tracks, the GCMs successfully reproduce the North Pacific midwinter suppression, while the NSIPP produces a midwinter suppression over the Atlantic storm track region. The anomalously strong Atlantic jet stream in the NSIPP model exceeds $45 \text{ m} \cdot \text{sec}^{-1}$, the threshold beyond which synoptic eddy activity becomes suppressed. Since the GCMs reproduce the observed relationship between synoptic eddy activity and the upper-tropospheric zonal wind threshold, we posit that the anomalously weak storm tracks in the models are attributed to relatively extended periods throughout winter when upper-tropospheric wind speeds exceed $45 \text{ m} \cdot \text{sec}^{-1}$.

The second portion of this work employs a novel method towards studying aspects of the North Pacific midwinter suppression phenomenon. The boreal cool season is stratified into three stages, where the early and late (middle) stages approximately correspond to the seasonal maxima (minimum) in synoptic eddy activity that occurs over the North Pacific. Results provide new insight into the North Pacific midwinter suppression, that is during the midwinter suppression period, cyclonic perturbations entering the North Pacific storm track core are already deficient in magnitude compared to early and late winter stages. In both observations and model simulations, the North Pacific midwinter suppression feature is discovered to have a clear organized extension upstream into Siberia, while similar behavior is observed in association with the parallel midwinter suppression of the North Atlantic storm track that is (erroneously) simulated in the NSIPP model.

With new evidence of an upstream origin of the North Pacific midwinter suppression, the final portion of this thesis examines seasonally stratified variations in the behavior of upper tropospheric Rossby wave packets propagating across Asia prior to strong cyclogenesis in the North Pacific storm track. During the early and late stages of the boreal cool season, strong Pacific cyclogenesis is preceded by coherent synoptic scale wave packets that can be traced upstream the northern branch of the Asian waveguide a week in

advance. Results are quite different during midwinter. There is an increased sensitivity of synoptic-scale wave packets with a large-scale, upper-tropospheric flow pattern over Siberia. The consequence is a general dampening of synoptic eddy amplitudes along the northern branch of the Asian waveguide, which is proposed to be the contributing factor to the upstream weakening ultimately leading to a suppression in the North Pacific storm track during midwinter.

CHAPTER I

BACKGROUND

1.1 Introduction

Extratropical meteorology focuses on changes in sensible weather primarily due to the passage of surface fronts and inherent precipitation patterns associated with synoptic-scale transient eddies. Stemming from the early works of Charney (1947) and Eady (1949), baroclinic instability theory has enhanced the accuracy of numerical weather prediction, since several aspects of synoptic eddies are synonymous with baroclinic waveguides (Hartmann, 1974; Blackmon, 1976; Wallace *et al.*, 1988). These eddies play a significant role in the global distribution of heat and momentum (Chang *et al.*, 2002). Regions where synoptic eddy activity tends to be strongest are known as the *storm tracks*. In the Northern Hemisphere, two storm tracks are situated downstream and slightly poleward of the North Pacific and North Atlantic jet streams (Lau, 1988). Changes in the structure and magnitude of the storm tracks occur on intraseasonal to decadal time scales and substantially impact regional weather and climate in the midlatitudes (e.g., Chang & Fu, 2002; Kushnir *et al.*, 2002).

Baroclinic instability in the boreal storm track regions is largest during midwinter when the upper-tropospheric jets are strongest. Based upon linear theories, the annual cycle of storm track activity should directly correlate with the level of baroclinicity. Consistent with this expectation, synoptic eddies comprising the Atlantic storm track attain maximum amplitudes during midwinter. However, the magnitude of the Pacific storm track is largest during late fall and early spring while *decreasing* during midwinter despite enhanced levels of baroclinicity. Originally reported by Nakamura (1992), this intraseasonal phenomenon is known as the North Pacific midwinter suppression. Although the midwinter suppression has been reproduced in Atmospheric General Circulation Models (e.g., Christoph *et al.*, 1997; Zhang & Held, 1999), the exact mechanistic origin underlying this phenomenon

remains unresolved.

Forecasting the development and tracking pattern of synoptic eddies is limited to about 10 days due to intraseasonal low-frequency variability in the atmosphere (LFV). Key regions marking relative maxima in LFV include the North Pacific and the North Atlantic Oceans as well as over northwestern Russia (Dole, 1986). Much of the LFV in these regions can be attributed to recurrent large-scale weather regimes (Black, 1990). These primary weather regimes, the most familiar of which is blocking (Rex, 1950), typically occur in the exit regions of the climatological jet streams (Black & Evans, 1998) and are dynamically linked to variations in the midlatitude storm tracks (Dole, 1986; Lau, 1988). Advancements in medium-range weather forecasting and region climate prediction are thus greatly dependent upon improved simulations of large-scale weather regimes.

Atmospheric General Circulation Models (GCMs) provide a pragmatic framework towards advancements in medium-range weather forecasting and region climate prediction. The initial portion of this thesis uses extended integrations of NASA Goddard Space Flight Center (GSFC) GCMs to characterize the geographical distribution and dynamical mechanisms underlying large-scale weather regimes and climatological storm tracks. The goal is to highlight the extent of which the GCMs replicate the observed characteristics of intraseasonal variability, and in cases where shortcomings are identified, deduce the underlying physical reasons for systematic errors.

An ancillary goal of this thesis involves ascertaining a mechanistic origin of the North Pacific midwinter suppression. Our approach includes partitioning the cool season into three distinct stages: late fall/early winter, midwinter, and late winter/early spring. The results for the early and late stages are then contrasted with the midwinter results. Specifically, we want to elucidate any causes for unique subseasonal variations in the development of synoptic eddies in the Pacific storm track. Insight into the North Pacific midwinter suppression may enhance the understanding of dynamic interactions not only for intraseasonal temporal scales but also from interannual to decadal time scales (e.g., Clark & Serreze, 2000; Chang, 2001; Nakamura *et al.*, 2002; Orlanski, 2005).

1.2 Midlatitude subseasonal variability

Storm tracks and large-scale weather regimes are intrinsically linked to aspects of the time mean flow. The climatological flow of the atmosphere is marked by zonally asymmetric waves, also referred to as stationary or planetary waves. Large-scale topography and time-mean temperature gradients over the continent-ocean boundaries are the primary sources underlying the formation of stationary waves. In the boreal midlatitudes, westerly winds converge and strengthen in the stationary troughs over the western basin of the Pacific and Atlantic Oceans forming two climatological jet streams. The jet streams zonally extend across the oceans and diminish upstream the stationary ridges over the west coasts of North America and Europe. The jet streams are largest in magnitude in the upper troposphere and during winter, respectively where and when the thermal equilibrium temperature gradients are largest.

1.2.1 Synoptic eddies, storm tracks, and baroclinic development

Derived from synoptic observations and computer simulations, the primary factors affecting baroclinic development are summarized thusly (Carlson, 1998): (i) The surface pressure tendency associated with baroclinic growth increases linearly with increasing meridional temperature gradient and the ensuing vertical wind shear. However, there is a minimum threshold associated with this relationship. (ii) The surface pressure tendency increases with increasing latitude. (iii) Increasing static stability, primarily in the lower atmosphere, dampens the feedbacks (vertical mixing) between upper and lower-level perturbations. (iv) Diabatic heating enhances the available potential energy, (v) There is a minimum (maximum) wavelength threshold for baroclinic growth around 2000 (8000–10000) *km* that is optimized at 3000–4500 *km* (wavenumber 7 or 8 in the midlatitudes) for atmospheric conditions corresponding to that of the time-averaged state. The wavelength for optimized baroclinic growth increases (decreases) with increasing (decreasing) static stability.

Given these requisites, baroclinic zones in the zonally asymmetric circulation of the atmosphere are identified as the regions with the largest potential for baroclinic development. In the Northern Hemisphere, two baroclinic zones are located in proximity to the

stationary troughs and associated jet streams over the western basin of the Pacific and Atlantic Ocean. These regions mark the entrance region of the climatological storm tracks.

Development in the baroclinic zones is typically initiated by an upper-level wave packet emanating from the continent. With the upper-level disturbance over the ocean, the reduction of low-level static stability results in intensified vertical mixing, and the wave packet develops baroclinically. Conversely, baroclinic development may be stoked by strong near-surface perturbations that baroclinically modify the upper-level wave features. For example, anomalous heat and moisture fluxes emanating from the Kuroshio currents enhances surface baroclinicity in the entrance region of the Pacific storm track (Chang, 2005). Furthermore, a dissipated upper-level disturbance may leave behind regions of strong surface baroclinicity resulting in "secondary" development of a separate upper-level features (Carlson, 1998).

Observational studies of baroclinic wave packets indicate that the energy within a wave packet has an eastward velocity slightly larger than the time-mean flow, which is transferred between consecutive disturbances in the form of an eastward ageostrophic geopotential flux (Orlanski & Katzfey, 1991). This process is referred to as downstream development. Over the storm track regions, Orlanski & Katzfey (1991) found that an embedded disturbance loses energy to downstream disturbances at approximately the same rate it gains from upstream neighbors. Downstream development is responsible for the coherence of baroclinic wave packets and their propagation downstream from the regional baroclinic zones. In some cases, baroclinic wave packets persist long enough to circumnavigate the globe (Chang, 1993).

Several studies discuss the role barotropic energy conversions have on the life-cycles of synoptic-eddies in the storm track regions (e.g., Mak & Cai, 1989; Whitaker & Dole, 1995; Black & Dole, 2000). Stemming from the methodology of Hoskins *et al.* (1983), barotropic conversions can be assessed from the horizontal major axis orientation of the synoptic eddy with respect to the time-mean flow. The relative role barotropic interactions have during baroclinic growth is difficult to assess (Chang *et al.*, 2002). However in the exit regions of the climatological storm tracks, barotropic deformation is a primary sink of eddy activity.

Synoptic-eddy kinetic energy in these regions is imparted to the background flow and is considered to be an important source for planetary-scale anomalies observed in the exit regions of the storm tracks (e.g., Orlanski, 1998; Martin *et al.*, 2001).

1.2.2 Midwinter suppression

Observational analyses indicate that the seasonal variation in the magnitude of the climatological storm track does not always correlate with the level of baroclinicity. More specifically, Nakamura (1992) illustrated that the mean baroclinic wave activity over the North Pacific positively correlates with upper-tropospheric jet speeds up to $45 \text{ m} \cdot \text{sec}^{-1}$. During the midwinter, however, the correlation reverses as the average jet speed exceeds this threshold. No such phenomenon is observed over the North Atlantic as the climatological jet in this region does not reach such a threshold windspeed. The midwinter suppression of the North Pacific climatological storm track is counterintuitive, because the time-averaged state of the atmosphere is deemed to be more unstable during this time.

Comparison studies examining the midwinter suppression have led to further insights on storm track variability. For example, using reanalyses data and the Hamburg version of the European Centre model (ECHAM3), Christoph *et al.* (1997) identified that the midwinter suppression is neither due to a simple shift in the frequency distribution of eddies, nor to an increased number of blocking regimes. Zhang & Held (1999) successfully reproduced the Pacific midwinter suppression using a dry version of the Goddard Fluid Dynamics Laboratory (GFDL) GCM and suggested that the midwinter phenomenon is attributed to intraseasonal variations in the background flow field and not changes in diabatic heating.

Low-level northerlies of the East Asian monsoon result in a deepening of the planetary-wave trough coupled with a strengthening, narrowing, and southward shift in the observed East Asian jet. At this stage of the cool season, the polar-front jet in the Pacific tends to merge itself with the intensified subtropical jet (Lee & Kim, 2003). Nakamura *et al.* (2002) correlated interannual variations in the extent of the midwinter suppression with the strength of the East Asian winter monsoon (Siberian High), such that strong (weak) midwinter

Suppressions were associated with strengthened (weakened) East Asian monsoons and anomalously strong (weak) Pacific jet cores. In a comparison study using a GFDL GCM and reanalyses datasets, Chang (2001) found that these interannual variations in the Pacific storm track intensity stemmed from changes in the structure and residence time of the synoptic eddies. Nakamura & Sampe (2002) explored subseasonal variations in the midwinter suppression by noting anomalously strong Pacific jet cores in midwinter modify the eddy structure by spatially trapping synoptic eddies. During midwinter, a "subtropical" Pacific jet core is located further south and thus positioned approximately 3 km higher than the jet during early and late winter. Consequently, the midwinter Pacific jet core literally lifts synoptic eddies and weakens its interaction with the surface baroclinic zone.

Previous studies of the midwinter suppression have mainly focused on baroclinic development within or downstream of the Pacific baroclinic zone. In closing remarks of Nakamura (1992), it was suggested that one factor that may contribute to the North Pacific midwinter suppression is a midwinter weakening in the upstream source of tropospheric short waves (the "seeds" for downstream baroclinic development). Midwinter changes in the structure and dynamical interaction between synoptic eddies and the background flow *in* the Pacific storm track may ultimately be rooted in variations of upstream seeding. The upstream seeding may result from subseasonal variations in upstream flow field, as suggested by Zhang & Held (1999).

In a model setting, Orlanski (2005) has shown that variations in upstream seeding result in changes to the structure of the Pacific storm track as well as the planetary-flow field. The upper-level synoptic waves that seed the Pacific storm track emanate from two Asian waveguides: a northern branch over Siberia and a southern branch over Southeast Asia (Chang & Yu, 1999). The northern branch is considered the key source of upper-tropospheric short level waves for the Pacific storm track (Hakim, 2003). However, Chang (2005) has demonstrated that waves from the southern branch can influence Pacific cyclogenesis by advecting warm, moist air from the subtropics into the low-level baroclinic zone.

1.2.3 Large-scale weather regimes

Large-scale weather regimes (LWR) are characterized by quasi-stationary anomaly patterns persisting beyond the range of synoptic-scale variability (Dole & Black, 1990). The time-averaged structure of large-scale weather regimes has been documented in several independent studies using a variety of techniques: (i) case study of persistent flow anomalies (Dole & Gordon, 1983; Dole, 1986), (ii) teleconnectivity maps (Wallace & Gutzler, 1981), (iii) regional empirical orthogonal function (EOF) analyses (Lau, 1988), and (iv) clustering methods (Cheng & Wallace, 1993). In other words, LWR are robust and project strongly upon the dominant teleconnection patterns and leading EOFs of the boreal LFW.

Typically occurring in the jet exit regions over the eastern basins of the North Pacific and North Atlantic Oceans, the vertical structure of these regimes is equivalently barotropic, or the geopotential height anomalies show little or no westward tilt with height. The horizontal major axis for LWR is zonally oriented, while the largest geopotential height anomalies are found in the upper troposphere. In the key regions of LWR, there is a similar frequency of positive (anticyclonic) and negative (cyclonic) cases, and the probability of persistence lasting one more day is independent of the duration (Dole & Gordon, 1983).

A discussion of the potential factors affecting the life-cycles of LWR can be found in Black (1990) and Evans (2000). In this thesis, we focus on the primary mechanistic factors that act to *maintain* the principal low-frequency anomaly. Previous studies indicate that there are two primary factors in the maintenance of LWR: (i) linear interactions with zonal asymmetries in the time-mean flow and (ii) the ensemble feedback from synoptic eddies (e.g., Hoskins *et al.*, 1983; Dole & Black, 1990; Branstator, 1992; Nakamura & Wallace, 1993; Higgins & Schubert, 1994). Following the methods of (Dole & Black, 1990), barotropic and baroclinic diagnostics can be used to assess the relative impact these primary dynamical mechanisms have on LWR.

1.3 Subseasonal variability and GCMs

Atmospheric General Circulation Models (GCMs) simulate large-scale motions in the Earth's atmosphere and facilitate the assessment of past and future global climate scenarios. GCMs are also used to assimilate observational datasets, especially for data-poor regions pre-dating satellite measurements. Therefore, a fundamental expectation of GCMs employed in such studies is that they realistically represent various aspects of the current climate. Important components of regional climate variability include second order atmospheric circulation characteristics such as the midlatitude storm tracks and anomalous weather regimes.

Regional discrepancies in the statistics and dynamics of intraseasonal variability have been linked to errors in the simulated zonally asymmetric circulation. For example, Black & Evans (1998) observed anomalously weak barotropic energy conversions during the maintenance phase of large-scale weather regimes in the second National Center for Atmospheric Research (NCAR) Community Climate Model (CCM2). This model deficiency was attributed to relatively weak diffluence in the jet exit region of the Pacific. In a separate comparison study contrasting different versions of the CCM and the Goddard Earth Observing System (GEOS) GCMs, Black & Dole (2000) discovered that midlatitude storm tracks extended too far downstream into regions of anomalously weak barotropic deformation.

Recent studies indicate that fundamental aspects of weather regimes remain misrepresented in climate models (Kaurola, 1997; Black & Evans, 1998; Evans, 2000). GCMs have had historical difficulties representing intraseasonal low-frequency variability. In past studies, low frequency variability was often observed to be relatively weak (Lau and Nath, 1987; Ferranti et al. 1994, Chen and van den Dool, 1995). In this thesis, some main points in the model validation that need to be covered include: (i) How well are regional levels of intraseasonal low-frequency variability simulated? (ii) Do any notable deficiencies exist in the simulated structure of LWR? (iii) What are the impacts of such differences on the dynamics of LWR? (iv) Are there any dynamical shortcomings attributable to the

background flow representation? (v) What are the implications of the results for potential model improvement?

Likewise, one would expect basic features of synoptic eddies to be well represented by GCMs. Storm track characteristics, including the Pacific midwinter suppression, provide important benchmark tests in validating the climate of GCMs. Thus, the model validation will address the following points: (i) How well are the primary storm tracks represented in terms of magnitude and structure? (ii) Are there any notable deficiencies in the simulated structure of synoptic eddies? (iii) How accurate are the large-scale patterns of baroclinicity and barotropic deformation? (iv) Are there any significant shortcomings in the simulated storm track dynamics? (v) Is the North Pacific midwinter suppression captured by the model simulations? (vi) What are the implications of the results for potential model improvement?

1.4 Summary

The following chapter (Ch. 2) introduces the simulated and observational datasets used in this study followed by a discussion of the general methodology. The presentation of the results is broken up into three chapters (Ch. 3–5) followed by a summary and conclusion (Ch. 6).

Chapter 3: A parallel analysis of the climatological characteristics of the general circulation is provided. This includes an examination of the three-dimensional structure and climatological mean flow interaction of storm tracks and large-scale weather regimes in recent NASA GSFC GCM simulations, focusing on the Northern Hemisphere wintertime when such variability is most prominent. Within this section, a composite analysis of large-scale weather regimes over the North Atlantic and North Pacific Oceans is conducted. The goal is to provide insight into potential reasons for discrepancies observed in the simulation of large-scale weather regimes. Additionally, it is of interest to test the extent to which the NASA GSFC GCMs capture the North Pacific midwinter suppression phenomenon.

Chapter 4: The second portion is dedicated to investigating the *development* of synoptic eddies in an effort to understand the physical reasons behind the model shortcomings

of the climatological storm tracks identified in Chapter 3. Furthermore, we take a new approach to study intraseasonal variability by seasonally stratifying the data. Our hope is to isolate unique aspects of baroclinic development and provide insight into the North Pacific midwinter suppression.

Chapter 5: Building upon the results from Chapter 4, the final portion of this work determines an origin of the North Pacific midwinter suppression phenomenon by exploring intraseasonal changes in the upstream flow field prior to Pacific cyclogenesis. We seasonally stratify the data in order to isolate variations in upstream wave behavior associated with the different stages of the cool season. We conclude by proposing an upstream origin behind the systematic midwinter weakening of baroclinic disturbances over the North Pacific by ascertaining the dynamical behavior leading to the midwinter weakness in the upper tropospheric seeding of Pacific cyclogenesis events.

CHAPTER II

DATASETS AND GENERAL METHODOLOGY

2.1 Observational datasets

The observational dataset used for the comparison study are the National Centers for Environmental Prediction (NCEP)-NCAR reanalyses (Kalnay & Coauthors, 1996) acquired from the National Oceanic and Atmospheric Administration (NOAA)-Cooperative Institute for Research in Environmental Sciences (CIRES) Climate Diagnostic Center in Boulder, Colorado (from their Website at <http://www.cdc.noaa.gov/>). The reanalysis dataset is daily-averaged data archived on a 2.5° latitude by 2.5° longitude grid over 17 pressure levels. To facilitate direct cross comparisons, the climatological and dynamical analyses presented in this study focus on the same time period as the GCMs, specifically the 17 years from 1979 to 1995.

For the observational analysis examining the mechanistic origin of the North Pacific midwinter suppression (Chapter 5), we use the ERA40 reanalysis dataset provided by the European Centre for Medium-Range Weather Forecasts (ECMWF) and downloaded from the Data Support Section of the Scientific Computing Division at the NCAR (from their Website at <http://dss.ucar.edu/datasets/ds118.1/>). The ERA40 reanalysis dataset is archived on a 2.5° latitude by 2.5° longitude grid over 23 pressure levels. We use 45 years of daily-averaged data from September 1958 through August 2002.

2.2 Model datasets

The model datasets used in this study are Atmospheric Model Intercomparison Project (AMIP)-II type simulations of two general circulation models developed at The National Aeronautics and Space Administration (NASA) Goddard Space Flight Center (GSFC). The first is a subset of the env05 AMIP run of version 1 of the Aries model used in NASA's Seasonal-to-Interannual Prediction Project (NSIPP) model. The NSIPP simulation employs

a finite-differenced, primitive equations dynamical core that is run at a horizontal resolution of 2.0° latitude by 2.5° longitude with 34 vertical levels (Suarez & Takacs, 1995). The second model simulation is the AMIP fvccm3-1.2.0 run of the NASA-National Centers for Atmospheric Research (NCAR) model developed jointly between the Data Assimilation Office (DAO) of NASA GSFC and the NCAR Climate and Global Dynamics Division (referred to as the NASCAR) model. NASCAR is a next-generation GCM that employs a novel finite-volume approach to computational fluid dynamics [e.g., Lin & Rood (1997)]. The simulation considered here is a run at a horizontal resolution of 2.0° latitude by 2.5° longitude with 55 vertical levels. For both model simulations we sample daily averaged data interpolated to the 17 standard pressure levels used in the NCEP-NCAR reanalyses.

2.3 Characterizing subseasonal variability

Initial analysis involves separating the general circulation into climatological and perturbation components. The daily climatology is derived by smoothing a seasonal cycle derived from the calendar time-series of long-term daily averages with a 91-point Parzen window (Fuenzalida & Rosenblüth, 1990). Daily anomalies (indicated by primes) are then computed by subtracting the smoothed daily climatology from the raw data. The anomalies are then separated into high-pass and low-pass components using a 151-point Lanczos filter. The high-pass (HP) band filter retains anomalies having periods of 2.5–6 days, while low-pass (LP)-filtered anomalies are variations with periods greater than 10 days (low-frequency eddies). Fluctuations with periods from 7 to 10 days are essentially excluded, however separating the HP and LP bands this way ensures clear distinctions between high and low-frequency fluctuations (Blackmon, 1976).

From a fixed location, Blackmon *et al.* (1977) noted that wave trains of baroclinic waves have frequencies of about 4 days, which is in general agreement with baroclinic theory and synoptic evidence (e.g., Hartmann, 1974). The high-pass band filter of 2.5–6 days is designated to isolate variations associated with baroclinic waves. However, Trenberth (1991) mentioned a potential problem when filtering anomalies with such a narrow band. The filtering introduces unwanted frequencies into the time-series by effectively broadening

the Gaussian representing the life-cycle of a disturbance. As a result, misinterpretations of the results may arise due to the "ringing" effect (e.g., see Appendix in Chang, 1993). To avoid this problem, studies such as Trenberth (1991) expand the band filter and include variations from 2–8 days. Other studies use the unfiltered meridional wind variance as a measure of baroclinicity (e.g., Chang, 2001). However, we approach the issue by including 151 points in the filter. Although this increases computation time, decomposing the time-series using a large number of coefficients minimizes the impacts of "ringing" outside the respective frequency bands and more effectively isolates variations associated with baroclinic waves.

Storm tracks mark the preferred propagation regions of baroclinic waves. Therefore, winter-mean storm track patterns are characterized by the regional maxima in HP filtered geopotential height variance in the mid- to upper troposphere (Trenberth, 1991). The three-dimensional structure of the transient eddies within the storm tracks are derived using the linear regression method of Lim & Wallace (1991), as shown in Equation 1.

$$b(i) = \frac{1}{N} \sum_t y_t(i) \cdot x'_t \quad (1)$$

N is the number of observations in the time series, while $y_t(i)$ represents an unnormalized time series of a particular field variable. x'_t is a reference time series normalized by its standard deviation (zero mean with unit variance), so the regression coefficient, $b(i)$ carries the units of the regressed variable, $y_t(i)$. Plotting maps of regression coefficients for different levels and time lags respectively illustrate the structure and evolution of baroclinic waves.

To test the GCMs ability to reproduce the Pacific midwinter suppression, the envelope function of Nakamura & Wallace (1990) is used to portray the local seasonal cycle in the level of baroclinic wave activity (Equation 2).

$$f_{env} = 2 \cdot [(Z'_{HP} \cdot Z'_{HP})_{LP}] \cdot \frac{\sin^2(45^\circ)}{\sin^2(lat)} \quad (2)$$

The envelope function, proportional to the 6-day lowpass-filtered HP geopotential

height variance, is designed to fit the amplitude modulation of baroclinic waves. Furthermore, the square-root of the envelope function gives the lowpass-filtered amplitude of baroclinic waves at a given time (Nakamura & Wallace, 1990). Therefore, the envelope function is utilized to illustrate the seasonal evolution in the magnitude of the storm tracks.

Episodes of low-frequency variability are assessed in terms of weather regime frequency (Black & Evans, 1998). Occurrences of persistent wintertime flow anomalies (PFAs) are determined following the method of Dole & Gordon (1983). An anticyclonic (cyclonic) PFA case is selected when the lowpass-filtered geopotential height anomaly exceeds +100 (−100) m for at least 10 days. Key regions marking the local maximum number of PFAs are identified for both Atlantic and Pacific sectors. Composite averages of PFAs over these key regions are used to characterize the typical three-dimensional structure and assess the barotropic and baroclinic energy conversions associated with the maintenance of the cases.

2.4 Barotropic dynamical diagnostics

Barotropic diagnostics assess the conversion of kinetic energy between the mean-flow and transient weather disturbances. Barotropic modes in the atmosphere are independent of depth and stratification and derive energy from the zonal wind shear (I. Kuo, 1949). Therefore, barotropic conversions depend upon the deformation in the horizontal structure of transient weather disturbances (Farrell, 1989). As the horizontal shape of a transient disturbance changes, the correlation between the zonal and meridional velocity components associated with the disturbance becomes nonzero (Carlson, 1998).

The barotropic dynamical interaction between intraseasonal anomalies and the climatological mean flow is diagnosed following the methods of Black & Dole (2000). This involves analyzing the barotropic \mathbf{E} vectors due to intraseasonal eddies (Hoskins *et al.*, 1983) and studying their spatial relation to horizontal gradients in the climatological-mean zonal wind field (\bar{U} ; Simmons *et al.*, 1983). Here \mathbf{E} vectors are related to the structure of the horizontal anomaly field and denoted mathematically by $\mathbf{E} = \{\overline{v'v'} - \overline{u'u'}, -\overline{u'v'}\}$, where an overbar indicates a climatological average. Meridionally (zonally) elongated eddies are generally associated with eastward (westward) directed \mathbf{E} vectors (Black & Dole, 2000).

The y -component is related to the meridional phase tilt with southward directed \mathbf{E} vectors indicating a southwest to northeast eddy orientation. The local barotropic energy conversion is proportional to the dot product of the \mathbf{E} vector and the horizontal gradient of the climatological-mean zonal wind ($\mathbf{E} \cdot \nabla \bar{U}$; Simmons *et al.*, 1983)]. Thus, \mathbf{E} vectors that are directed up (down) the gradient of \bar{U} will be associated with positive (negative) barotropic energy conversions from the zonal-mean flow into the eddies.

2.5 *Baroclinic dynamical diagnostics*

Baroclinic disturbances lower the center of gravity of the atmosphere by ultimately converting the available potential energy of the zonal mean flow into eddy kinetic energy. The motion decreases the meridional temperature gradient via the lifting/poleward advection of warm, light air and sinking/equatorward advection of colder, denser air. Baroclinic disturbances grow resulting from mutual reinforcements between upper and lower-level waves resulting from feedbacks in the circulation pattern to restore thermal wind equilibrium (geostrophic and hydrostatic balance). This reinforcement relies on a horizontal relative phase shift between the geopotential height and temperature fields, or a vertical tilt of the wave axes in geopotential height (Wallace & Hobbs, 1977).

Baroclinic energy conversions can be inferred by examining interactions between the horizontal eddy heat flux vectors and background temperature field. Equation (10) of Dole & Black (1990) measures the conversion of available potential energy of the zonal mean flow into available potential energy for the synoptic eddy and is a representative measure of local baroclinic conversions. This term is proportional to the dot product of horizontal eddy heat flux vectors and the gradient of the climatological-mean temperature field ($-\overline{\mathbf{u}'T'} \cdot \nabla \bar{T}$). In this case, downgradient (upgradient) heat fluxes are associated with positive (negative) baroclinic energy conversions. Considered together the barotropic and baroclinic diagnostic tools provide dynamical insight into potential underlying physical reasons for any systematic errors observed in the models.

CHAPTER III

COMPARATIVE STUDY OF MIDLATITUDE SUBSEASONAL VARIABILITY: STATISTICS AND STRUCTURES

3.1 Winter Mean Circulation

Due to its linkage to storm tracks and anomalous weather regimes, the first part of the model assessment examines important aspects of the climatological-mean zonally asymmetric circulation. Figure 1 displays DJF average zonal wind (\bar{U} , shading) along with contours of the climatological stationary waves at 300 *hPa* for both models and observations. For the NSIPP model, the simulated stationary trough over the western Pacific is anomalously broad and the local height maximum is shifted 10° upstream. The downstream ridge in the NSIPP model is notably amplified and shifted westward relative to observations. The NASCAR model exhibits a stationary trough over the western Pacific, which corresponds very well with the location of the observed trough, yet is more zonally confined especially in terms of its eastward extent. The downstream ridge in the NASCAR model is broader and shifted northwestward relative to observations. Both of the above features contribute to a westward retraction in the East Asian jet. The stationary wave structures in the Atlantic region are very similar between the two models. The simulated stationary troughs over northeastern Canada are deeper and extend southward compared to observations. The Atlantic stationary ridge is well positioned in both GCMs but is a bit too strong (weak) in the NASCAR (NSIPP) model.

We note that the average zonal wind magnitude throughout the Northern Hemisphere is greater in the GCMs than in observations. This is particularly true in the NSIPP model, where the core regions of the climatological jets are typically $5\text{--}10 \text{ m} \cdot \text{sec}^{-1}$ greater than observations. For the NASCAR model, the jet cores are relatively similar in magnitude to the observed cores. Both models produce Pacific jet cores that terminate farther upstream

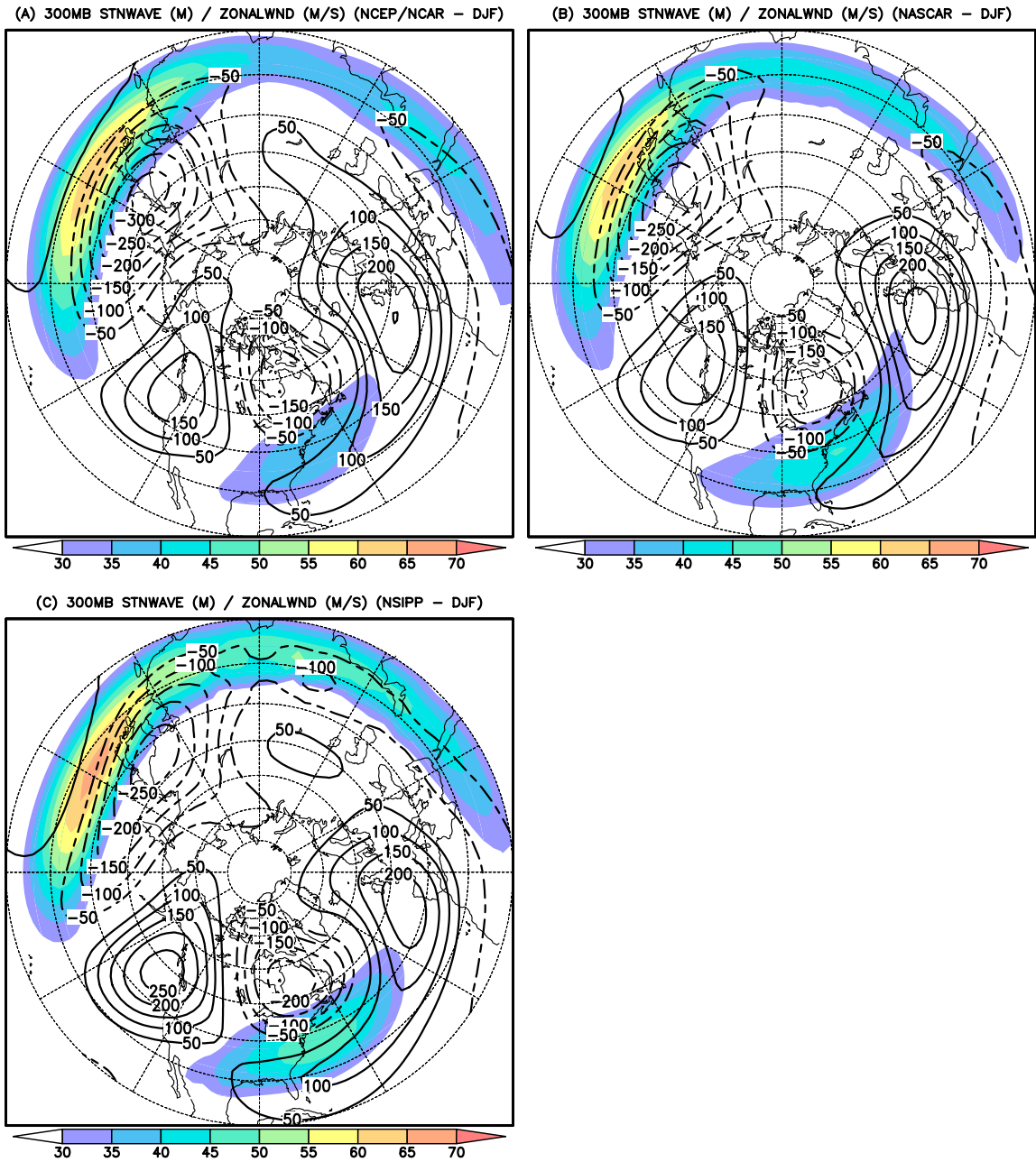


Figure 1: The climatological zonal wind (shading: $m \cdot sec^{-1}$) and stationary wave field (contour intervals: 50 m) at 300 hPa for (a) NCEP-NCAR reanalysis, and (b) NASCAR and (c) NSIPP models. The climatologies are derived from the AMIP-II time period for the 90-day winter (DJF).

compared to the observed jet structures. This leads to a stronger zonal wind gradient ($d\bar{U}/dx$) west of the date line over the North Pacific. Opposing characteristics are observed over the Atlantic region. Further discussion of the discrepancies in the magnitude and location of the climatological jet streams are provided in subsequent sections detailing the dynamical interaction between intraseasonal anomalies and the time-mean flow.

Prior to examining the regional intraseasonal eddy characteristics, we first illustrate the vertical structure of the horizontally averaged eddy variability in different frequency bands. Figure 2 displays vertical profiles of the areal-averaged (20°N–90°N) eddy kinetic energy ($EKE = \frac{1}{2} \cdot \overline{u'u' + v'v'}$) associated with unfiltered, high-pass, and low-pass anomalies. These plots illustrate that the winter-mean level of eddy activity in the GCMs is relatively weak through the mid- to upper troposphere. This discrepancy is greater in the HP band than in the LP band. In the upper troposphere, the NASCAR model performs better in both the HP and LP bands, while the NSIPP model is superior at midtropospheric levels. Thus the NSIPP model exhibits a weaker vertical variation in EKE. The models closely cluster around observed values in the lower troposphere.

3.2 Climatological Storm Tracks

3.2.1 Synoptic Eddy Diagnostics

Figure 3 depicts the climatological storm tracks by shaded regions of the rms Z'_{HP} overlaying contours of \bar{Z} (zonal mean not removed) at 300 hPa. Also plotted in Figure 3 are the horizontal E vectors associated with HP eddies (\mathbf{E}_{HP} ; Hoskins *et al.*, 1983). The general location and structure of the primary storm tracks are well reproduced in the GCMs. In the Pacific region, the simulated storm tracks are weaker in magnitude than in observations, with the NSIPP Pacific storm track having the lowest relative magnitude. These model characteristics are consistent with the previously noted levels of HP EKE analyzed for the mid- to upper troposphere (Figure 2). Downstream of the simulated storm track cores over the North Pacific, we note an eastward *decrease* of rms Z'_{HP} south of the Aleutian Islands and an eastward *increase* of rms Z'_{HP} farther downstream over the coastal region of northwest North America (just east of the climatological ridge axis). In the reanalysis data there is a

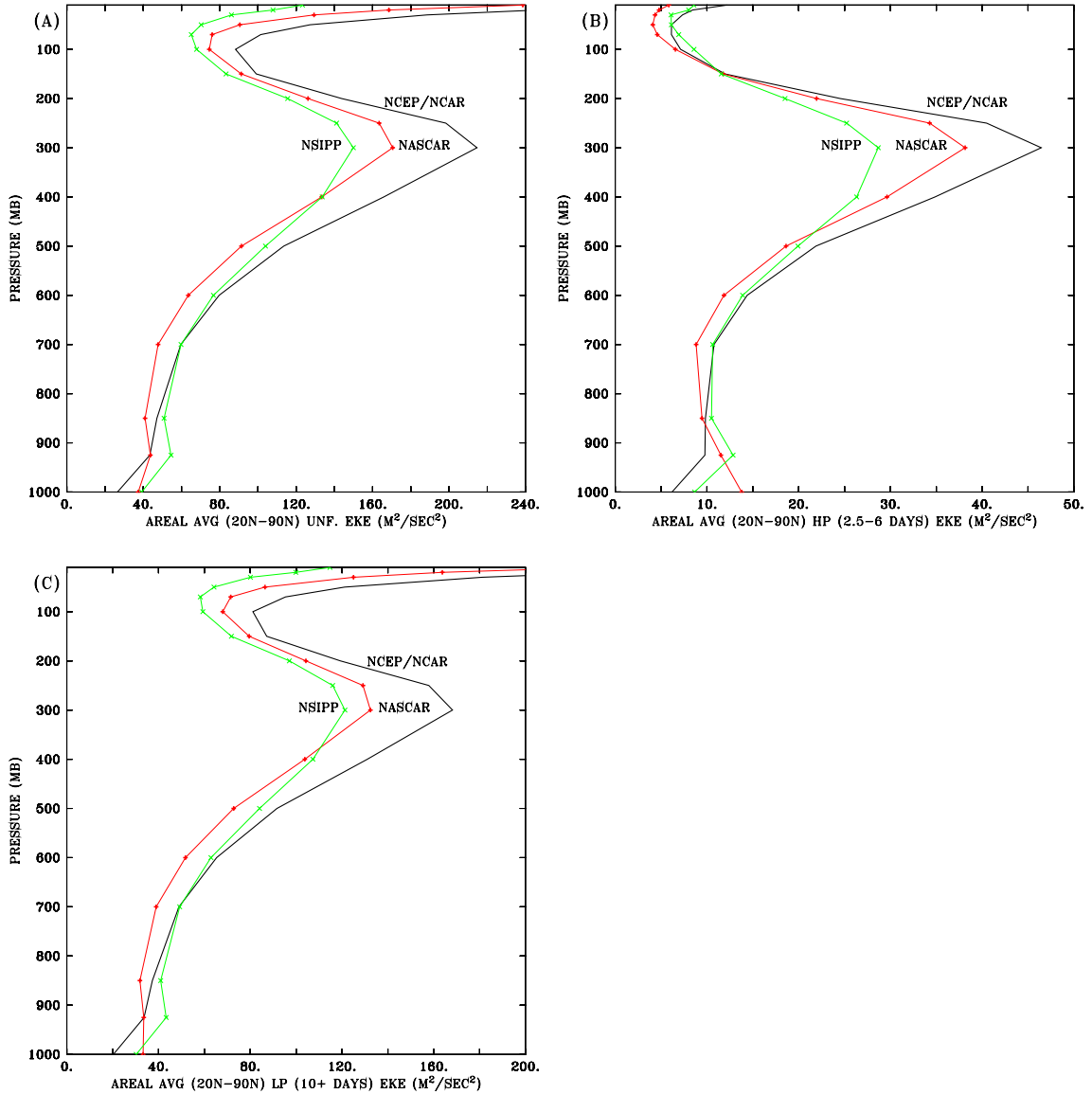


Figure 2: Vertical profiles of the areal-averaged eddy kinetic energy for each dataset derived from (a) unfiltered, (b) high-pass filtered, and (c) low-pass filtered anomalies. The averaging region includes all grid points north of 20°N.

more continual and gradual decrease in rms Z'_{HP} extending downstream from the core of the storm track region into North America.

In the Atlantic region, the properties of the simulated storm tracks correspond somewhat more closely in structure and magnitude to observations. The Atlantic storm track in the NSIPP model is deficient in magnitude, whereas the core magnitude of the NASCAR Atlantic storm track is closer to that of observations. The local maxima in the Atlantic storm tracks for all three datasets are approximately located near and to the east of the Canadian Maritimes. The NSIPP model exhibits an anomalously weak poleward deflection of the storm track activity over western Europe compared to observations. This feature is consistent with the anomalously weak stationary ridge observed in this region (Figure 1).

In the exit regions of the climatological storm tracks, the \mathbf{E}_{HP} vectors point eastward toward lower values of the winter-averaged zonal wind, indicating that the synoptic eddies lose energy to the mean flow via barotropic conversions (Black & Dole, 2000). Since earlier noted model biases in $d\bar{U}/dx$ (located west of the date line) coincide with the core of the Pacific storm track (cf. Figures 1 and 3), we expect stronger barotropic damping of synoptic eddy activity to occur in the Pacific storm tracks of the model simulations. For the NCEP reanalyses, \mathbf{E}_{HP} vector patterns found downstream of the climatological storm tracks exhibit a more prominent latitudinal fanning compared to the GCMs, which tend to exhibit southeastward directed \mathbf{E}_{HP} vectors in these regions. This observations is consistent with an enhanced southward (northward) eddy flux of wave activity (zonal momentum) in the model simulations.

We next evaluate the typical three-dimensional structure of HP transient eddies within the storm tracks. From the methods of Lim & Wallace (1991), the typical three-dimensional structure of transient eddies are determined by regressing the height anomaly field (Z') onto a normalized time series measuring the local amplitude of synoptic waves in the Pacific storm track region. For this analysis, the time series used is the value of the 500 hPa HP-filtered meridional wind anomaly (v'_{HP}) at (42°N , 170°W), which is a midtropospheric grid point located within the core of the Pacific storm track for all three datasets. The

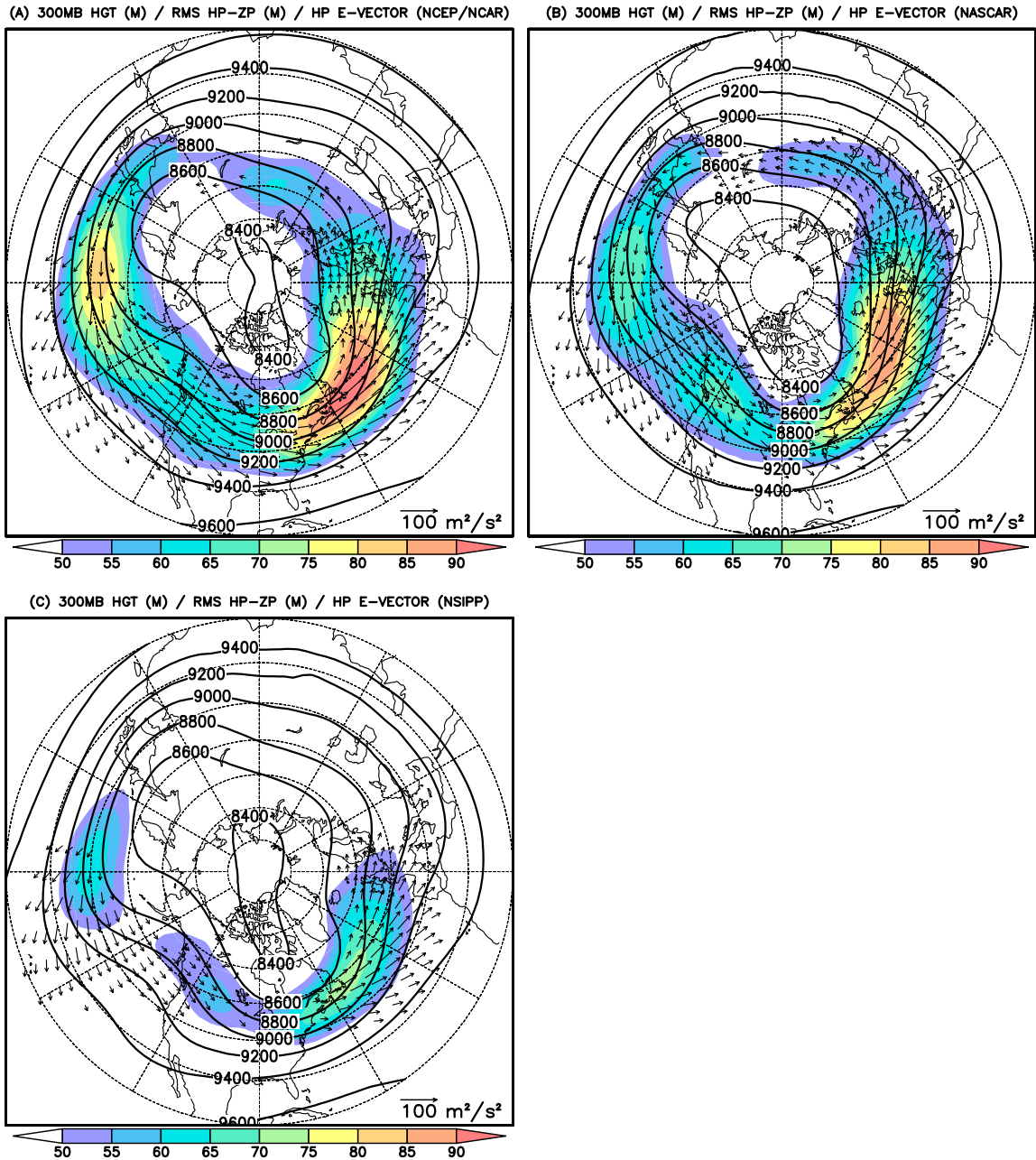


Figure 3: The rms high-pass filtered geopotential height anomalies (shaded regions: units m) superposed on the climatological height field (contour intervals: $200 m$) at $300 hPa$ for (a) NCEP-NCAR reanalyses and (b) NASCAR and (c) NSIPP GCMs. The E vectors associated with the $300 hPa$ HP eddies are plotted for each dataset with a scale vector provided. The threshold vector length is $15 m^2 \cdot sec^{-2}$.

regression results, shown in Figure 4, verify that the GCMs produce synoptic transient eddies with horizontal and vertical anomaly structures that are generally similar to observed events. Primary differences in the model anomaly structures include (i) anomalously low perturbation magnitudes (especially in the lower troposphere) and (ii) more pronounced southwest to northeast tilts. The latter feature is consistent with the earlier noted model biases in meridional wave propagation (Figure 3) and could be linked to the meridional shear associated with the anomalously strong jets.

Regression of v'_{HP} in the core region of the Atlantic storm tracks (Figure 5) produced similar results among the three datasets. However, the magnitudes of the geopotential anomalies in the GCMs are closer to observations over the Atlantic than the Pacific (as might be anticipated from Figure 3). Overall, the regression analysis results suggest only modest misrepresentations in the structure of the synoptic eddies by the models.

The next part of our assessment examines the climatological patterns of eddy heat and zonal momentum fluxes associated with HP eddies. Figure 6 displays the winter-averaged horizontal heat flux vectors associated with HP eddies overlaying the climatological temperature field (\bar{T} , contours) at 700 hPa. The gray regions in Figure 6 highlight areas where the winter-averaged baroclinic energy conversions exceed a common threshold value. First, it is important to note that the polar temperatures in the GCMs are anomalously cold, more so in the NASCAR model. This observation is hydrostatically consistent with the anomalously low heights observed in the upper troposphere over the Arctic regions in the models (see Figure 3). Consistent with the structural analyses presented in Figures 4 and 5, the synoptic eddy heat flux *patterns* closely resemble that of the reanalyses data. However, in the NSIPP model the associated baroclinic energy conversions are typically 20% – 30% weaker throughout the Pacific and Atlantic storm tracks. This deficiency is consistent with the difference in HP EKE presented in Figure 2. Although the baroclinic energy conversions in the NASCAR model are anomalously weak in the Pacific storm track core, they are anomalously high farther downstream near the west coast of North America (not shown). Over the Atlantic region, baroclinic energy conversions associated with the

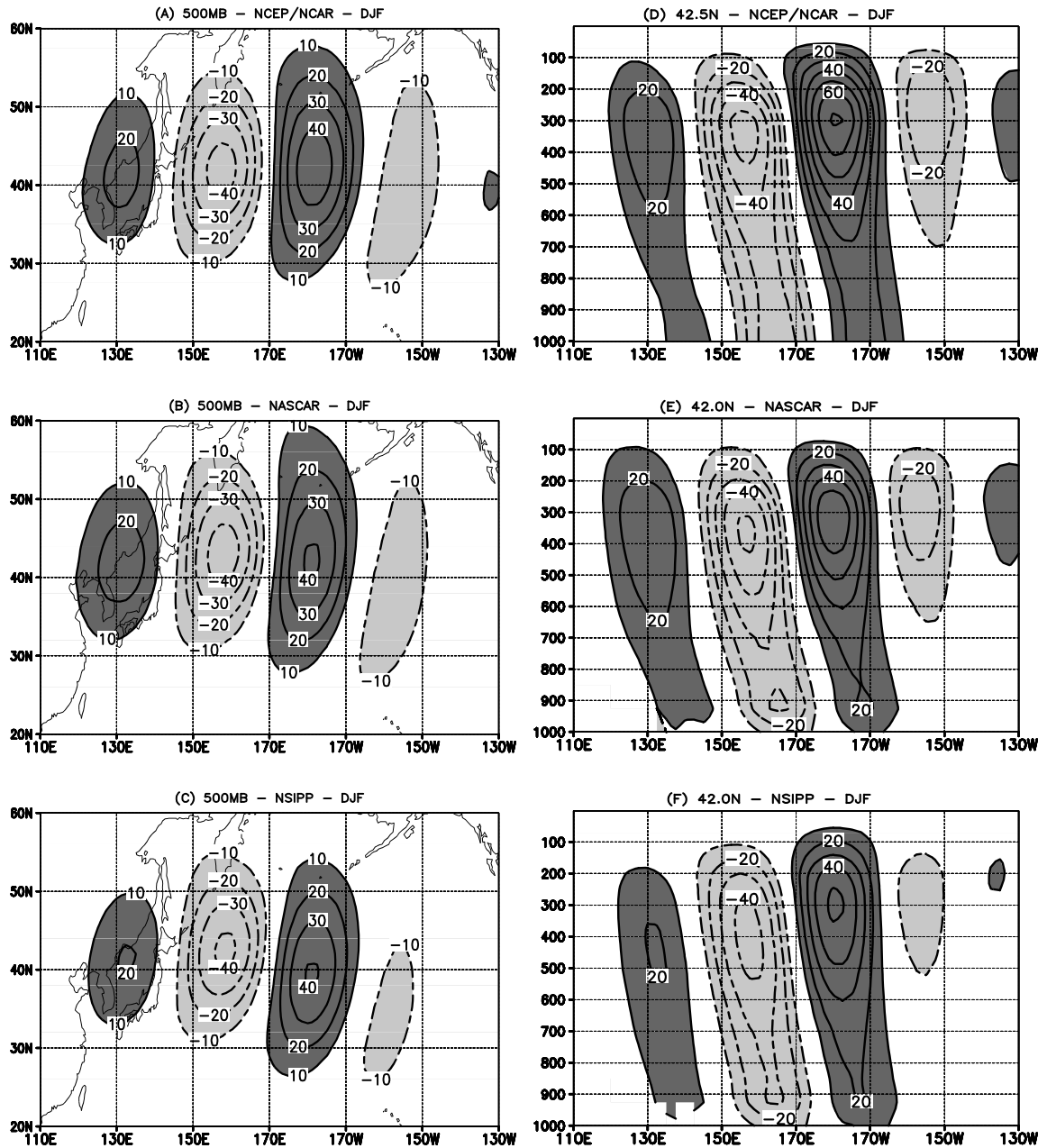


Figure 4: The height anomaly field regressed onto the time series of the 500 hPa HP-filtered meridional wind anomaly at 42°N, 170°W. The regressed height field (contour intervals: 10 m) at 500 hPa is displayed for the (a) NCEP-NCAR reanalyses and (b) NASCAR and (c) NSIPP models. (d)-(f) The vertical cross sections of the regressed height field at 42°N for each respective dataset. Positive values are darkly shaded, and negative values are lightly shaded.

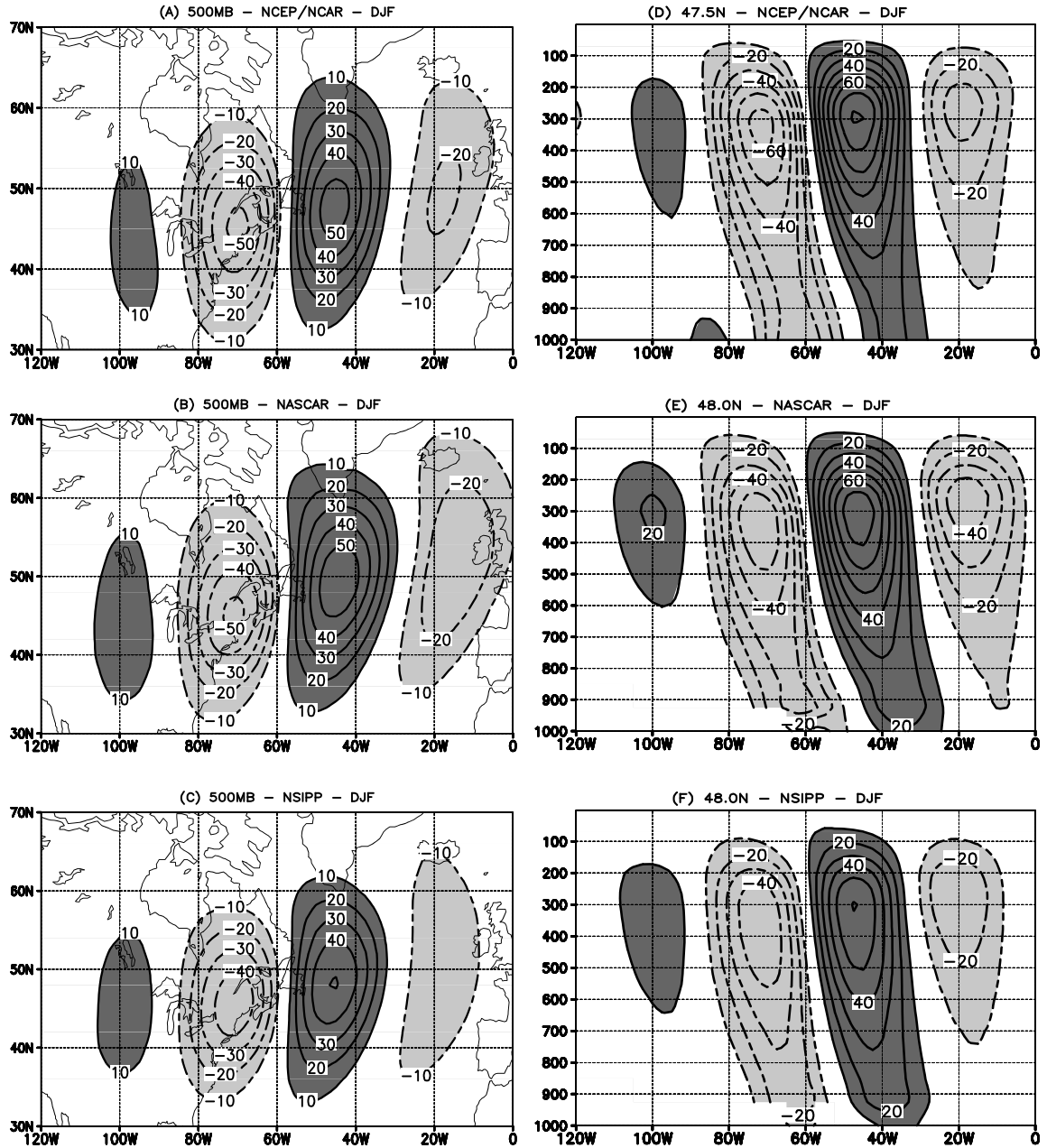


Figure 5: The height anomaly field regressed onto the time series of the 500 hPa HP-filtered meridional wind anomaly at 48°N, 305°W. The regressed height field (contour intervals: 10 m) at 500 hPa is displayed for the (a) NCEP-NCAR reanalyses and (b) NASCAR and (c) NSIPP models. (d)-(f) The vertical cross sections of the regressed height field at 48°N for each respective dataset. Positive values are darkly shaded, and negative values are lightly shaded.

NASCAR HP eddies actually exceed observations. This appears related to the climatological structure of the temperature field, specifically the larger horizontal gradients observed over the northern Atlantic region in association with anomalously cold temperatures found over northeastern Canada.

The results of Black & Dole (2000) indicate the importance of the barotropic deformation field in determining the structure of the climatological storm tracks. Analyses of regional barotropic deformation magnitudes (not shown) indicate that the regions of maximum barotropic deformation in both GCMs are more localized and shifted westward relative to the observations over the North Pacific (consistent with Figure 1). The biases in the regional patterns of barotropic deformation are consistent with the differences in the horizontal storm track structures noted in Figure 3. For example, the local maxima of rms Z'_{HP} observed in the models over northwest North America are likely linked to a relative lack of diffluence over this region (which is in turn associated with the previously noted westward shifts in the simulated climatological ridge feature over this region). Also, as discussed earlier the relative weakness of the simulated Pacific storm tracks may be due to local enhancements in $d\bar{U}/dx$ (see discussion of Figure 3). In a latter section of this work, we will illustrate how the midwinter suppression in synoptic eddy activity over the North Pacific storm track is associated with a relative midwinter weakness in the *magnitude* of the growing synoptic eddies. Sources underlying the upstream weakening may also be responsible for the winter-mean weakness in the simulated storm tracks. Furthermore, another study has shown that increasing the resolution in the GCMs results in a net increase in the magnitude of the storm tracks.

3.2.2 Midwinter Suppression

A common method for assessing the seasonal variation of the storm tracks includes a test for the reproduction of the midwinter suppression. Here we use the envelope function of Nakamura & Wallace (1990) to measure low-frequency variations in the amplitude of baroclinic wave activity. Figure 7 displays the daily climatological trend of the envelope function longitudinally averaged across the zonal extension of the Pacific and Atlantic

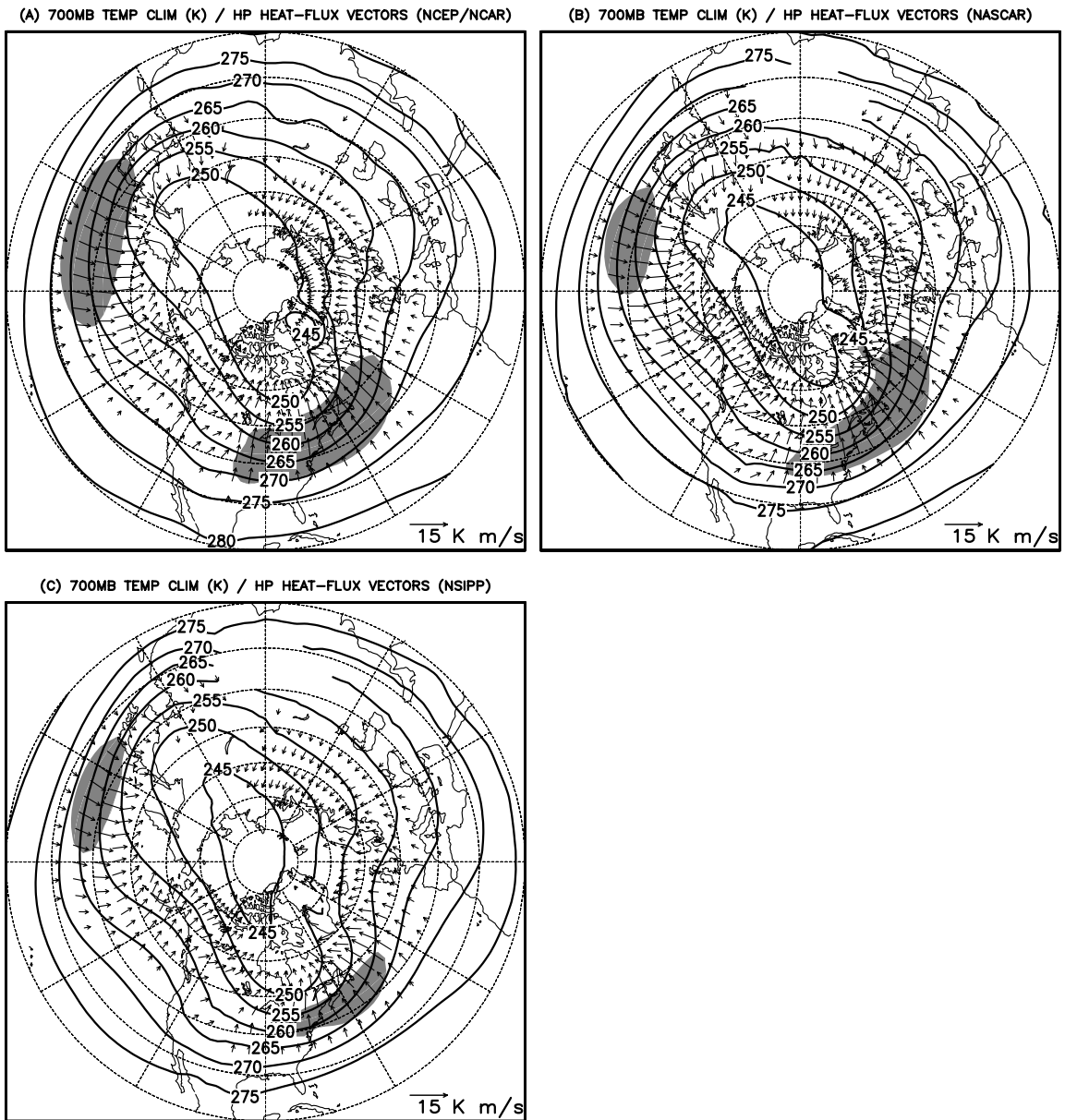


Figure 6: Synoptic eddy heat flux vectors (units: $K \cdot m \cdot sec^{-1}$) superposed on the climatological temperature field (contour intervals: 5 K) at 700 hPa for (a) NCEP-NCAR reanalyses and (b) NASCAR and (c) NSIPP models. A scale vector is provided for the eddy heat flux. Gray shaded regions mark the winter-averaged baroclinic energy conversions greater than $5 \times 10^{-5} K^2 \cdot sec^{-1}$.

storm tracks at 300 *hPa*. It is evident that each GCM faithfully reproduces a midwinter suppression over the North Pacific, with a relative maxima occurring in the late autumn and early spring. Conversely, the observed level of baroclinic wave activity over the North Atlantic attains a maximum during the midwinter, and this result is reproduced by the NASCAR model. Interestingly, however, the NSIPP model actually produces a midwinter suppression over the North Atlantic, mimicking the observed behavior of the North Pacific midwinter suppression. Nakamura (1992) found that baroclinic wave activity directly correlates to the strength of the upper tropospheric jet for wind speeds up to approximately $45 \text{ m} \cdot \text{sec}^{-1}$. As previously noted, the NSIPP's climatological zonal wind is typically 5–10 $\text{m} \cdot \text{sec}^{-1}$ greater in magnitude compared to observations. Consequently, during midwinter, the magnitudes of the Atlantic jet core in the NSIPP model (not shown) actually exceed the "threshold" values reported by Nakamura. Thus, we are led to the interesting result that errors in the strength of the North Atlantic jet stream can lead to unanticipated higher-order errors in the representation of regional climate variability.

3.3 *Large-scale weather regimes*

We next study the model representation of large-scale weather regimes. Episodes of persistent flow anomalies (PFAs) are used as a means to determine how well the GCMs simulate the regional levels of intraseasonal low-frequency variability. Figure 8 displays regional frequency distributions of PFA events for the three datasets, noting that the areas having the highest number of PFAs are generally found near the exit regions of the climatological jet streams. The key points used to composite cases of PFAs are marked with an "X" in Figure 8. Following Black & Evans (1998), we perform pointwise significance tests of the difference between simulated and observed PFA frequencies (Figure 9) to guide the discussion below.

We first observe that the *magnitudes* of the simulated regional frequency patterns compare quite well with observations, noting that GCMs have had historical difficulty in simulating the appropriate level of low-frequency variability (Black & Evans, 1998). On

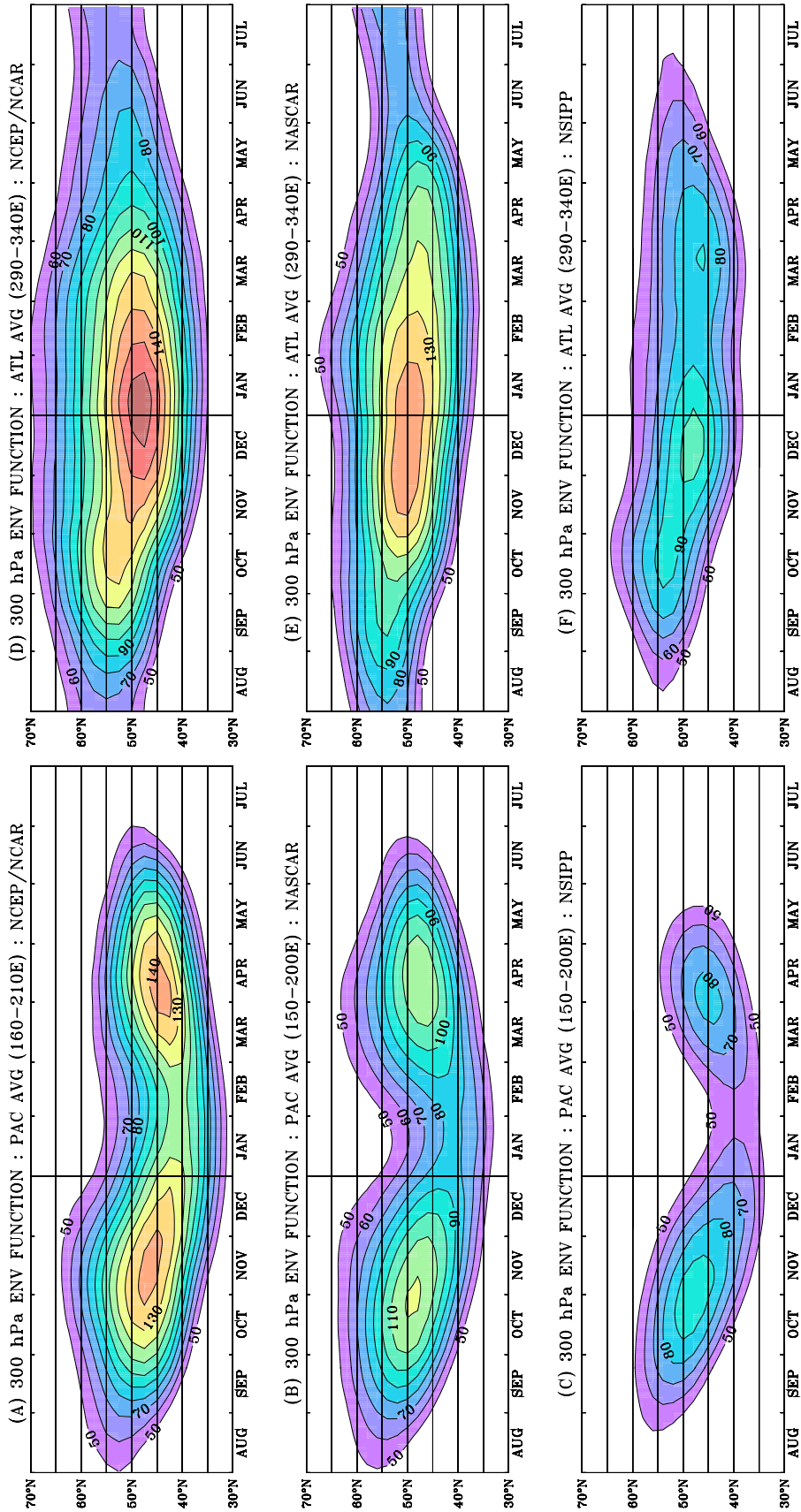


Figure 7: The annual cycle of the climatological average 300 hPa rms of the envelope function (shaded contour intervals: 15 m) longitudinally averaged across the core region of the (a)-(c) Pacific storm tracks and (d)-(f) Atlantic storm tracks for the NCEP-NCAR reanalyses and NASCAR and NSIPP models, respectively. A vertical axis marking 1-Jan is plotted.

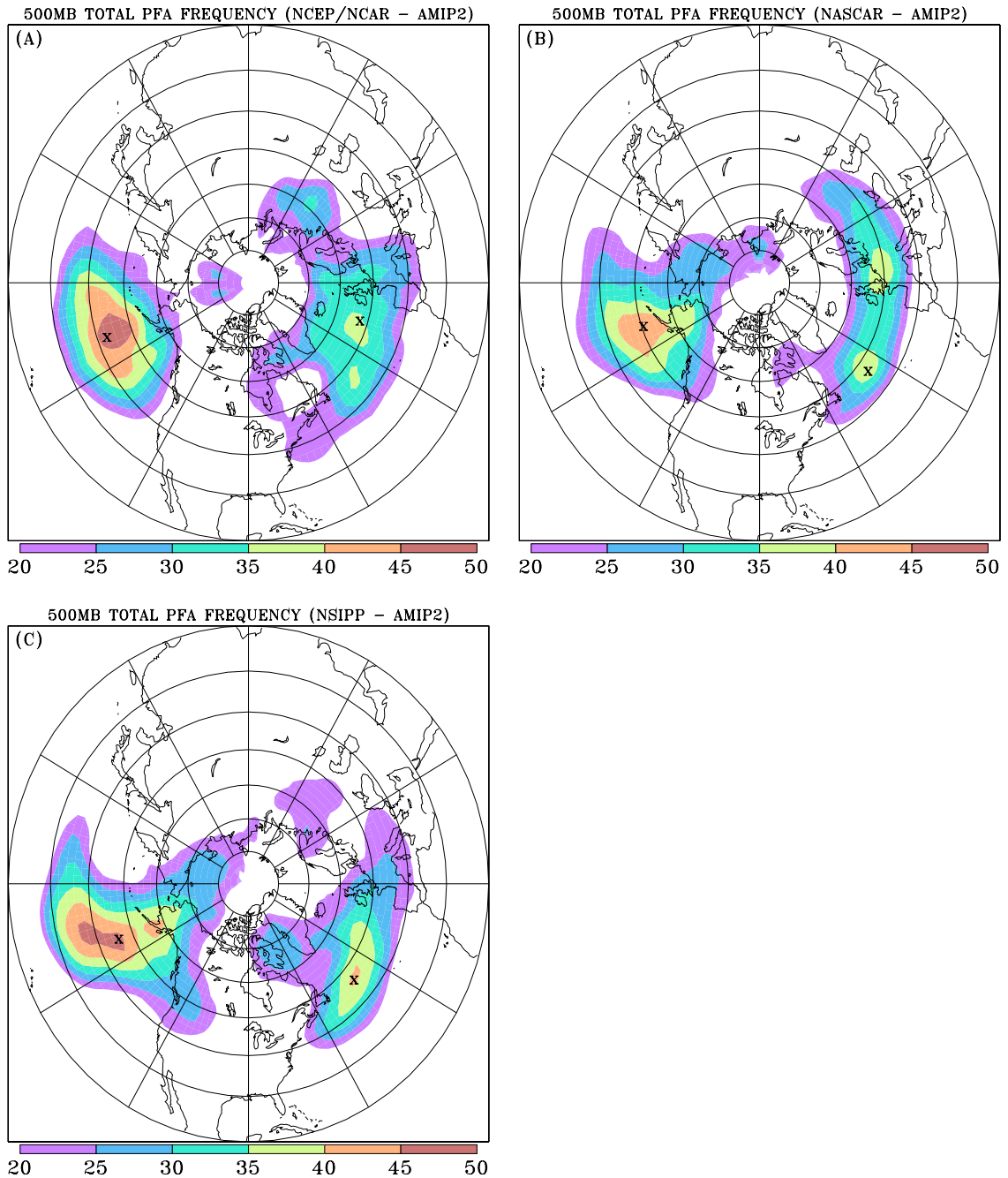


Figure 8: The regional frequency distribution (shading units: number of events per AMIP-2 period) of persistent flow anomalies at 500 *hPa* for (a) NCEP-NCAR reanalyses and (b) NASCAR and (c) NSIPP models. Events are selected using a 10 day, 100 *m* anomaly threshold. The key points marking the highest frequency of events are marked with an "X".

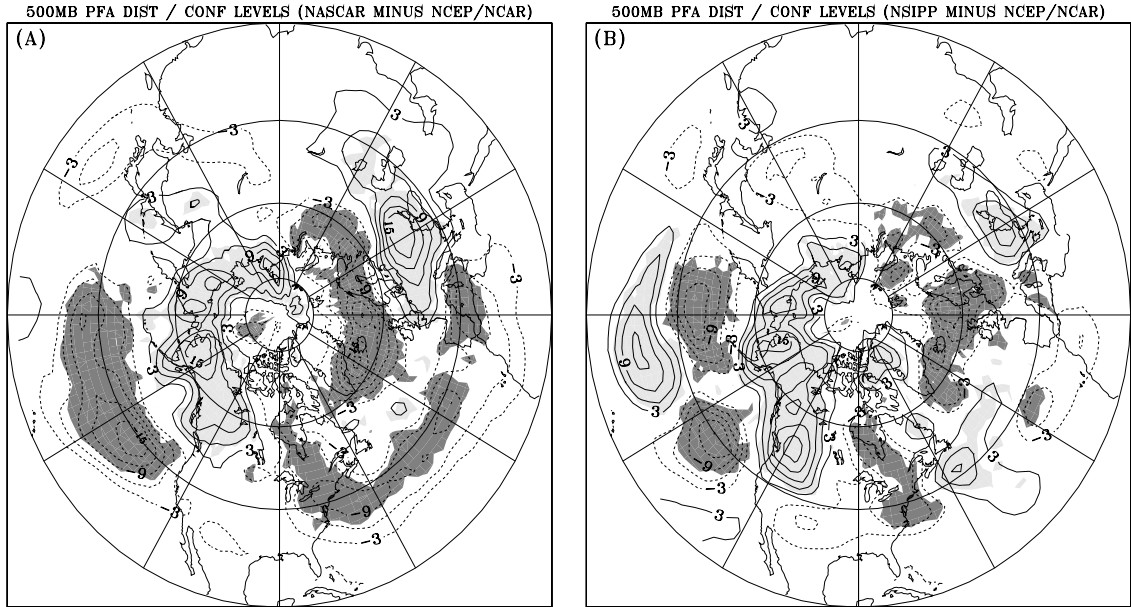


Figure 9: The difference in the total number of PFA events between the NCEP-NCAR reanalyses and (a) NASCAR and (b) NSIPP models (contour intervals: 3 cases per AMIP-2 period). Light (dark) shading indicates regions where the model exhibits positive (negative) biases that are significant at the 95% confidence level.

the other hand, it is evident that there are some differences in the regional frequency distribution *patterns*. For the NASCAR model there is a significant northward shift in the Pacific PFA distribution while the Atlantic distribution is anomalously narrow and extends too far east. For NSIPP, the Pacific distribution is latitudinally distended and longitudinally restricted and shifted to the west (compared to observations). These differences lead to the selection of different key points for the model events, as indicated in Figure 8. We next present composite analyses of LP anomaly fields for different classes of PFA events.

3.3.1 North Pacific composites

Over the Pacific key regions, each dataset exhibits strong symmetry between positive and negative PFA cases. Therefore, we choose to simultaneously discuss the anticyclonic (PACANT) and cyclonic (PACCYC) cases. The typical three dimensional anomaly structure for PACANT (PACCYC) cases is shown in Figure 10 (Fig. 11) by displaying the composite height anomalies at 300 and 1000 *hPa* for the three datasets. For observed anticyclonic

and cyclonic events the primary anomaly center over the North Pacific has a distinct zonally elongated anomaly structure (more so for the anticyclonic composite) with a slight westward tilt with height. Since the zonally elongated structure is positioned within the jet exit region, we expect such an anomaly will be associated with positive barotropic energy conversions from the climatological mean flow. For both cases in the NASCAR model, the horizontal perturbation structure is considerably more isotropic with slightly larger westward vertical tilts. The NSIPP model features primary anomaly structures with a horizontal major axis that is actually meridionally oriented and westward tilting vertical axis. Each model does a qualitatively good job reproducing the downstream wave train structure stretching across North America, which resembles the PNA teleconnection pattern of Wallace & Gutzler (1981).

The noted discrepancies in the structures of the PFAs provide insight into the composite dynamical interactions between PFAs and the mean flow. In particular compared to their observed counterparts, model events are more (less) likely to baroclinically (barotropically) extract energy from the climatological mean flow. This is verified in the following dynamical analyses of heat fluxes and E_{LP} vectors. The heat flux vectors associated with the PFA cases are calculated from the composite low-pass filtered horizontal wind and temperature anomaly fields. A similar process is used to compute the E_{LP} vectors for the PFAs. The left column in Figure 12 (Fig. 13) display the horizontal heat flux vectors of the PACANT (PACCYC) cases superposed upon contours of the climatological temperature field at 700 *hPa*. Regions having a strong positive baroclinic energy conversions are gray shaded. Consistent with the noted differences in the vertical structure, anomalously large poleward heat fluxes and positive baroclinic energy conversions are observed for the simulated events (Fig. 12b,c for PACANT and Fig. 13b,c for PACCYC events). Areal averages of the respective baroclinic conversions for PACANT (PACCYC) events are tabulated in the first row of Table 1a (Table 1b).

Figures 12d–f and 13d–f (right column on each page) plot the analogous E_{LP} vectors overlaying contours of the winter-averaged zonal wind field at 300 *hPa*. For observed events the E_{LP} vectors (Figs. 12d and 13d) in the Pacific jet exit region point westward

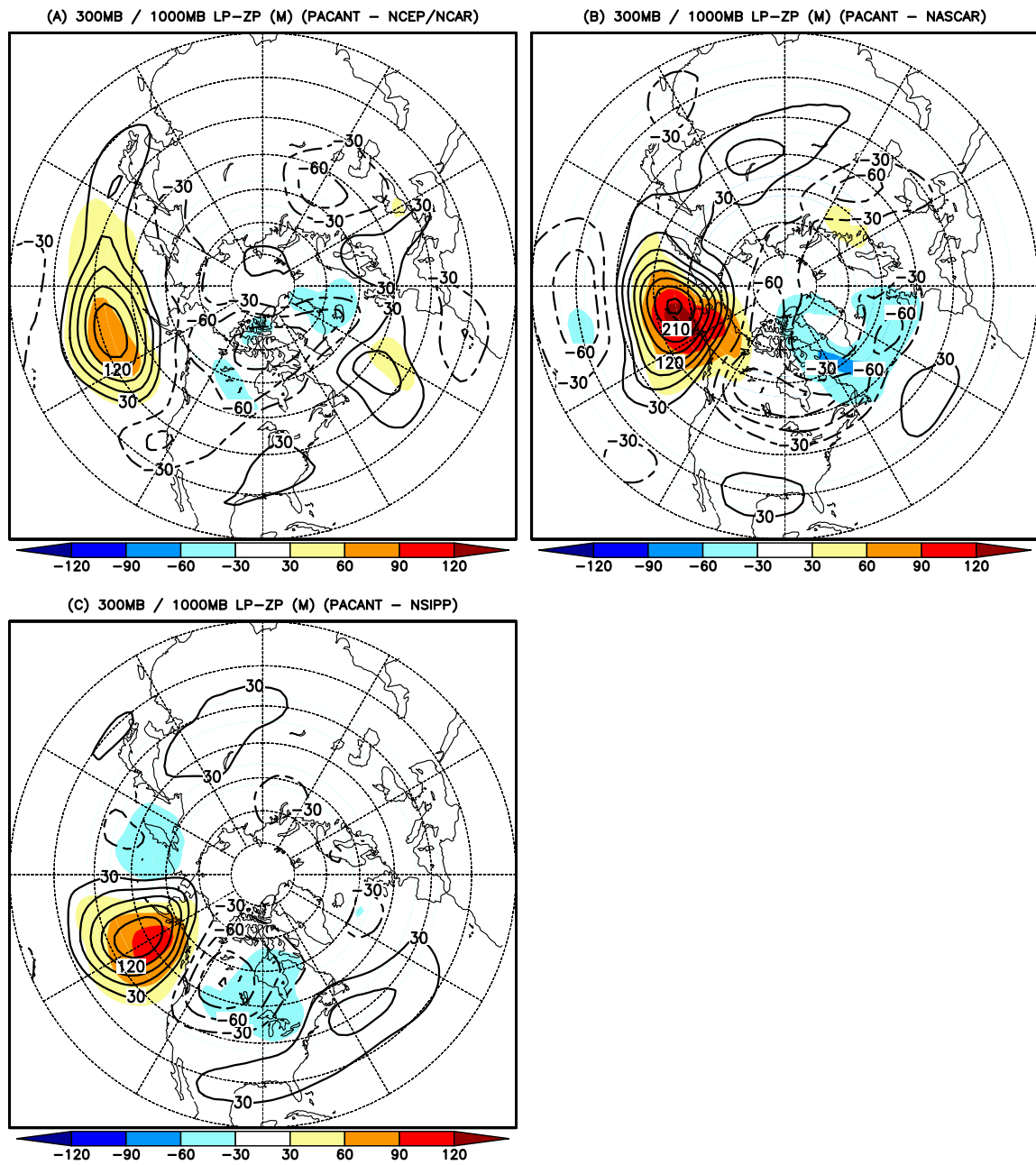


Figure 10: The composite height anomalies at 300 *hPa* (contour interval: 30 *m*) and 1000 *hPa* (color shaded regions) for anticyclonic PFA cases over the Pacific key region of the (a) NCEP-NCAR reanalyses and (b) NASCAR and (c) NSIPP models.

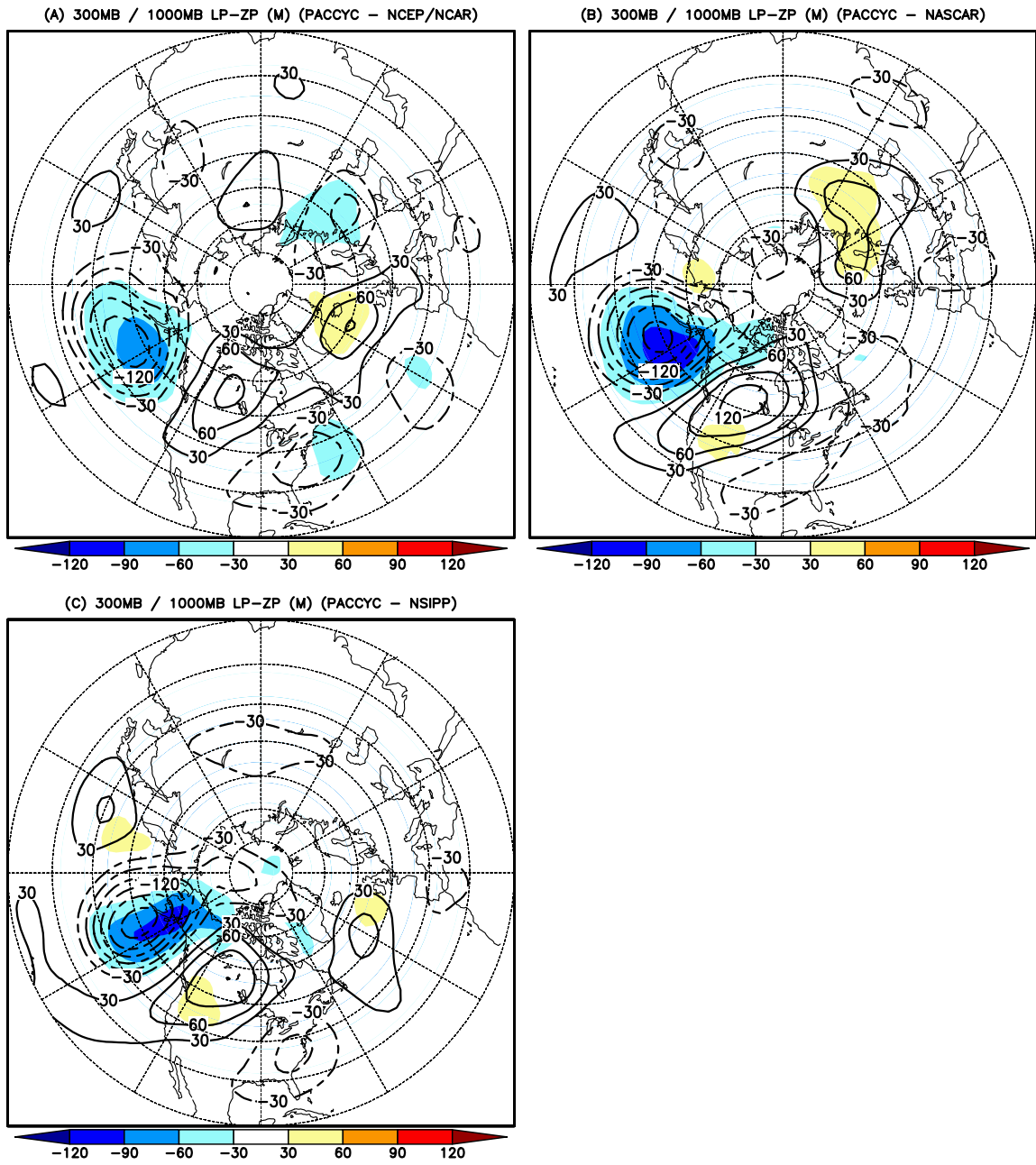


Figure 11: Same as Figure 10 except for Pacific cyclonic PFA cases.

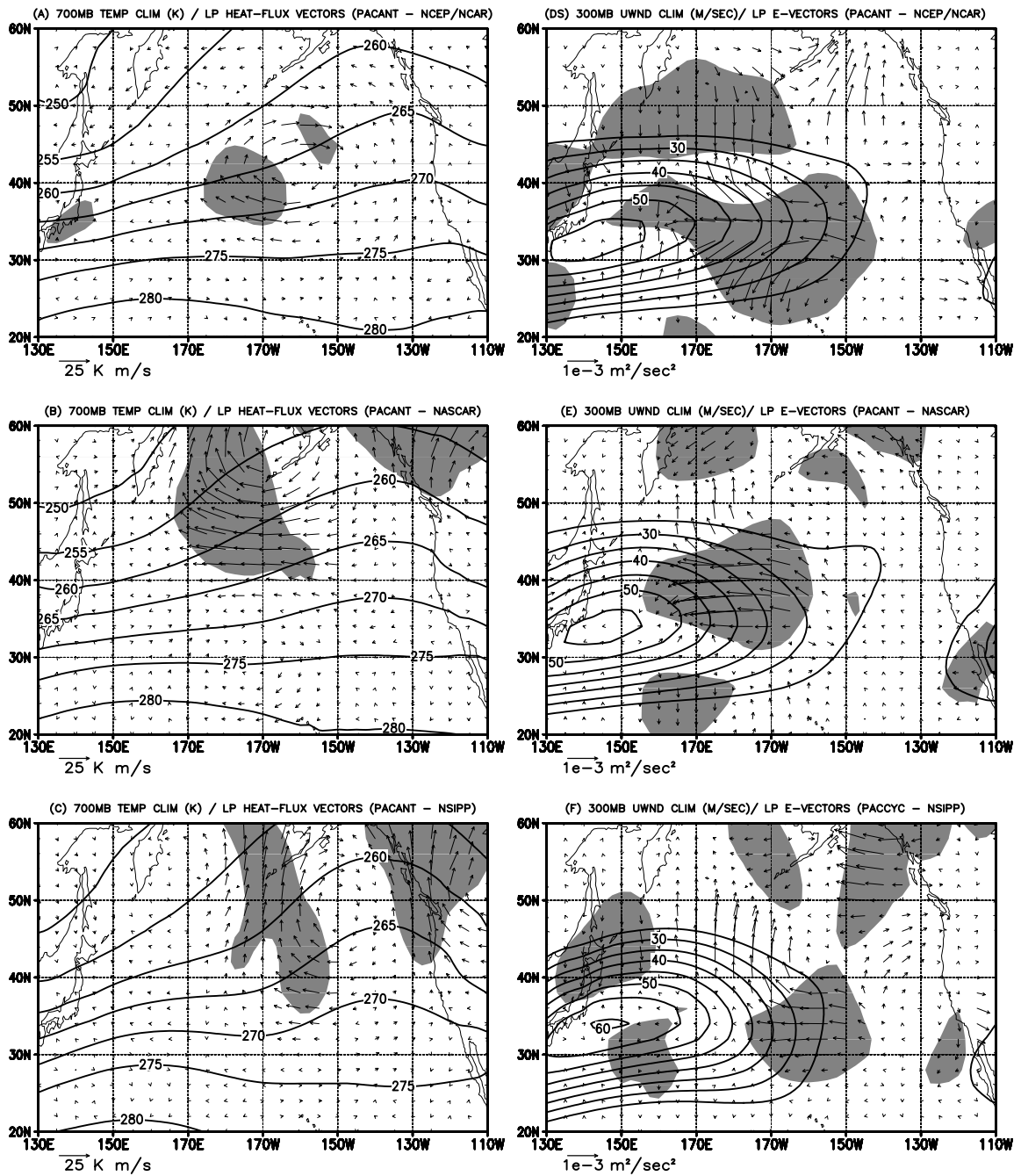


Figure 12: (a)-(c) Heat flux vectors (units: $K \cdot m \cdot s^{-1}$) overlaying the winter-averaged temperature field (contour intervals: 5 K) at 700 hPa and (d)-(f) E_{LP} vectors (units: $m^2 \cdot s^{-2}$) overlaying the winter-averaged zonal wind field (threshold: $25 m \cdot s^{-1}$; contour intervals: $5 m \cdot s^{-1}$) at 300 hPa computed from the anticyclonic Pacific PFAs for the NCEP-NCAR reanalyses and NASCAR and NSIPP models, respectively. Scale vectors are provided. Regions with baroclinic (barotropic) conversions greater than $1 \times 10^{-4} m^2 \cdot s^{-3}$ ($3 \times 10^{-3} K^2 \cdot s^{-1}$) are shaded in gray.

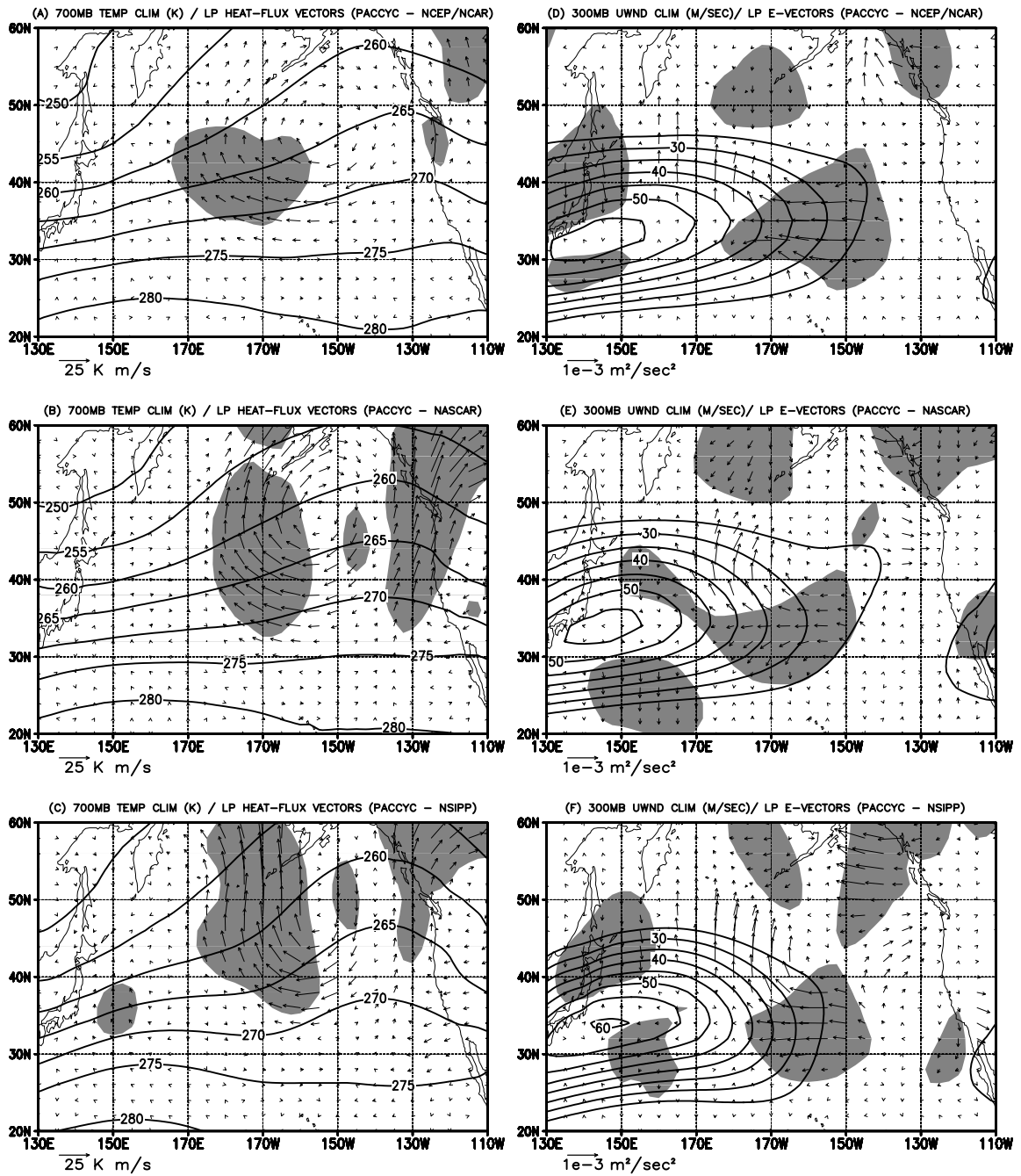


Figure 13: Same as Figure 12 except for Pacific cyclonic PFA cases.

(a) Pacific anticyclonic cases			
	NCEP-NCAR	NASCAR	NSIPP
700 <i>hPa</i> baroclinic conversions LP Anomalies ($10^{-5} K^2 \cdot s^{-1}$)	0.37	1.30	1.06
300 <i>hPa</i> barotropic conversions LP Anomalies ($10^{-5} m^3 \cdot s^{-3}$)	8.35	7.43	0.73
300 <i>hPa</i> barotropic conversions Synoptic Eddies ($10^{-5} m^3 \cdot s^{-3}$)	0.97	-1.52	-1.54
(b) Pacific cyclonic cases			
	NCEP-NCAR	NASCAR	NSIPP
700 <i>hPa</i> baroclinic conversions LP Anomalies ($10^{-5} K^2 \cdot s^{-1}$)	0.79	1.56	1.43
300 <i>hPa</i> barotropic conversions LP Anomalies ($10^{-5} m^3 \cdot s^{-3}$)	2.40	2.96	1.48
300 <i>hPa</i> barotropic conversions Synoptic Eddies ($10^{-5} m^3 \cdot s^{-3}$)	-0.28	-1.26	-0.98

Table 1: Average energy conversions for (a) anticyclonic and (b) cyclonic Pacific persistent flow anomalies for the NCEP-NCAR reanalyses and NASCAR and NSIPP models. Each values is time-averaged during the maintenance phases of the PFAs and areally-averaged from 20°N–90°N, 160°E–280°E.

toward larger values of the zonal wind (in sharp contrast to the earlier HP results) within a region of strong barotropic deformation (diffluence). This implies that barotropic extraction of kinetic energy from the mean flow likely contributes to maintaining observed large-scale Pacific weather regimes. For the models (Figs. 12e,f and 13e,f), the E_{LP} vectors also point westward in the exit regions of the Pacific jet; however the associated E_{LP} vectors are (i) weaker in magnitude and (ii) not optimally configured to take advantage of the maximum barotropic deformation field (which is shifted westward in the models). This results in anomalously weak barotropic energy conversions for the simulated Pacific PFA cases. (Areally averaged conversion values are presented in Table 1.)

Another potential contributor to PFA maintenance is the collective dynamical effect of case-to-case variability, especially the contributions of synoptic eddies which tend to be removed in the compositing process [e.g., Dole & Black (1990)]. Synoptic eddies have been shown to provide a positive barotropic contribution to low-frequency anomalies is past observational (Lau, 1988) and modeling studies (Higgins & Schubert, 1994). Therefore, it is of interest to assess the barotropic interaction between composite anomalies in the synoptic

(a) 700 hPa baroclinic conversions ($10^{-5} K^2 \cdot s^{-1}$)				
		Mean Flow		
		NCEP	NASCAR	NSIPP
Eddies	NCEP	0.37	0.31	0.24
	NASCAR	1.48	1.30	
	NSIPP	1.39		1.06

(b) 300 hPa barotropic conversions ($10^{-5} m^3 \cdot s^{-3}$)				
		Mean Flow		
		NCEP	NASCAR	NSIPP
Eddies	NCEP	8.35	6.70	7.96
	NASCAR	8.66	7.43	
	NSIPP	2.80		0.73

Table 2: Average (a) baroclinic energy conversions at 700 hPa and (b) barotropic energy conversions at 300 hPa for the composite anticyclonic PFAs for the NCEP-NCAR reanalyses, NASCAR and NSIPP models, and the swapped energy conversions.

(a) 700 hPa baroclinic conversions ($10^{-5} K^2 \cdot s^{-1}$)				
		Mean Flow		
		NCEP	NASCAR	NSIPP
Eddies	NCEP	0.79	0.67	0.61
	NASCAR	1.75	1.56	
	NSIPP	1.67		1.43

(b) 300 hPa barotropic conversions ($10^{-5} m^3 \cdot s^{-3}$)				
		Mean Flow		
		NCEP	NASCAR	NSIPP
Eddies	NCEP	2.40	0.74	1.50
	NASCAR	5.22	2.96	
	NSIPP	2.69		1.48

Table 3: Same as Table 2 except for Pacific cyclonic PFA cases.

eddy flux field and the large-scale flow¹. This is achieved by calculating the barotropic energy conversions between (i) **E** vectors constructed from the composite anomalies in the synoptic eddy flux field and (ii) a large-scale flow field that now includes the composite anomalies. In such a framework negative conversions imply that the synoptic eddies are losing energy to the large-scale circulation and vice versa.

To place such calculations into context, Table 1 contrasts areally averages of this new conversion term (row 3) along with parallel averages of the baroclinic and barotropic energy conversions presented in Figures 12 and 13 (i.e., the dynamical interaction between large-scale composite eddies and the climatological mean flow). Each value in Table 1 is areally averaged from 20°N to 90°N, 160°E to 280°E to encompass the horizontal extent of PFAs. We first note that the large-scale baroclinic energy conversions are much greater (more than double) in the GCMs than observations, while the large-scale barotropic conversions in the GCMs are less than half of the observed values (especially in NSIPP). This verifies our assertion of the relative roles of large-scale baroclinic and barotropic dynamics in the maintenance of observed and simulated PFA events. Interestingly, the net impact of synoptic eddies upon the large-scale flow field (Table 1, row 3) is negligible for the observed PFA events. On the other hand, the model cases are characterized by a positive barotropic feedback upon the large-scale flow that is comparable in magnitude to the large-scale barotropic conversion term (especially for NSIPP). We conclude that the model PFA events are characterized by (i) anomalously strong baroclinic conversions, (ii) anomalously weak barotropic conversions, and (iii) anomalously positive feedbacks from the synoptic-scale eddies.

We further examine the large-scale energy conversions to quantitatively test the relative roles of composite eddy structure and climatological mean flow structure in determining model simulated conversions. This is approached by separately swapping observed and model simulated eddy fluxes and background wind (temperature) field in calculating barotropic (baroclinic) energy conversions (Tables 2 and 3 for the PACANT and PACCYC

¹We note that this provides an upper bound on the contribution of synoptic eddies since synoptic eddies provide a baroclinic dissipation of the large-scale flow field (e.g., Lau, 1988).

cases, respectively). When the heat fluxes derived from the NCAR PFA cases are inserted into the mean flow of the GCMs, the values of the baroclinic energy conversions decrease to nearly the observed values. This clearly demonstrates that the noted structural differences in the simulated Pacific PFAs are the main factor leading to the anomalously large baroclinic conversions compared to observations (similarly, the model simulated conversions can be achieved by pairing the model eddy fluxes with the NCEP mean flow).

Tables 2b and 3b illustrate that the relative barotropic energy conversions decrease when the NCEP E_{HP} vectors are matched with the simulated mean flows, particularly for NASCAR. Conversely, when the simulated E_{HP} vectors are matched with the NCEP mean flow, the relative barotropic conversions increase yet remain substantially deficient compared to observed conversion values. As earlier noted, the upstream shift in the diffluent jet exit regions in the models is linked to a westward displacement of the downstream climatological ridge, which is located over the Gulf of Alaska in the models. Thus, model deficiencies in representing the climatological mean flow, especially the magnitude and structure of barotropic deformation in the jet exit regions, partly contribute to the anomalously weak barotropic dynamics observed in the GCMs. However, our results indicate that the main source of error is related to deficiencies in the simulated PFA structure (as for baroclinic conversions).

3.3.2 North Atlantic composites

We now examine the three-dimensional structure of composite PFAs over the North Atlantic. Since substantial asymmetries exist for the oppositely signed cases in the GCMs, here anticyclonic (ATLANT) and cyclonic (ATLCYC) cases are presented separately. Initially focusing on ATLANT cases, Figure 14 displays the 300 *hPa* and 1000 *hPa* composite anomalies for the three datasets. The primary anomaly feature in both model composites is anomalously weak compared to observations. In terms of horizontal structure, the NASCAR pattern (Fig. 14b) most closely resembles observed cases (Fig. 14a) as the primary and secondary (downstream) circulation anomaly features exhibit southwest to northeast horizontal tilts, with local anomalies resembling the East Atlantic teleconnection pattern

of Wallace & Gutzler (1981). For NSIPP, the primary anomaly structure is somewhat more zonally oriented with a downstream cyclonic anomaly that differs considerably from the other two datasets. Westward tilts with height are observed in all three composites.

Figures 15a–c plot the ATLANT heat flux vectors overlaid upon the climatological temperature field at 700 hPa (left column of Fig. 15). The heat flux vector pattern for NASCAR events (Fig. 15b) is similar to that of observations but with weaker vector magnitudes. The resulting baroclinic energy conversions are quantitatively similar, however, due to the anomalously strong horizontal temperature gradients in the NASCAR model. For the NSIPP cases, downgradient heat fluxes (and positive baroclinic energy conversions) are observed both to the southwest and northeast of the primary flow anomaly. The right column of Figure 15 displays the E_{LP} vectors and the winter-averaged zonal wind speeds at 300 hPa for the three datasets. In all three cases there are upgradient E_{LP} vectors indicating positive barotropic energy conversions. The primary difference is that the model E_{LP} vectors have weaker amplitudes than their observational counterparts. However, this effect is largely offset by anomalously strong horizontal gradients in \bar{U} that exist in the model simulations, leading to comparable values in the resulting barotropic energy conversions. Overall, we find that both baroclinic and barotropic conversions act to maintain the observed anticyclonic weather regimes over the Atlantic, aspects of which are fairly well simulated by both models.

The composite results for the ATLCYC cases are displayed in Figures 16 and 17. As previously noted, asymmetries exist between the respective model representations of Atlantic anticyclonic and cyclonic cases. In contrast to ATLANT events, the NSIPP model provides a better representation of the horizontal structure of ATLCYC than does NASCAR (Fig. 16b). For NASCAR events, the main circulation anomaly is oriented from northwest to southeast, unlike the southwest to northeast horizontal tilt observed for NCEP and NSIPP events. Interestingly, there are some structural parallels between NASCAR ATLCYC events and NSIPP ATLANT events, especially with respect to the downstream anomaly structures (cf. Figs. 16b and 14c). As observed for anticyclonic events, the model cases are generally too weak in amplitude compared to their observational counterparts (especially NSIPP)

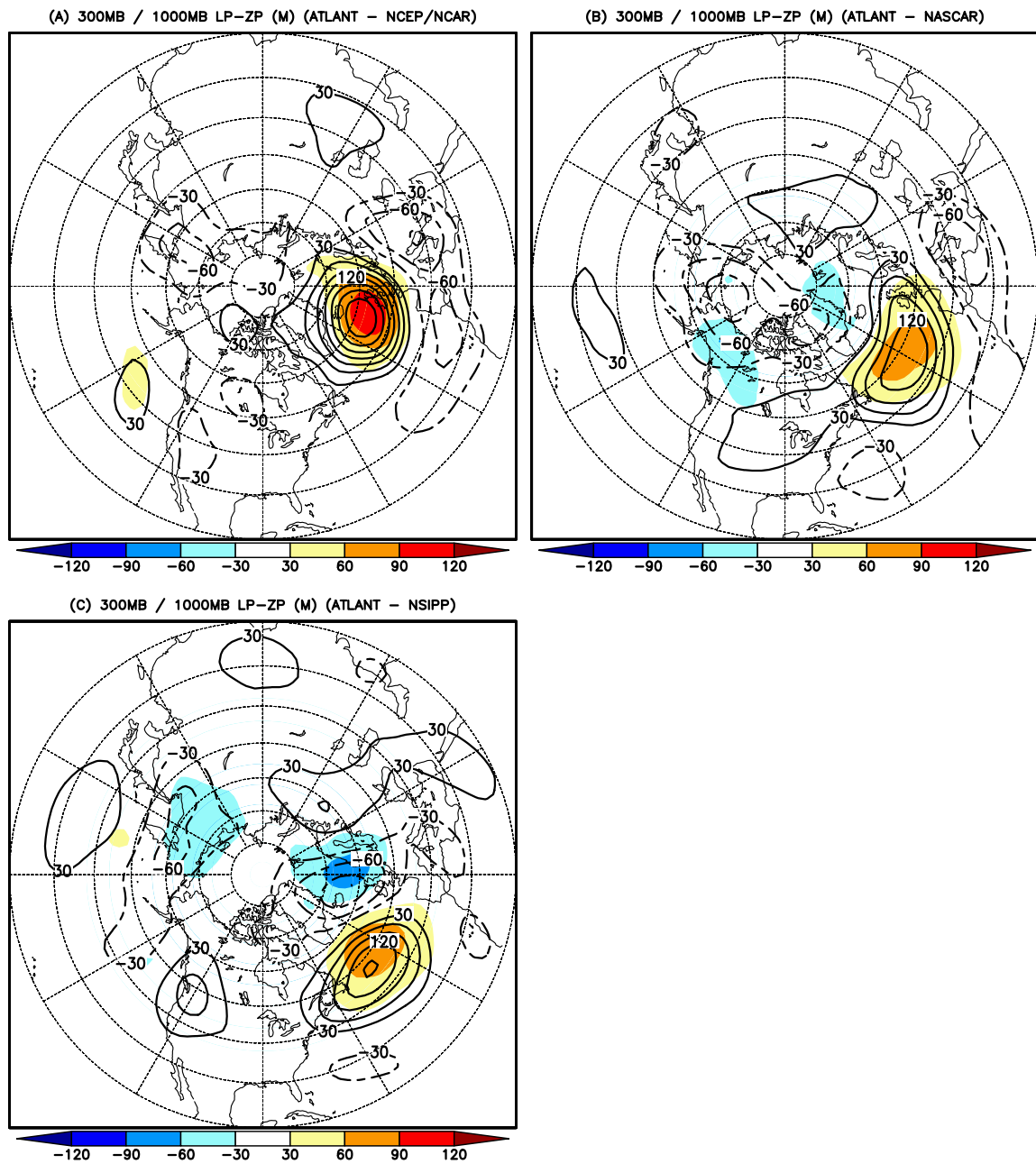


Figure 14: Same as Figure 10 except for Atlantic anticyclonic PFA cases.

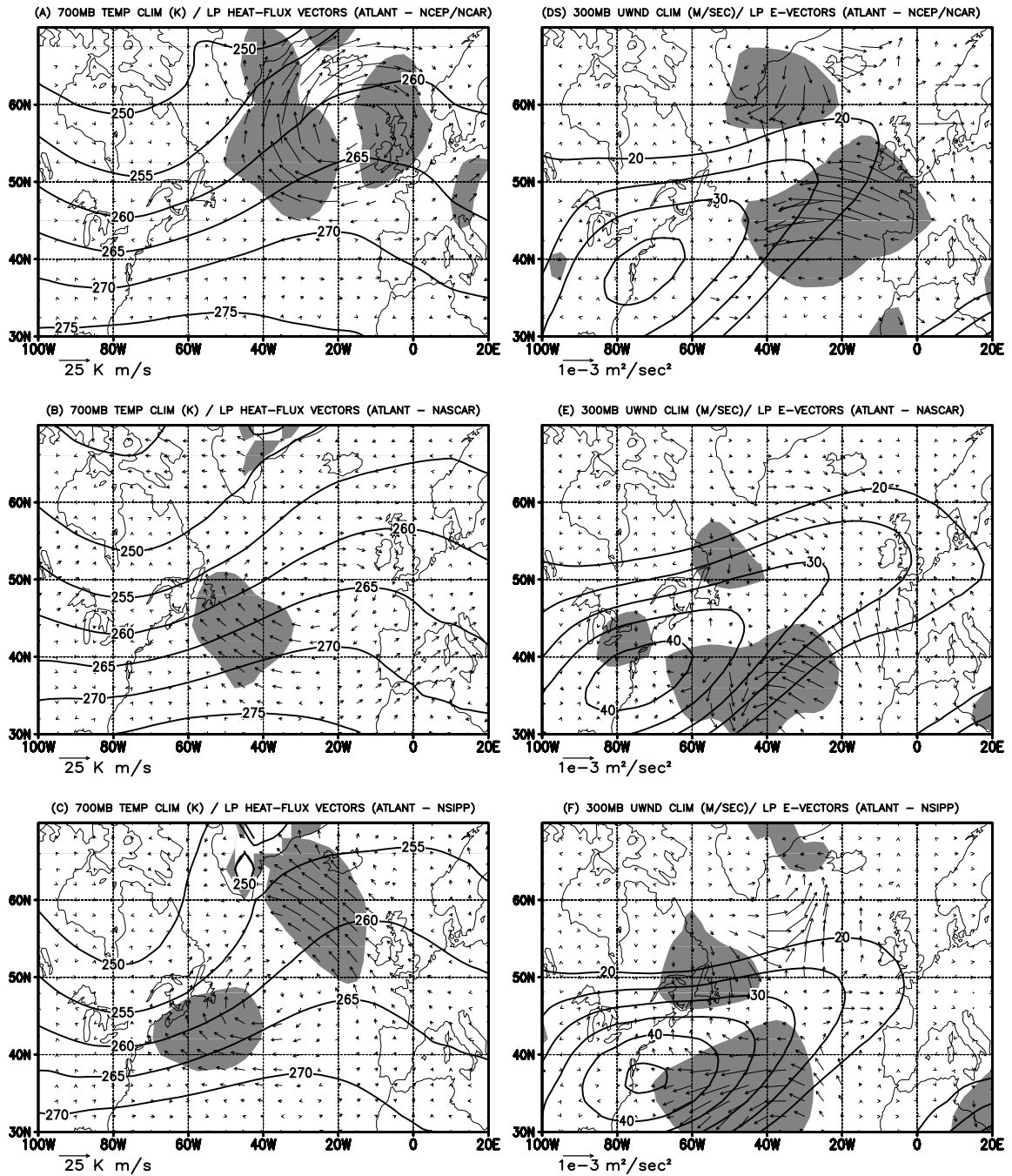


Figure 15: Same as Figure 12 except for Atlantic anticyclonic PFA cases.

and tilt westward with respect to height.

Composite plot of the associated horizontal heat fluxes show qualitatively similar patterns among the three composites (left column of Fig. 17). The primary difference is the relative weakness of the heat flux patterns associated with the model events. Local baroclinic energy conversion analyses reveal that for the NASCAR model this is offset by anomalously strong horizontal temperature gradients (similar to the ATLANT results). The resulting conversions for NSIPP events are anomalously low, however, due to the relative weakness in composite anomaly magnitude. Parallel plots of the horizontal \mathbf{E}_{LP} vectors (right column of Fig. 17) show that the observed vector magnitudes are generally greater than that of either model. Similar to the ATLANT cases, however, the NASCAR barotropic energy conversions are comparable to observations because the anomalously strong horizontal gradients in \bar{U} in the model simulation (Fig. 17e). On the other hand, the \mathbf{E}_{LP} vector patterns for the NSIPP events are not optimally aligned to efficiently extract energy barotropically from the climatological mean flow. In summary, although NASCAR ATLANT events exhibit some structural differences with the observed events, they are maintained by comparable values of baroclinic and barotropic energy conversions. This is partly attributable to differences in the structure of the mean flow over the North Atlantic compared to observations. NSIPP ATLANT cases are relatively weak in terms of both the anomaly amplitude and large-scale dynamical forcing.

Chen & van den Dool (2003) recently studied teleconnection patterns over the North Atlantic and found a regional sensitivity among patterns identified in different parts of the region. We test for such sensitivity in our observed cases by creating cyclonic and anticyclonic composites using a new "key point" located at $42.5^{\circ}\text{N}, 42.5^{\circ}\text{W}$, which is closer to the key points obtained in the GCMs. The 300 and 1000 *hPa* composite anomalies for both the cyclonic and anticyclonic cases are plotted in Figure 18. Similar to the composite analysis of the models, we now find rather asymmetric patterns in which the ATLANT pattern exhibits a zonally elongated monopole structure while the ATLANT pattern is characterized by a strong horizontal north-south dipole structure (quite different from Fig. 14). We note that the observed ATLANT structure for the new key point (Fig. 18a)

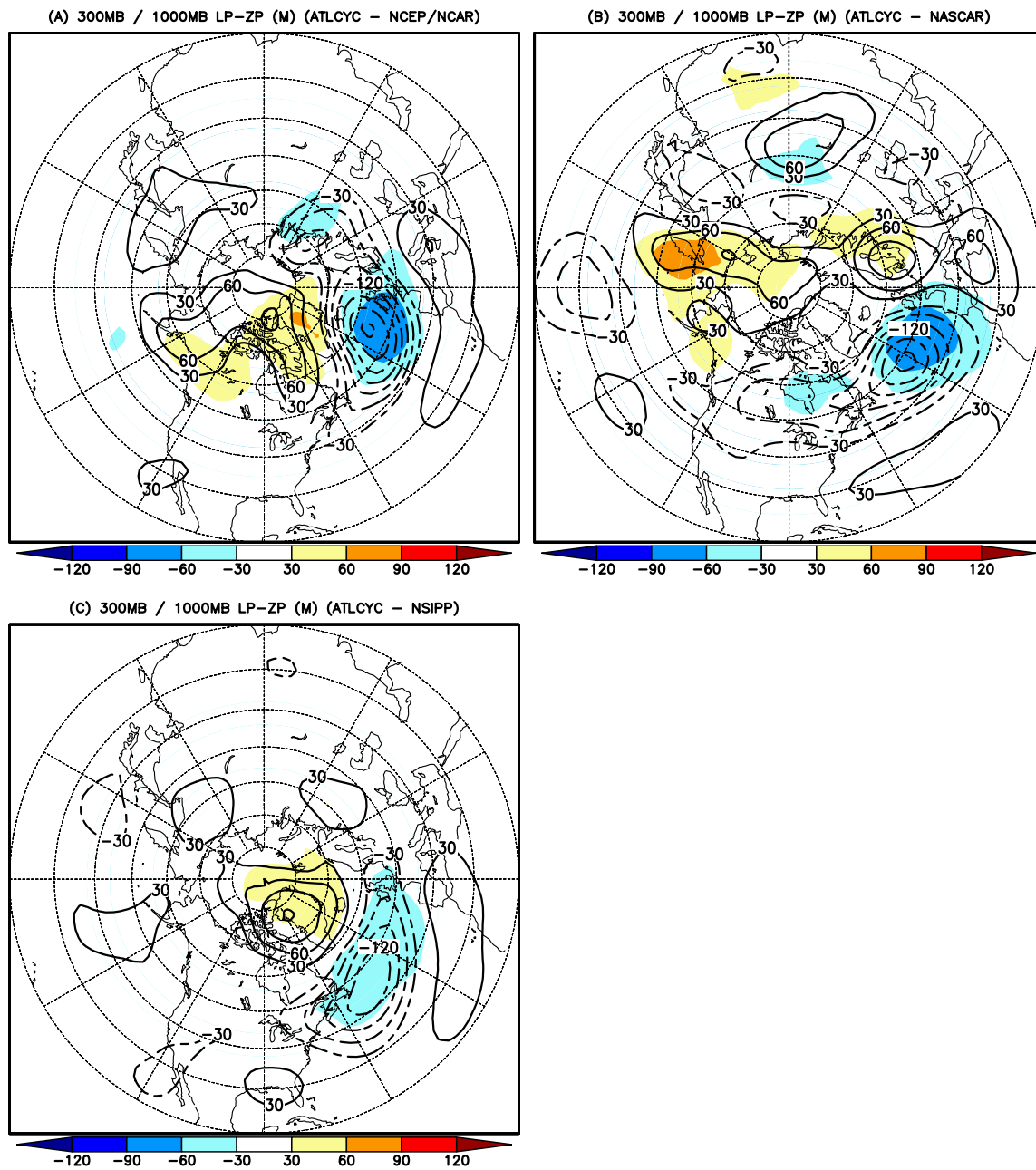


Figure 16: Same as Figure 10 except for Atlantic cyclonic PFA cases.

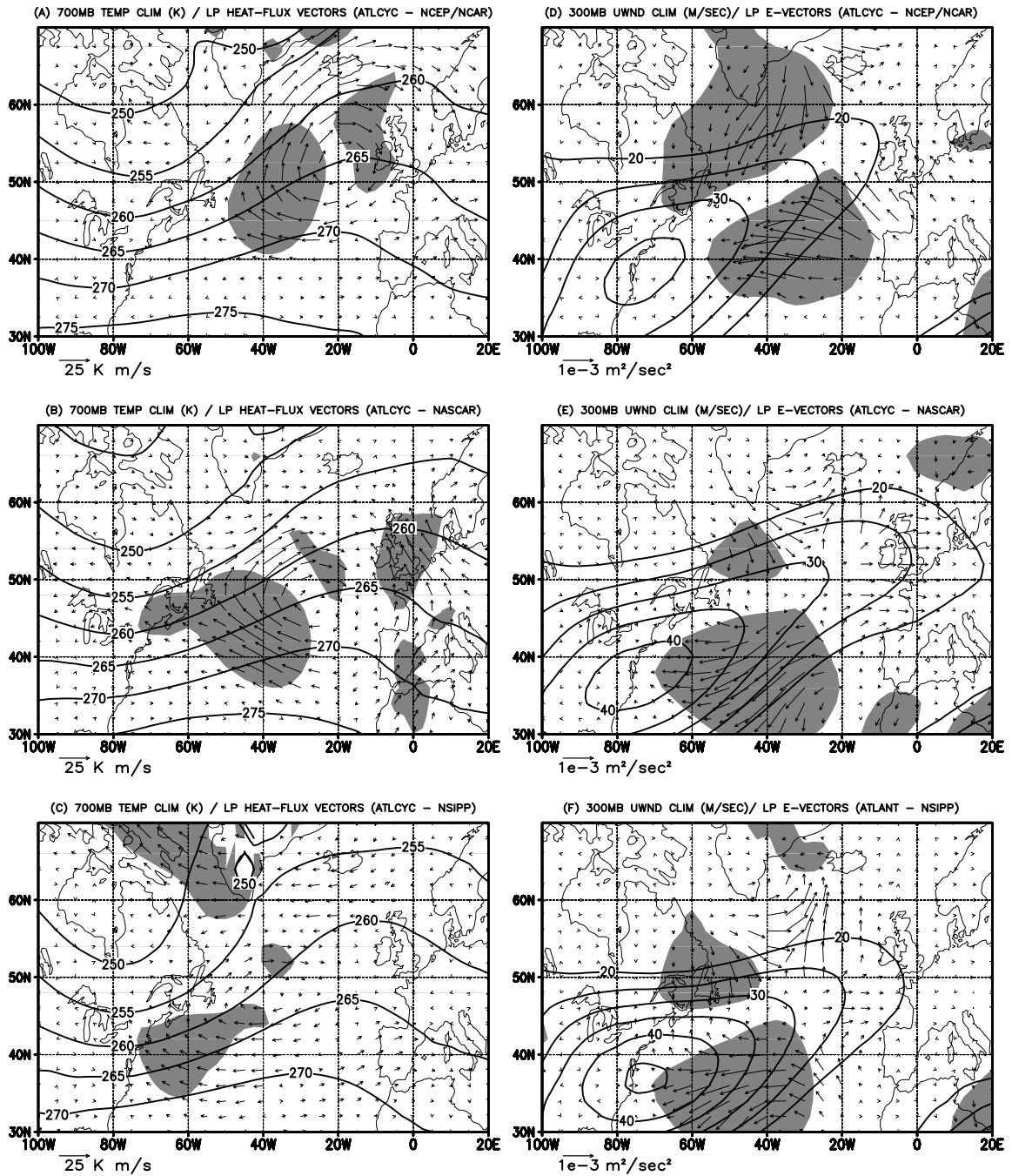


Figure 17: Same as Figure 12 except for Atlantic cyclonic PFA cases.

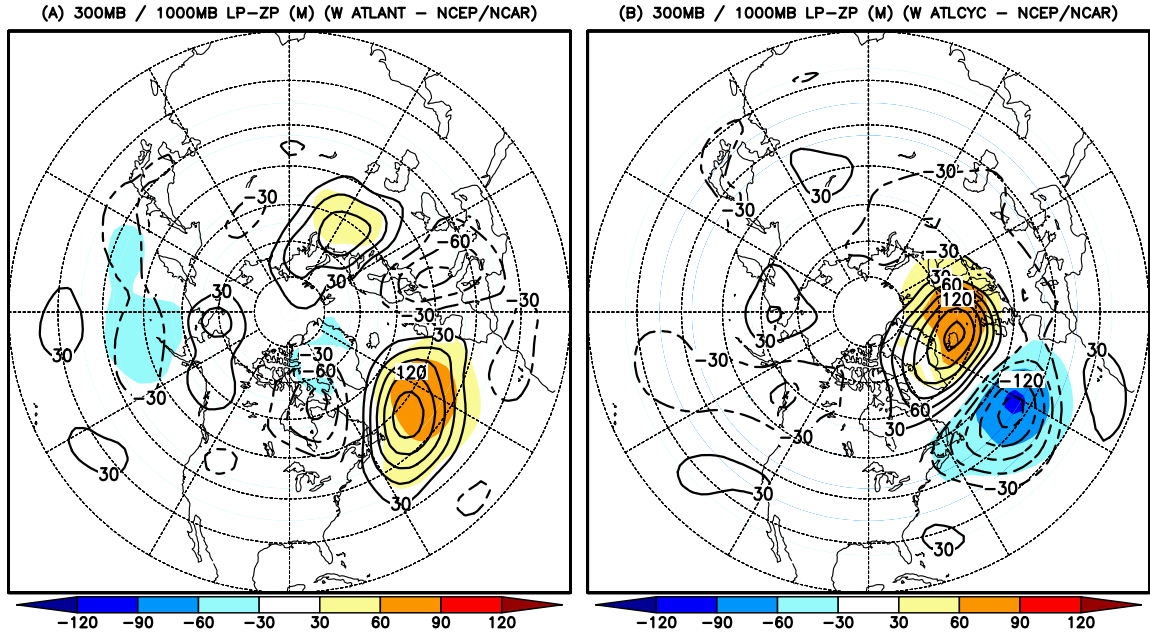


Figure 18: Composite height anomalies at 300 *hPa* (contour interval: 30 *m*) and 1000 *hPa* (color shaded regions) for (a) anticyclonic and (b) cyclonic PFA cases at the point 42.5°N, 42.5°W for NCEP-NCAR reanalyses. The key point used for the original composite of Atlantic PFAs in the reanalyses is 52.5°N, 25.5°W.

resembles both the NSIPP ATLANT (Fig. 14c) and NASCAR ATLCYC (Fig. 16b) patterns, all of which are characterized by monopole structures with oppositely signed anomalies located downstream to the northeast. Conversely, the north-south dipole structure found in Fig. 18b is partly evident in both the NASCAR ATLANT (Fig. 14b) and NSIPP ATLCYC (Fig. 16c) patterns. We conclude that some of the structural differences observed in Figs. 14 and 16 may be associated with the regional sensitivity observed to exist in the northern Atlantic.

3.4 Summary

A qualitatively good representation of the vertical structure of intraseasonal eddy kinetic energy (EKE) is provided by both models with maximum values of EKE occurring near 300 *hPa*. The main model shortcoming is an underestimation of EKE in the upper troposphere, especially for synoptic eddies in the NSIPP model. Nonetheless, both models provide a reasonable representation of the three-dimensional structure and dynamical characteristics

of synoptic eddies. Discrepancies in the storm track structures simulated by the models include an anomalous local minimum over the eastern Pacific basin. However, both GCMs faithfully reproduce the observed Pacific midwinter storm track suppression. Interestingly, the NSIPP model also produces a midwinter suppression feature over the Atlantic storm track in association with anomalously strong upper-level jet stream simulated by NSIPP in this region.

The regional distribution of anomalous weather regime events is well simulated by the models. However, substantial structural differences exist between observed and simulated events over the North Pacific region. In comparison to observations, model events are horizontally more isotropic, have stronger westward vertical tilts, and are more strongly driven by baroclinic dynamics. The structure and dynamics of anomalous weather regimes occurring over the North Atlantic region are qualitatively better represented by the models. It is suggested that model deficiencies in representing the zonally asymmetric climatological mean flow field (particularly the magnitude and structure of the Pacific and Atlantic jet streams) help contribute to model shortcomings in (i) the strength and seasonal variability of the storm tracks and (ii) dynamical distinctions in the maintenance of large-scale weather regimes.

CHAPTER IV

COMPARATIVE STUDY OF BAROCLINIC DEVELOPMENT

The previous chapter examined the time averaged statistics and structure of midlatitude storm tracks in AMIP-type simulations of the NASCAR and NSIPP GCMs. It was found that both models have important shortcomings in representing the regional structure and magnitude of the primary storm tracks. In particular, the simulated synoptic eddy activity tends to be too weak compared to observations (especially NSIPP), while low-frequency events in the GCMs are more strongly driven by baroclinic dynamics (primarily over the Pacific region). Nonetheless, both models reproduce a midwinter suppression in the Pacific climatological storm tracks. Interestingly, the NSIPP model also produces a midwinter suppression within the Atlantic climatological storm track (Figure 7f).

In this chapter, we study the structure and dynamical properties of growing baroclinic waves in the storm track regions for NASA GSFC GCM simulations and compare the results with parallel observational analyses derived from the NCEP-NCAR reanalyses. Our general approach is to perform lag composite analyses of discrete cyclonic and anticyclonic events, focusing on the period of anomaly growth (negative lags). Our research objectives are twofold: We first wish to assess the fundamental model representation of the structure and dynamics of anticyclogenesis and cyclogenesis events considering the winter season as a whole. An ancillary goal is to comparatively diagnose cyclogenesis activity for seasonally stratified periods to isolate the period of the midwinter suppression. In the former case, we present results focusing on the winter-averaged properties of growing synoptic eddies. For the latter, we present parallel assessments of growing cyclones by partitioning the cool season into three distinct parts: late fall/early winter, midwinter, and late winter/early spring. The results for the early and late stages are then contrasted with midwinter results.

4.1 Methodology

Composite analyses of unfiltered, daily-averaged anomalies are performed for the observational (NCEP-NCAR reanalyses) and simulated (NASCAR and NSIPP) datasets. In this chapter, daily anomalies are computed by successively subtracting (a) the daily climatology (see 2.3) and (b) the interannual (seasonal mean) anomalies from the raw data. Removing the seasonal cycle and seasonal mean from the raw data results in unfiltered anomalies with variations less than 90 days. Two measures of synoptic-scale variability are used as references to select events for compositing. First, anticyclonic (cyclonic) events are identified from relative maxima (minimum) in geopotential height associated with synoptic eddies at a core point in each of the climatological storm tracks. A time-series of the HP-filtered 300 *hPa* geopotential height anomaly is utilized to identify the events. Once the synoptic events are identified, the 300 *hPa* envelope function of Nakamura & Wallace ((see 2.3) 1990) is areally averaged ($\pm 10^\circ$ longitude and $\pm 5^\circ$ latitude) over each climatological storm track core region, and a minimum threshold value is applied to identify suitable dates from compositing (defined as Day 0). Using this threshold value assures that the events composited are of coherent wave packets propagating through the core of the climatological storm tracks. The choice of the threshold is arbitrary, and the results presented are not sensitive to the exact value. In this presentation, we use a threshold value corresponding to 0.75σ , which gives us about 120 events over the DJF period and 80–90 cases during each stage of the cool season. Our assessment of synoptic eddy growth upstream of the storm track focuses on the composite fields at Day -1 , since the largest growth typically takes place during this time.

The lag composite anomaly fields are then used to directly infer key information regarding the three dimensional structure and dynamical interactions of synoptic eddies for the different observational and model categories discussed earlier. In the current study we assess the areally-averaged baroclinic and barotropic energy conversions occurring between the composite eddy field and the climatological mean flow during synoptic eddy growth. This approach follows the diagnostics explained in 2.4 and 2.5 and used in the

study of the mean dynamical characteristics of persistent flow anomalies.

4.2 *Winter mean characteristics*

The first part of this chapter focuses on the winter-averaged properties of growing synoptic eddies located just upstream of the core regions of the storm tracks, where winter is defined as the 90-day period from 1–December to 28–February (DJF). Specifically, we study the Day –1 features of cyclonic and anticyclonic synoptic eddies in the North Pacific and North Atlantic storm tracks using both observations and model simulations. Supplementing the material presented in this section, the previous chapter provided detailed comparison of the winter-averaged zonally asymmetric circulation among the NASCAR and NSIPP simulations and NCEP/NCAR reanalyses.

As a practical first step in this analysis the vertical structure of the horizontally averaged eddy strength during growth is presented. Figure 19 displays the vertical profile of the DJF and areally-averaged eddy kinetic energy (EKE) associated with each case at Day –1, where the horizontal extent of the averaging is chosen to encompass the entire wave packet. Generally speaking, EKE increases less quickly with respect to height for the GCM events (especially NSIPP) compared to the observed events. This relationship holds for both models over the Pacific storm track and for NSIPP over the Atlantic storm track. The NASCAR model generally compares better with the observed profiles, actually exceeding the observed profile throughout the troposphere for Atlantic cyclonic events. The NSIPP model is quite deficient in all cases except for Pacific anticyclonic cases, where it outperforms the NASCAR model. These results are consistent with the relative magnitudes of the simulated winter-mean storm tracks (see Figure 3). The main point to emphasize in Fig. 19 is that the upper-tropospheric EKE is underrepresented by the models in many of the event categories just as the eddy enters the period of strongest baroclinic development (Day –1).

To illustrate the three-dimensional circulation anomaly structure of the ensemble averages, Figures 20–23 superpose 300 *hPa* height anomalies (contours) with 700 *hPa* height

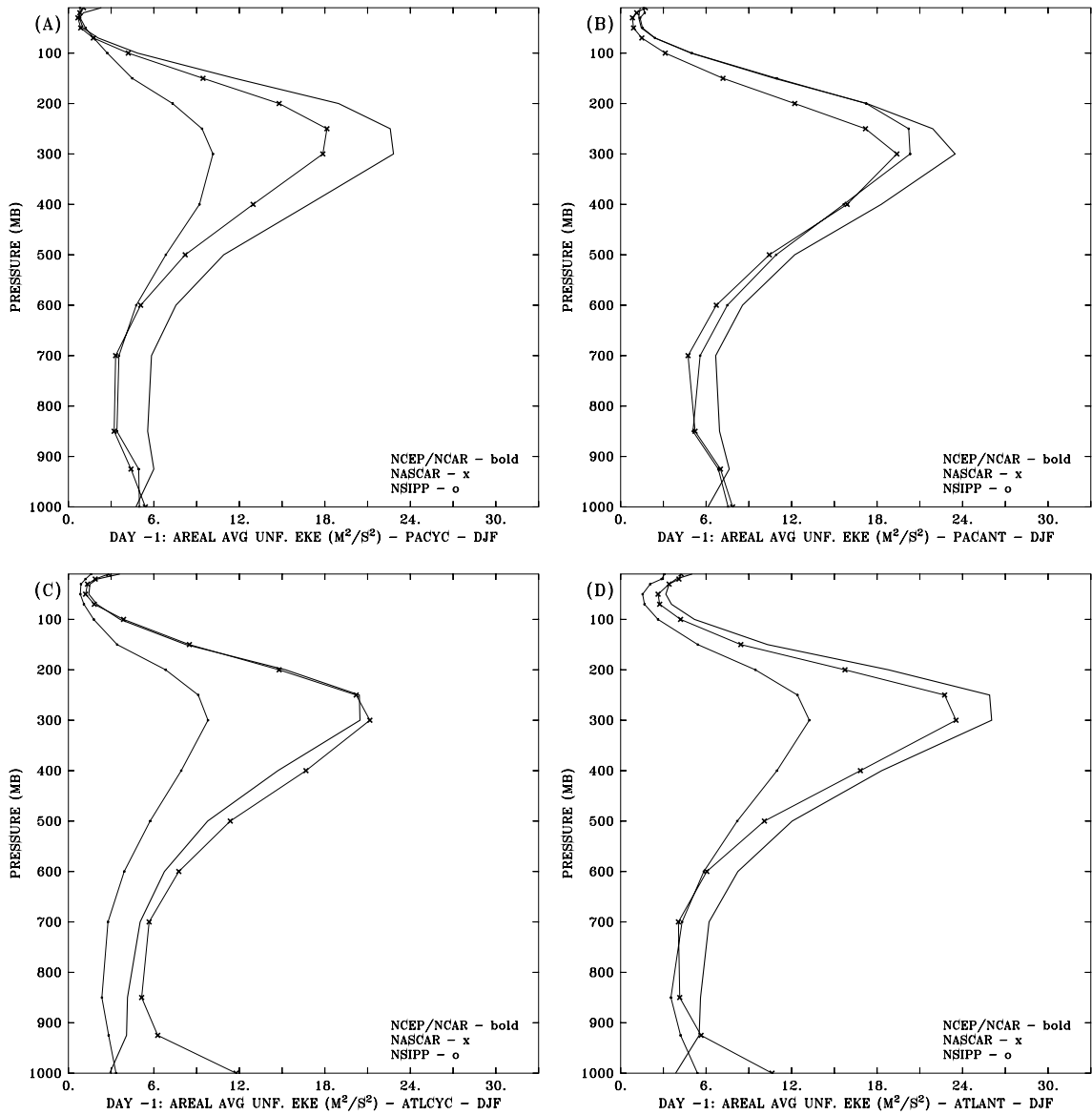


Figure 19: Vertical profiles of the areally-averaged eddy kinetic energy for each dataset derived from the winter-averaged unfiltered anomalies for (a) Pacific cyclonic, (b) Pacific anticyclonic, (c) Atlantic cyclonic, and (d) Atlantic anticyclonic cases. The averaging region is $20^{\circ}N-60^{\circ}N, 110^{\circ}E-230^{\circ}E$ for the Pacific cases and $30^{\circ}N-70^{\circ}N, 240^{\circ}E-360^{\circ}E$ for the Atlantic cases.

anomalies (shading) for the four event categories: Pacific cyclonic (PACCYC), Pacific anticyclonic (PACANT), Atlantic cyclonic (ATLCYC), and Atlantic anticyclonic (ATLANT). For PACCYC events, the primary (cyclonic) anomaly feature (160°–170°E) of the simulated events at both levels is weaker in amplitude, exhibits a greater SW-NE tilt, and has a greater meridional extent than observed events. In terms of vertical structure, the PACCYC events in observations and the NSIPP model exhibit a notable southwestward tilt with height, the southward component of which is exaggerated in the NSIPP model. This southward shift of the upper-level feature from its lower-level counterpart is reminiscent of the meridional trapping observed by Nakamura and Sampe (2002) in association with the midwinter suppression phenomenon. On the other hand, the NASCAR PACCYC cases exhibit westward tilts with height.

As illustrated in Figure 21, the GCMs do a much better job representing the magnitude and vertical structure of the growing anticyclonic feature of PACANT events. In fact, the local upper-level anomaly for the NSIPP cases is larger in magnitude than observations. (The discrepancy with Fig. 19b is attributable to the relative weakness of the upstream and downstream anomaly features in the NSIPP wave packet.) We note, however, that the model-simulated anticyclonic features have larger meridional extensions and there is slight SW-NE horizontal eddy tilt in the NSIPP model. We also note that the ensemble wave train in the NSIPP model exhibits a strong arcing toward the SE compared to the observed anomalies while the NASCAR wave train has a greater northeastward arc compared to observations.

Parallel analyses for the ATLCYC and ATLANT cases are displayed in Figures 22 and 23, respectively. Referring to the ATLCYC cases in Fig. 22, the three-dimensional *structure* of the primary anomaly features in the NASCAR model compares very well with the observed structure, although the simulated cyclone is anomalously deep. In both cases, the simulated cyclonic feature is meridionally elongated with a southwestward tilt with height. In the NSIPP model, growing ATLCYC events are considerably weaker in magnitude and more isotropic (weaker meridional distension). On the other hand, both models do a good job representing the longitudinal placement of the upper-level downstream anticyclonic

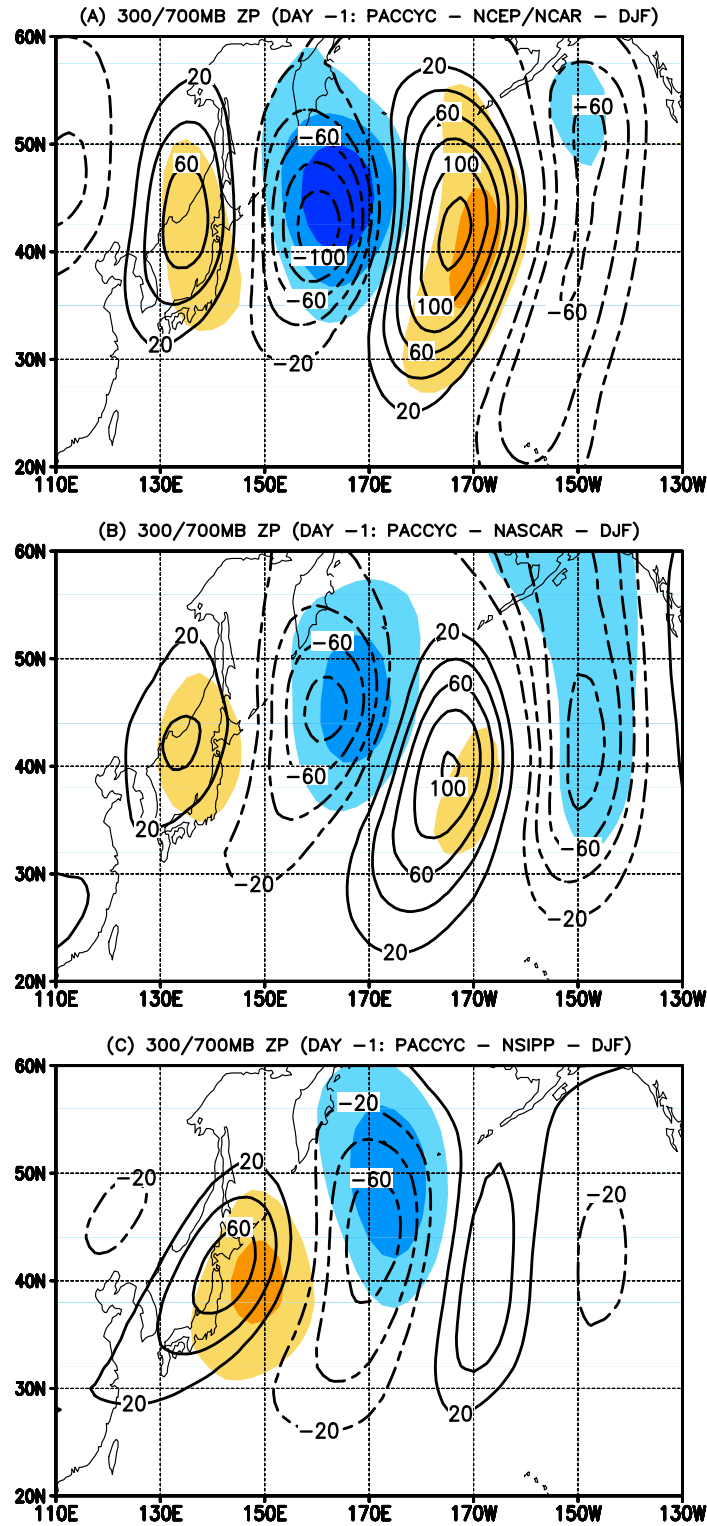


Figure 20: Winter-averaged composite height anomalies at 300 *hPa* (contour intervals: 20 *m*) and 700 *hPa* [orange (blue) shaded regions greater (less) than 20 (–20) *m* at 20 *m* intervals] for Pacific cyclonic cases at Day –1 for the (a) NCEP-NCAR reanalyses and (b) NASCAR and (c) NSIPP models. Day 0 is defined as when the synoptic eddies are at maximum amplitude in the core of the regional storm track.

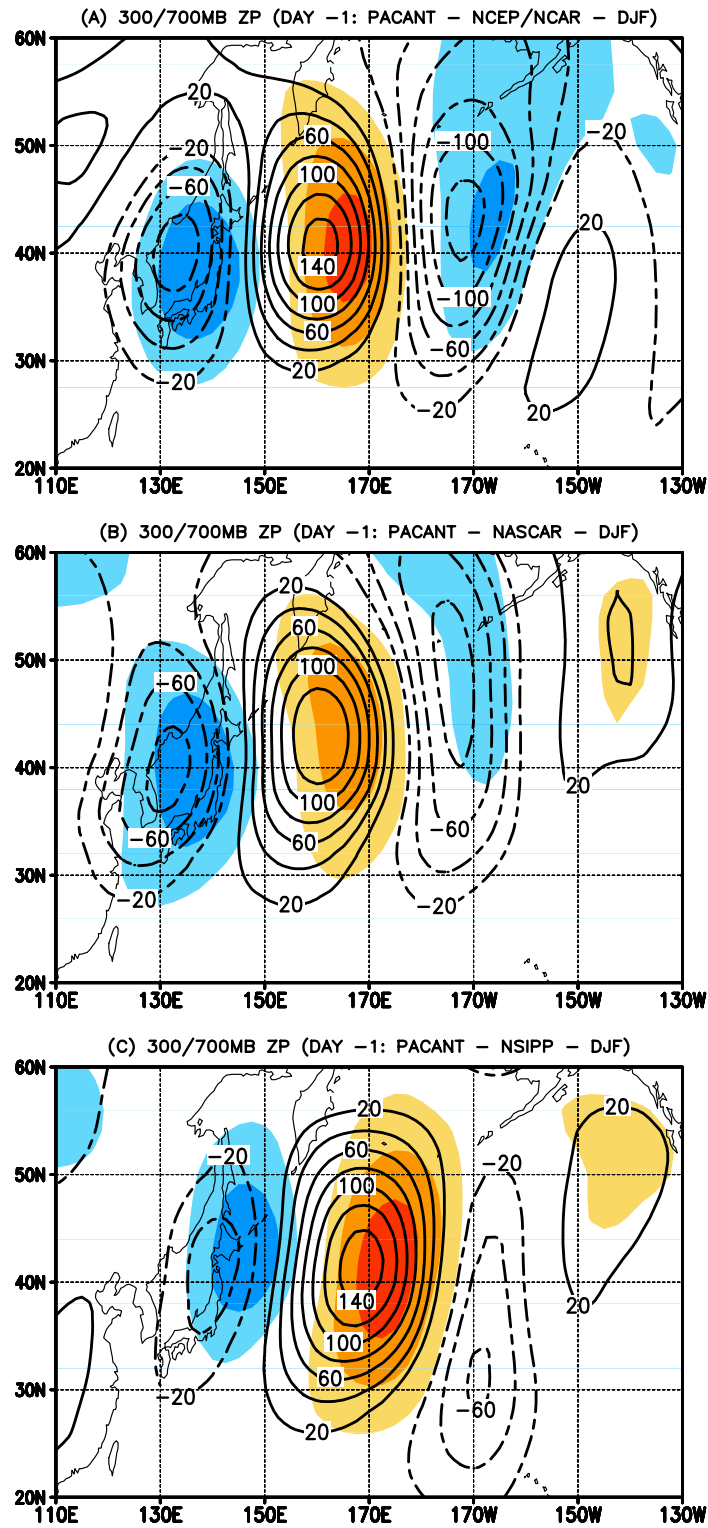


Figure 21: As in Figure 20 except for Pacific anticyclonic cases.

anomaly feature. For the ATLANT cases (Fig. 23) the anticyclonic feature in each model is anomalously weak and meridionally retracted in comparison to observations. In terms of the horizontal structure of the primary feature, while observed cases are meridionally aligned (N-S), the NASCAR (NSIPP) structures exhibit SW-NE (NW-SE) phase tilts. There are similar asymmetries in the great circle arcs of the two wave trains. In this case, the NSIPP pattern better corresponds to observations. Finally, it is of interest to note that in all three cases the downstream cyclonic circulation anomalies have notably greater amplitudes (unlike for PACANT events). This is consistent with the asymmetries in the relative structure and magnitude of cyclones and anticyclones predicted by nonquasigeostrophic models of baroclinic instability [e.g., Rotunno *et al.* (2000)].

For each of the categories discussed above, the areal-averaged baroclinic and barotropic energy conversions calculated at 700 and 300 *hPa*, respectively, are listed in Tables 4 and 5 (Pacific cases) and Tables 6 and 7 (Atlantic cases). To help assess the dynamical impact of the above-noted structural discrepancies between simulated and observed anomaly fields, we compute additional sets of energy conversions by respectively swapping the anomaly fields and climatological mean background flows among the datasets. These swapped conversions are also listed in Tables 4–7.

Initially focusing on the PACCYC (Table 4) and PACANT (Table 5) cases, the 700 *hPa* baroclinic energy conversions for the GCM cases are markedly lower than for observed events, especially in the NSIPP model where values are about 33% lower. Interestingly, when the eddy fluxes associated with the GCM composite anomalies are paired with the observed background flow, the baroclinic conversions are effectively unchanged. Conversely, when the observed eddy fluxes are paired with the simulated background flow fields, the observed conversion values are approximately replicated. The latter correspondence is fractionally better for NASCAR, indicating a relative weakness in NSIPP’s representation of the climatological mean flow. These results indicate that the simulated deficiencies in representing baroclinic energy conversions are primarily due to the misrepresentation of the synoptic eddy structure. For the NSIPP cases, there is a second-order influence that can be attributed to deficiencies in NSIPP’s representation of the background temperature

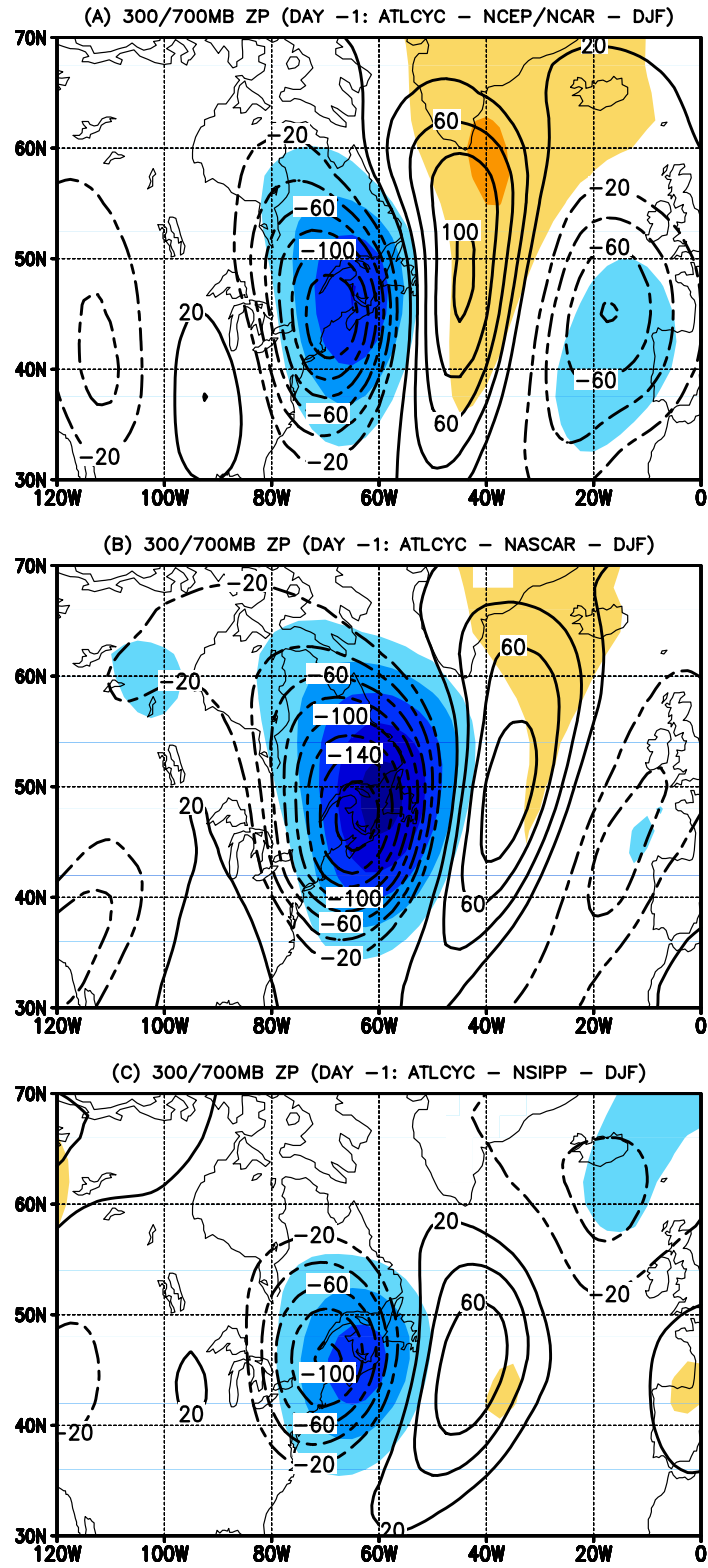


Figure 22: As in Figure 20 except for Atlantic cyclonic cases.

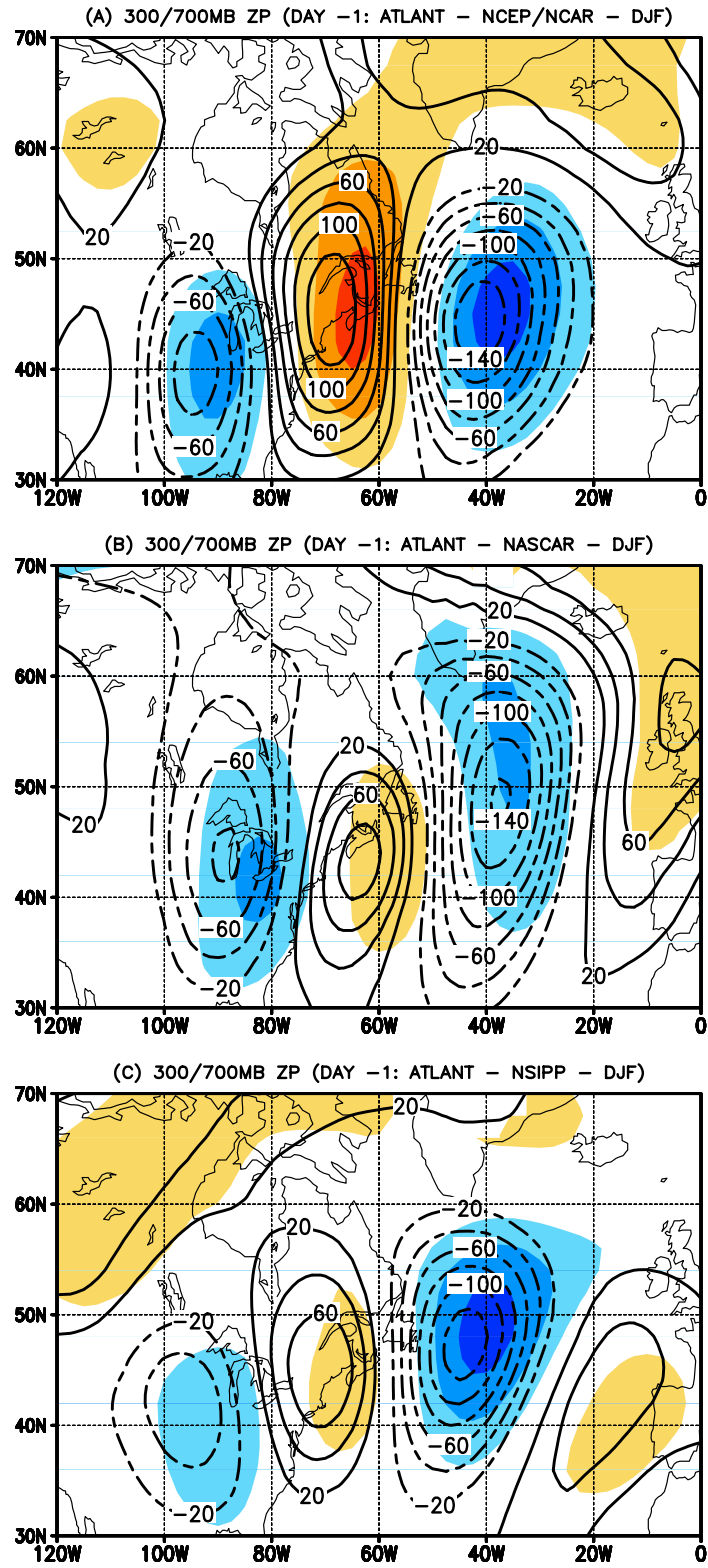


Figure 23: As in Figure 20 except for Atlantic anticyclonic cases.

PACCYC: Day -1, DJF				
(a) 700 hPa baroclinic conversions ($10^{-5} K^2 \cdot s^{-1}$)				
		Mean Flow		
		NCEP	NASCAR	NSIPP
Eddies	NCEP	1.97	1.96	1.84
	NASCAR	1.52	1.55	
	NSIPP	1.39		1.33
(b) 300 hPa barotropic conversions ($10^{-5} m^3 \cdot s^{-3}$)				
		Mean Flow		
		NCEP	NASCAR	NSIPP
Eddies	NCEP	-4.62	-4.68	-2.80
	NASCAR	-3.73	-3.82	
	NSIPP	-0.75		-1.23

Table 4: The winter-mean, areally-average (a) 700 hPa baroclinic and (b) 300 hPa barotropic energy conversions for Pacific cyclonic cases at Day -1 for the NCEP-NCAR reanalyses, NASCAR and NSIPP models, and the swapped energy conversions. The averaging region for the Pacific cases is 20°N–60°N, 110°E–230°E.

gradient.

Before discussing the details of the barotropic energy conversions in Tables 4 and 5, it is useful to note that baroclinic eddies (which are meridionally elongated) generally lose kinetic energy to the mean flow in the storm tracks, which are characterized by horizontal diffluence in the jet exit regions (Black & Dole, 2000). However, this energy loss can be locally offset if a disturbance has a SW-NE (NW-SE) horizontal anomaly tilt on the north (south) side of the jet axis. Referring to Fig. 20, we recall that the GCM-simulated PACCYC cases exhibit a greater SW-NE tilt. Since this feature occurs on the north side of the climatological jet, this will lead to an enhanced local transfer of kinetic energy from the mean flow into the eddies (Black & Dole, 2000). For the PACANT cases, we do not observe a strong model bias in the horizontal anomaly tilt, but we do observe a larger meridional elongation (Fig. 21). These differences in eddy structures for the Pacific cases are consistent with the variations in 300 hPa barotropic conversions observed in Tables 4 and 5. The eddy-mean flow swapping exercise confirms that this is indeed true for the NASCAR cases. However, a similar exercise performed for the NSIPP Pacific cases indicates that the background mean flow plays a larger role in determining the local barotropic energy

PACANT: Day -1, DJF				
(a) 700 hPa baroclinic conversions ($10^{-5} K^2 \cdot s^{-1}$)				
		Mean Flow		
		NCEP	NASCAR	NSIPP
Eddies	NCEP	3.58	3.58	3.42
	NASCAR	2.98	3.02	
	NSIPP	2.31		2.22
(b) 300 hPa barotropic conversions ($10^{-5} m^3 \cdot s^{-3}$)				
		Mean Flow		
		NCEP	NASCAR	NSIPP
Eddies	NCEP	-5.58	-5.48	-6.29
	NASCAR	-6.16	-6.12	
	NSIPP	-6.35		-5.92

Table 5: As in Table 4 except for Pacific anticyclonic cases.

conversion. In particular, barotropic damping of NSIPP Pacific cyclone events (Table 4) is anomalously weak in large part because of existing deficiencies in the background zonal wind field. In particular, the NSIPP model is characterized by a westward displacement and relative localization of the climatological barotropic deformation field compared to observations (see discussion in 3.1).

For the Atlantic cases (Tables 6 and 7), baroclinic conversions in the NSIPP model are seriously deficient (50% too low), which can be largely attributed to the structure and magnitude of the ATLCYC and ATLANT cases. This is confirmed by the eddy-mean flow swapping exercise as the NCEP and NSIPP background temperature configurations result in virtually identical energy conversions (for a given eddy heat flux field). Conversely, the NSIPP 300 hPa mean flow over the Atlantic region modestly impacts the relative barotropic conversions. For NASCAR, although the baroclinic conversions compare more favorably with NCEP, they are overestimated for ATLCYC events (Table 6). Although this is primarily due to the anomalously strong eddy magnitudes in the NASCAR events (Fig. 22b), it is also attributed to variations in the background temperature gradient. This is consistent with Figure 6 in 3.1 where the average temperature in proximity to the climatological stationary trough over Hudson Bar is considerably colder in the NASCAR model. Consequently, larger horizontal temperature gradients exist over the east coast of North America in

ATLCYC: Day -1, DJF				
(a) 700 hPa baroclinic conversions ($10^{-5} K^2 \cdot s^{-1}$)				
		Mean Flow		
		NCEP	NASCAR	NSIPP
Eddies	NCEP	2.37	2.58	2.25
	NASCAR	3.15	3.42	
	NSIPP	1.31		1.28
(b) 300 hPa barotropic conversions ($10^{-5} m^3 \cdot s^{-3}$)				
		Mean Flow		
		NCEP	NASCAR	NSIPP
Eddies	NCEP	-9.20	-9.80	-8.27
	NASCAR	-6.32	-6.75	
	NSIPP	-1.92		-0.75

Table 6: The winter-mean, areally-average (a) 700 hPa baroclinic and (b) 300 hPa barotropic energy conversions for Atlantic cyclonic cases at Day -1 for the NCEP-NCAR reanalyses, NASCAR and NSIPP models, and the swapped energy conversions. The averaging region for the Atlantic cases is 30°N–70°N, 240°E–360°E.

NASCAR. The results of eddy-mean flow swapping indicate the general tendency of the NASCAR temperature gradients to enhance the baroclinic energy conversion magnitudes over the North Atlantic storm track. Finally, we note that it is possible for errors in the simulated mean flow and eddy fields to feed back upon one another as (a) the mean flow helps determine the time-evolving eddy structure and (b) the eddy heat and momentum fluxes provide local alterations to the background flow field.

4.3 Seasonal stratification

We next apply similar diagnostic methods but focus on growing Pacific cyclones during different parts of the cool season. We first stratify the cool season into three stages: an early stage taken as November and December, a middle stage of January and February, and a late stage taken to be March and April. The early and late (middle) stages approximately correspond to the seasonal maxima (minimum) in synoptic eddy activity that occurs over the North Pacific in association with the midwinter suppression phenomena (e.g., refer back to Figure 7a-c). A core point marking the relative maximum of climatological synoptic eddy activity for each stage is chosen separately in each dataset. In doing so, we isolate the general characteristics of growing cyclones occurring within each stage taking account

ATLANT: Day -1, DJF				
(a) 700 hPa baroclinic conversions ($10^{-5} K^2 \cdot s^{-1}$)				
		Mean Flow		
		NCEP	NASCAR	NSIPP
Eddies	NCEP	3.24	3.60	3.33
	NASCAR	2.77	3.05	
	NSIPP	1.68		1.72
(b) 300 hPa barotropic conversions ($10^{-5} m^3 \cdot s^{-3}$)				
		Mean Flow		
		NCEP	NASCAR	NSIPP
Eddies	NCEP	-0.89	-1.93	-0.10
	NASCAR	-12.41	-12.54	
	NSIPP	-5.559		-4.62

Table 7: As in Table 6 except for Atlantic anticyclonic cases.

the seasonal migration of the climatological storm tracks. Our primary goals in this effort are to (a) identify synoptic and dynamic differences among the three stages and (b) test the extent to which the model behavior mimics observations.

Figure 24 displays Day -1 composite analyses of the 300 hPa and 700 hPa height anomalies for the early, middle, and late stages for observed PACCYC events. The most apparent difference between the stages is the magnitude of the growing cyclonic anomaly. During the midwinter, the primary cyclonic height anomaly at 300 hPa is about $-90 m$, while the magnitudes for the early and late stages exceed $-120 m$ (a similar disparity is observed at 700 hPa). This indicates that midwinter cyclones enter their strong growing stage somewhat deficient in magnitude. (On the other hand, the upstream and downstream anticyclonic feature is actually strongest during midwinter.) Comparing the early and late stages, the primary cyclonic feature in the early stage is deeper and more isotropic at both levels than that of the late stage. In each stage, the vertical tilt of the growing cyclone has a notable southwestward component, which is relatively enhanced in the middle and late stages. In addition to the southwestward tilt with height, the *horizontal* anomaly structure during midwinter features a bowing structure that rotates with respect to height. At 700 hPa there is a NW-SE anomaly tilt while at 300 hPa the eddy is oriented N-S. We note that the horizontal wave train pattern is more zonally oriented during the early and late stages than

the middle stage.

Figure 25 displays corresponding seasonally stratified composite 300 *hPa* and 700 *hPa* height anomalies for the NASCAR model. During the early and late stages, the core points in the NASCAR model are displaced north of the observed Pacific storm track. Consequently, the north-south seasonal migration of the climatological Pacific storm track is anomalously large in the NASCAR model. (This can be verified by comparing the location of the downstream anticyclonic features in Figs. 24 and 25.) During all three stages, the growing cyclone in the NASCAR model exhibits a westward tilt with height (with a slight southward component in the early stage). At both levels the major axis of the cyclonic flow anomaly is oriented NE-SW in the early stage, more N-S during midwinter, and NW-SE during the late stage. Similar to observations, the relative magnitude of the growing cyclonic anomaly is smallest during the middle stage at both levels. However, the downstream anticyclonic feature is also weakest during the middle stage in the NASCAR model, while the growing cyclonic feature is largest in magnitude during the late stage. The upper-level horizontal wave train pattern is more zonal during the early and late stages than it is during the middle stage (slight arcing toward the SE).

Figure 26 displays corresponding stratified composite 300 and 700 *hPa* height anomalies for the NSIPP model. From the middle to late stage, the core point in the NSIPP model shifts westward by 10°, while there is only a 5° westward shift in the observed core point. (No such zonal shift occurs in the NASCAR model.) The vertical tilt of growing cyclones in the NSIPP model has a notable southwestward component, especially during the middle and late stages. In the upper troposphere there is a greater NE-SW tilt in the cyclonic feature during the early stage relative to observations, and this relatively greater tilt prevails during the midwinter as well. The horizontal wave train feature in the NSIPP model bends towards the SE during the early stage, becomes more zonal in midwinter, and is slightly oriented from SW-NE during the late stage. For the middle stage, the 300 *hPa* cyclonic anomaly extends much farther south than in the observed cases (likewise for the upstream anticyclonic feature), yet we note that the growing cyclone at 300 *hPa* during the middle stage is weaker in magnitude than during the early and late stages. However, the

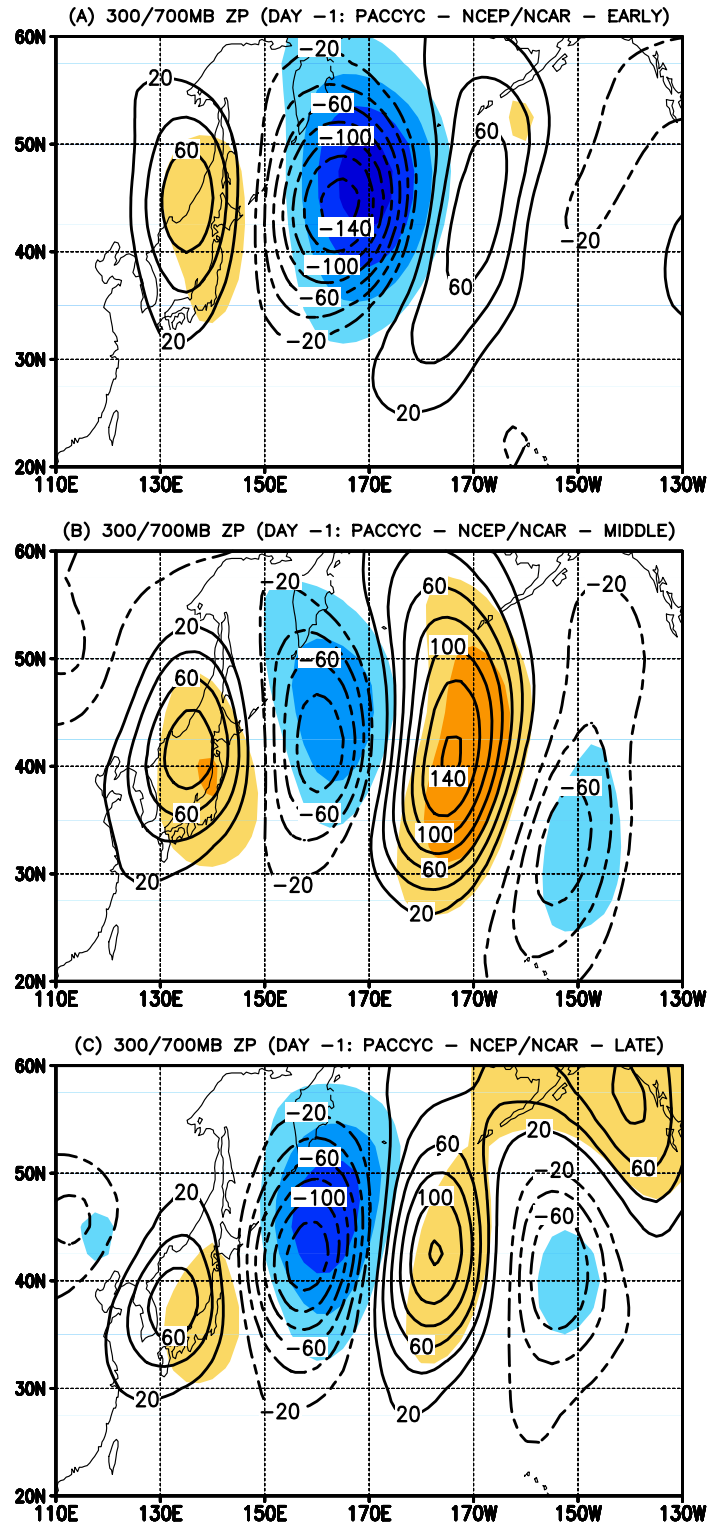


Figure 24: Composite height anomalies at 300 hPa (contour intervals: 20 m) and 700 hPa [orange (blue) shaded regions greater (less) than 20 m (–20) at 20 m intervals] for Pacific cyclonic cases at Day –1 for the NCEP-NCAR reanalyses during the (a) early, (b) middle, and (c) late stage of the northern Pacific cool season. The early stage is taken to be November and December, midwinter is taken to be January and February, and late stage is taken to be March and April.

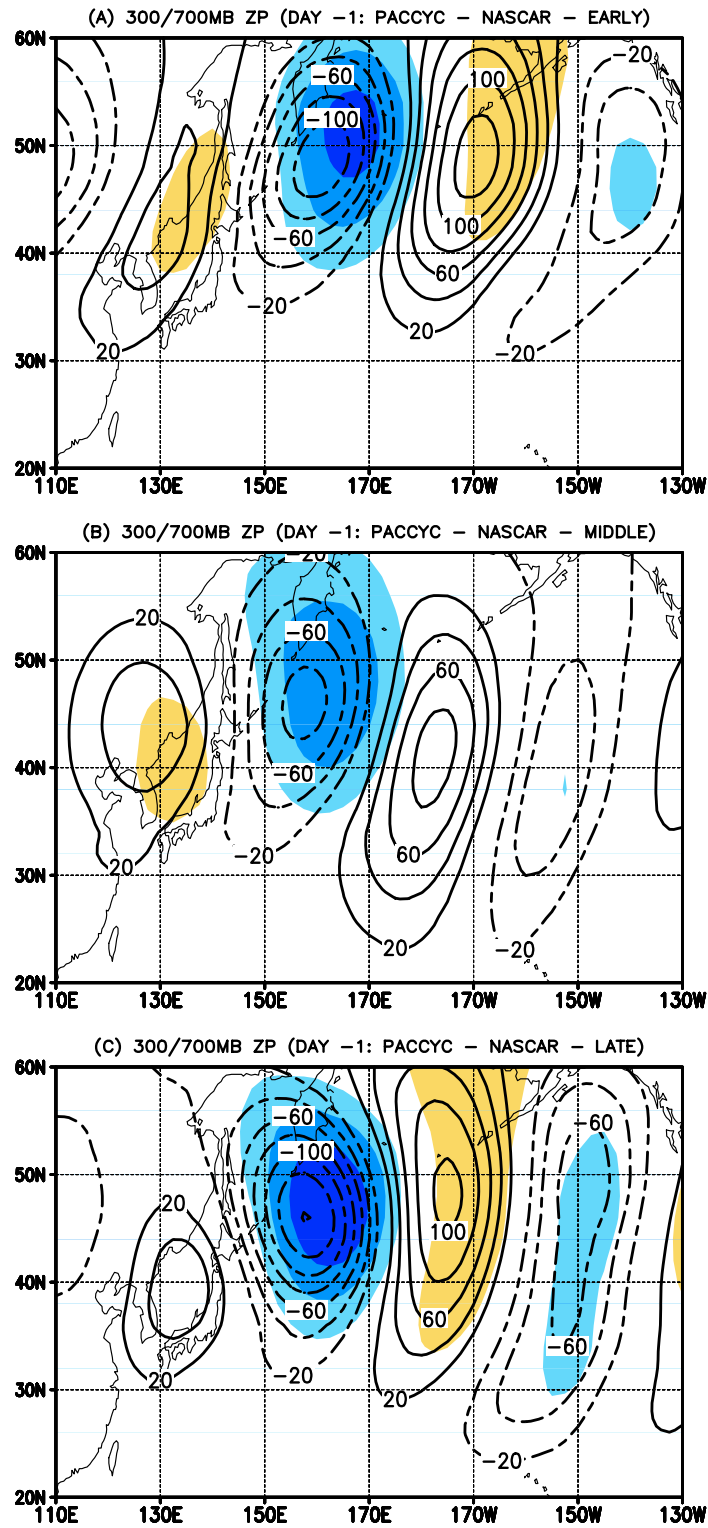


Figure 25: As in Figure 24 except for the NASCAR model.

corresponding cyclonic features at 700 *hPa* are similar in magnitude during the middle and late stages, and the downstream anticyclonic feature is weakest during the late stage.

One common element of the above analyses is the relative weakness of midwinter growing cyclones as they enter the period of strongest baroclinic growth. One factor proposed by Nakamura (1992) to explain the decreased baroclinic wave activity in the Pacific storm track in association with the midwinter suppression phenomena is a concomitant weakening in the upstream source of short waves (the "seeds" for downstream baroclinic development). Hakim (2003) recently demonstrated that Pacific baroclinic wave packets originate upstream poleward of the Himalayas. Following the idea of Nakamura (1992), we posit that the midwinter suppression could be partly related to a relative lack of upstream short-wave activity emanating from over Siberia, where high static stability prevails during midwinter.

To test this idea directly we next analyze the regional difference in 300 *hPa* synoptic eddy activity between the midwinter period and an average of the early and late periods. This difference is shown in Figure 27 along with contours of the winter-mean rms in the 300 *hPa* height field for all three datasets considered. Consistent with the profiles of EKE (Figure 19), the magnitude of the simulated winter-averaged storm tracks over the North Atlantic correspond much more closely to observations than the Pacific storm track. For the NASCAR model, the magnitude of the Pacific climatological storm track is slightly weaker, whereas the Atlantic storm track compares very well with observations. Both storm tracks in the NSIPP model are much weaker than the observed winter-mean storm tracks (also see Fig. 3). As one would expect from the analyses of 3.2.2 (Figure 7), there are prominent reductions in synoptic eddy activity observed over and north of the winter-averaged storm track during midwinter. Interestingly, this anomalous weakening pattern is observed to extend upstream into Siberia, precisely the region from which the upstream short waves emanate.

As mentioned earlier, one of the interesting things found in 3.2.2 (Figure 7) was that the NSIPP model not only produces a midwinter suppression of the North Pacific storm track but also a midwinter suppression of the North Atlantic storm track (which is weaker and

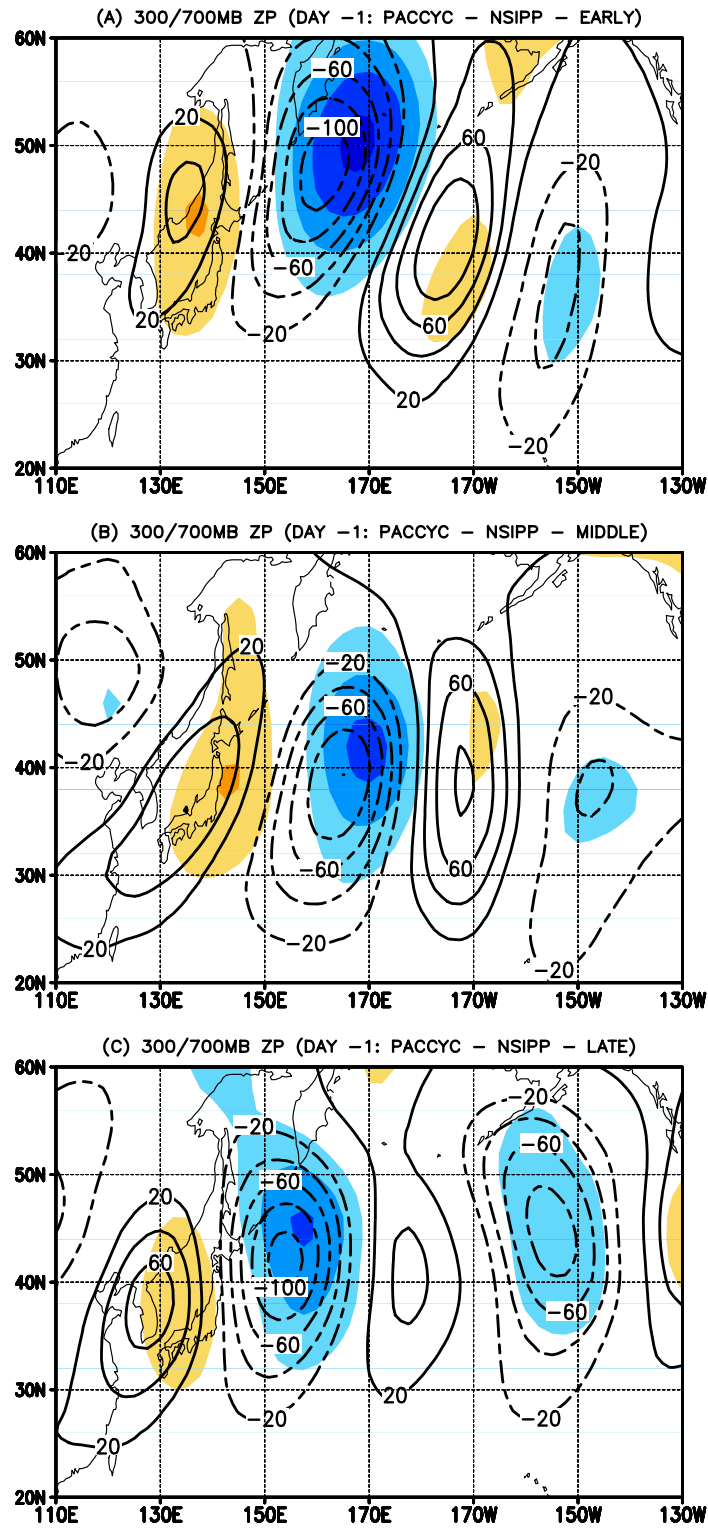


Figure 26: As in Figure 24 except for the NSIPP model.

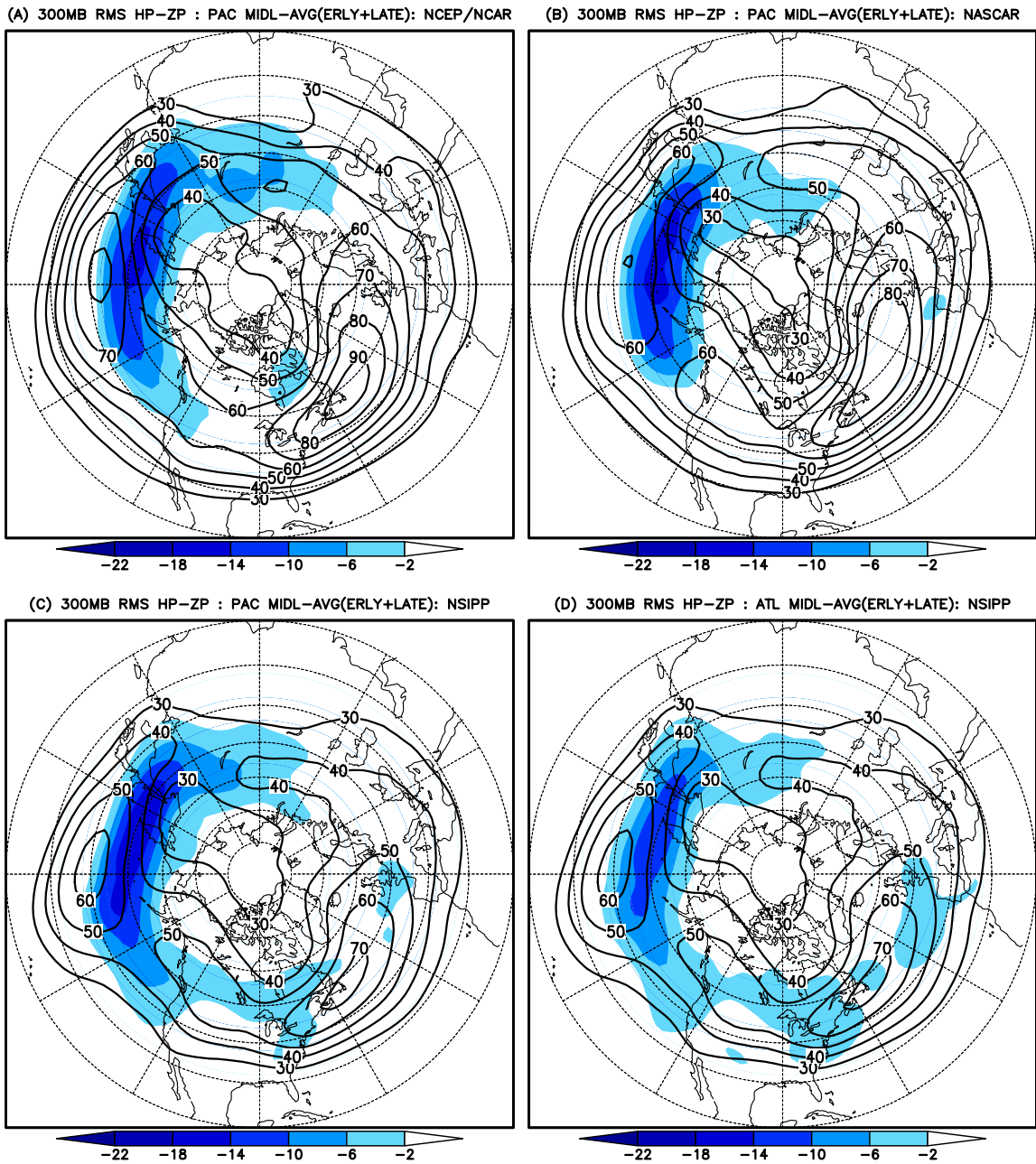


Figure 27: The rms highpass-filtered geopotential height anomalies for the winter average (contour intervals: 10 *m*) and the difference between the midwinter period and an average of the early and late periods (blue shaded regions: units *m*) at 300 *hPa* during the Pacific cool season for the (a) NCEP-NCAR reanalyses, (b) NASCAR dataset, (c) NSIPP dataset, and (d) during the Atlantic cool season for the NSIPP model. The early stage of the Atlantic cool season is taken as December through 15–January, midwinter 16–January through Feb., and late stage March through 15–April.

confined between 15–January through February). As such, one might wonder whether the idea put forth above for the Pacific storm track has any relevance for NSIPP’s North Atlantic storm track. Interestingly, Figure 27d provides evidence that this may be indeed the case as the NSIPP difference pattern includes an organized area of suppressed synoptic eddy activity located over eastern North America, which is a regional source of synoptic wave activity for the North Atlantic storm track. Similar patterns are not observed for NCEP or NASCAR. The current results provide circumstantial evidence that the midwinter suppression phenomenon may be linked to midwinter weaknesses in the upstream formation of upper-level short waves, leading to anomalously weak “seeding” for baroclinic growth in the downstream storm track of interest.

4.4 Summary

Winter-averaged results indicate that the model-simulated events are generally too weak in amplitude, particularly in the upper troposphere. For the North Pacific storm track, model-simulated events are also anomalously distended in the meridional direction. The existing model biases in eddy structure and magnitude lead to anomalously weak baroclinic energy conversions for both cyclonic and anticyclonic events over the North Pacific. For the North Atlantic storm track, the NASCAR model provides a very good representation of the structure of developing cyclonic events. However, growing North Atlantic cyclones in the NSIPP model are anomalously weak and horizontally too isotropic (meridionally retracted). These latter two characteristics are also observed in both models for developing anticyclonic flow anomalies over the North Atlantic. The relative weakness of NSIPP synoptic events over the North Atlantic region is largely responsible for the 50% deficiency in areally-averaged baroclinic energy conversions. Conversely, the NASCAR model climatology features anomalously strong temperature gradients over the western North Atlantic that provide local enhancements to the baroclinic energy conversion field.

A seasonally stratified diagnostic analysis reveals that the simulated climatological storm tracks over the North Pacific undergo larger spatial migrations during the cool season compared to observations. It is further determined that the suppression of synoptic eddy

activity in the Pacific storm track is associated with a relative midwinter weakness in the *magnitude* of the growing cyclonic anomalies. Specifically during midwinter, the cyclonic perturbations entering the Pacific storm track are deficient in magnitude compared to their early and late winter counterparts. It is also discovered that the midwinter suppression pattern over the North Pacific region has a clear organized extension upstream into Siberia, the region from which incipient upper-tropospheric short-wave features emanate. This behavior is found in both observations and model simulations. These results support the idea that the North Pacific midwinter suppression phenomenon is linked to a midwinter weakness in the upstream formation of upper-level short waves, leading to anomalously weak "seeding" of baroclinic disturbances in the Pacific storm track.

CHAPTER V

DIAGNOSES OF THE NORTH PACIFIC MIDWINTER SUPPRESSION

The previous chapter provided initial evidence consistent with the seeding hypothesis originally proposed in Nakamura (1992). Specifically, the structure of maturing North Pacific cyclones was studied and it was found that midwinter cyclones enter their period of maximum growth weaker in magnitude than analogous events occurring during early or late winter. In this chapter, we present an observational study of the upstream origin of the midwinter suppression of North Pacific storm track. The evolution of wave packets traversing Asia prior to strong cyclogenesis in the Pacific storm track is analyzed. Our procedure isolates the variations in upstream wave behavior associated with the different stages of the cool season.

5.1 Methodology

In this section, we expand from the AMIP-II time period and use 45 years of daily-averaged data from September 1958 through August 2002. We first define a daily climatology as the sum of the first 6 Fourier harmonics of a seasonal cycle derived from the calendar time-series of long-term daily averages. Daily intraseasonal anomalies are then computed by systematically subtracting both the daily climatology and interannual variability (seasonal anomalies) from unfiltered daily averages. As before, high-pass (synoptic scale) and low-pass components of the intraseasonal anomaly field are determined using 151-point Lanczos filters. Synoptic scale (low frequency) variability is defined as eddies having periods of 2.5–6 (10–90) days. The total (unfiltered) intraseasonal anomaly field is the sum of all time scales less than 90 days.

The Pacific midwinter suppression phenomenon is illustrated in Figure 28 by plotting the climatological annual cycle of baroclinic forcing and baroclinic wave activity averaged

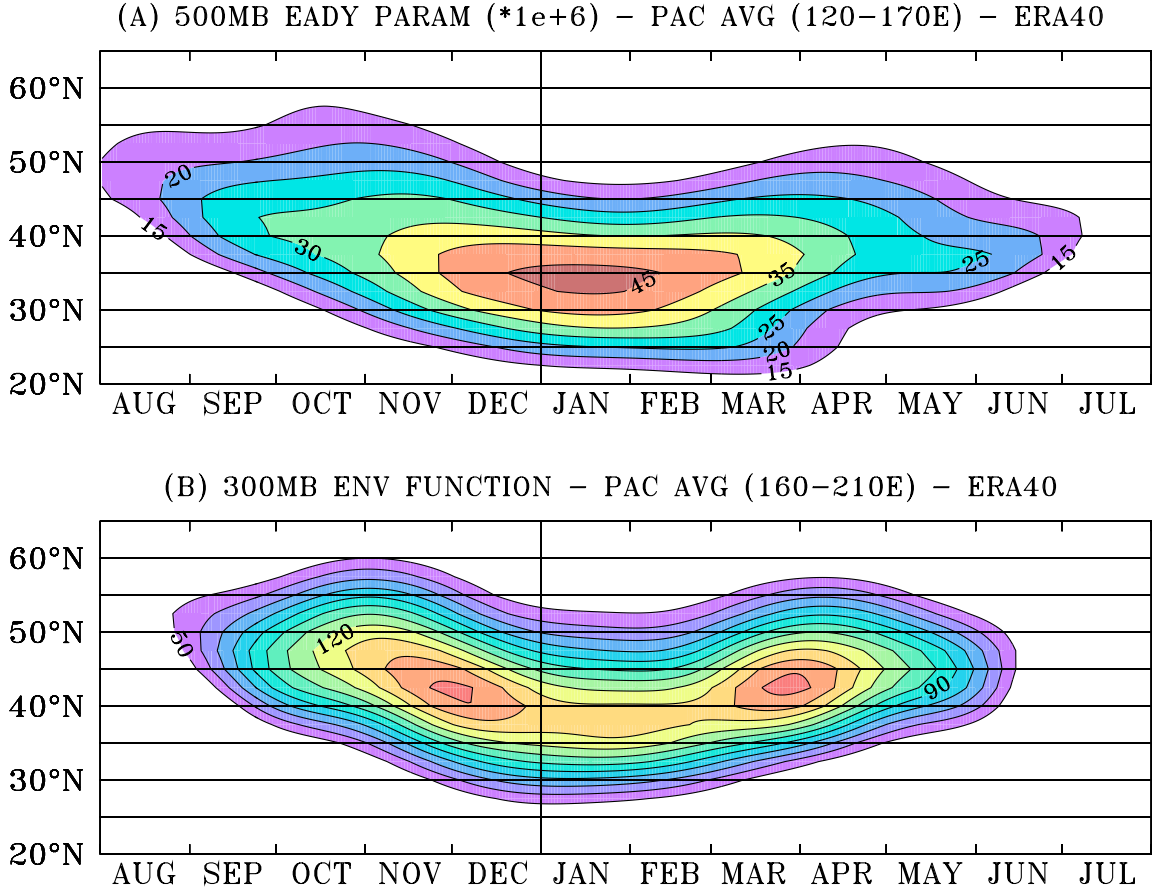


Figure 28: The annual cycle of the climatological-average of (a) the 500 *hPa* Eady parameter longitudinally averaged across the baroclinic region of the Pacific storm track and (b) the 300 *hPa* envelope function longitudinally averaged across the zonal extent of the North Pacific storm track. A vertical axis marking 1–January is plotted.

over the Pacific storm track. The baroclinic forcing is measured by the Eady parameter.

$$\Gamma = \frac{f}{N} \cdot \frac{d\bar{U}}{dz}, \quad (3)$$

where f is the Coriolis parameter, N is the static stability, and \bar{U} is the zonal wind climatology. Figure 28a shows that the average baroclinicity over the North Pacific is largest during midwinter (when the upper tropospheric jets are strongest). Baroclinic wave activity is measured using the envelope function of Nakamura & Wallace (1990). Interestingly, the Pacific storm track (Figure 28b), is strongest during (a) late autumn/early winter and (b) late winter/early spring with a relative minimum observed during midwinter, when baroclinic forcing is greatest.

To study seasonal variations in the behavior of upstream wave packets that seed the Pacific storm track, we first stratify the boreal cool season into three stages: an early stage taken as November and December, a middle stage taken as January and February, and a late stage of March and April. As shown in Figure 28 the early and late (middle) stages correspond to the maxima (relative minimum) in synoptic eddy activity over the North Pacific. Taking into account the seasonal migration of the storm track, we next select a geographical "core" point marking the local relative maximum in wave activity for each stage. To focus on strong cyclonic events, we normalize the time-series at the core point for each stage and perform regressions for times marking relative minima in the time-series that exceed -1σ . The regression approach follows Equation 1. We will plot maps of regression coefficients for different lags in order to illustrate the structure and evolution of baroclinic waves prior to strong cyclogenesis. This provides about 300 separate events for each stage over the 45 year period. Due to the marked symmetry of the early and late stages, we combine the results of these stages into one (early/late winter) and contrast them with that of the middle stage.

As noted in the 1.2.1, downstream development is responsible for the coherence of baroclinic wave packets and their propagation away from the regional baroclinic zones. The energy within a wave packet has an eastward velocity slightly larger than the time-mean flow, which is transferred between consecutive disturbances in the form of an eastward ageostrophic geopotential flux (Orlanski & Katzfey, 1991). Following the methods of (Orlanski & Katzfey, 1991), we compute the ageostrophic flux vectors to illustrate the downstream dispersion of eddy kinetic energy within a Rossby wave packet (relative to the background mean flow).

5.2 Lag regression analyses

The regression results for the total (unfiltered) intraseasonal (Figs. 29–31) and the low-pass filtered (Figs. 32–34) anomaly field at Day -3 , -5 , and -7 for the average of the early and late stages (EL: top figure) and the midwinter stage (MW: bottom figure), respectively. Day 0 is defined when the upper level cyclone is mature within the core of the climatological storm

track (175°E). Contours are the regressed geopotential height anomalies at 300 *hPa*, while the shaded regions indicate statistical significance at the 95% level based on a two-tailed t-test. The associated ageostrophic geopotential flux vectors are also plotted with a scale vector provided.

The upper tropospheric cyclonic disturbance, which ultimately initiates cyclogenesis, enters the baroclinic zone of the Pacific storm track at Day -3 (Fig. 31). The associated negative height anomaly is located over the Sea of Japan (135°E) at this time. It is evident that this "seed" for subsequent cyclogenesis is weaker in amplitude (by 20 *m*) during MW (Fig. 31d) than EL (Fig. 31a), consistent with the composite results presented in 4.3. Furthermore, it is interesting to note that the upstream anticyclone (110°E) and cyclone (90°E) are relatively larger in magnitude with greater downstream-oriented ageostrophic fluxes during MW. The remaining discussion is focused on examining why this precursor perturbation is weaker during midwinter.

The upstream time evolution during EL consists of the southeastward propagation (in both phase and energy) of a coherent packet of synoptic scale waves from Siberia toward the east coast of Asia. The phase of the precursor cyclonic disturbance can be traced back to west of Lake Baikal at Day -7 (Fig. 29a). This disturbance strengthens via downstream energy dispersion as it propagates southeastward within the wave packet. In accord with Rossby wave theory, the energy of the wave packet moves downstream more quickly than the individual troughs and ridges. There is little or no projection of this wave pattern upon the low-frequency time scales (Fig. 32a). The evolution observed during the early and late stages corresponds very well to the behavior of synoptic wave packets propagating along the northern branch of the Asian wave guide as in Chang (2005). However, the southern branch does not play a significant role in the strong cyclogenesis events identified in our analysis.

The upstream behavior observed during MW is markedly different than EL. First, there is no evidence of a coherent synoptic scale wave packet upstream at Day -7 (Fig. 29b). However, a significant large scale cyclone feature extends over much of central Siberia at Day -7. As illustrated in Figure 32b, this cyclone feature is mainly a low frequency

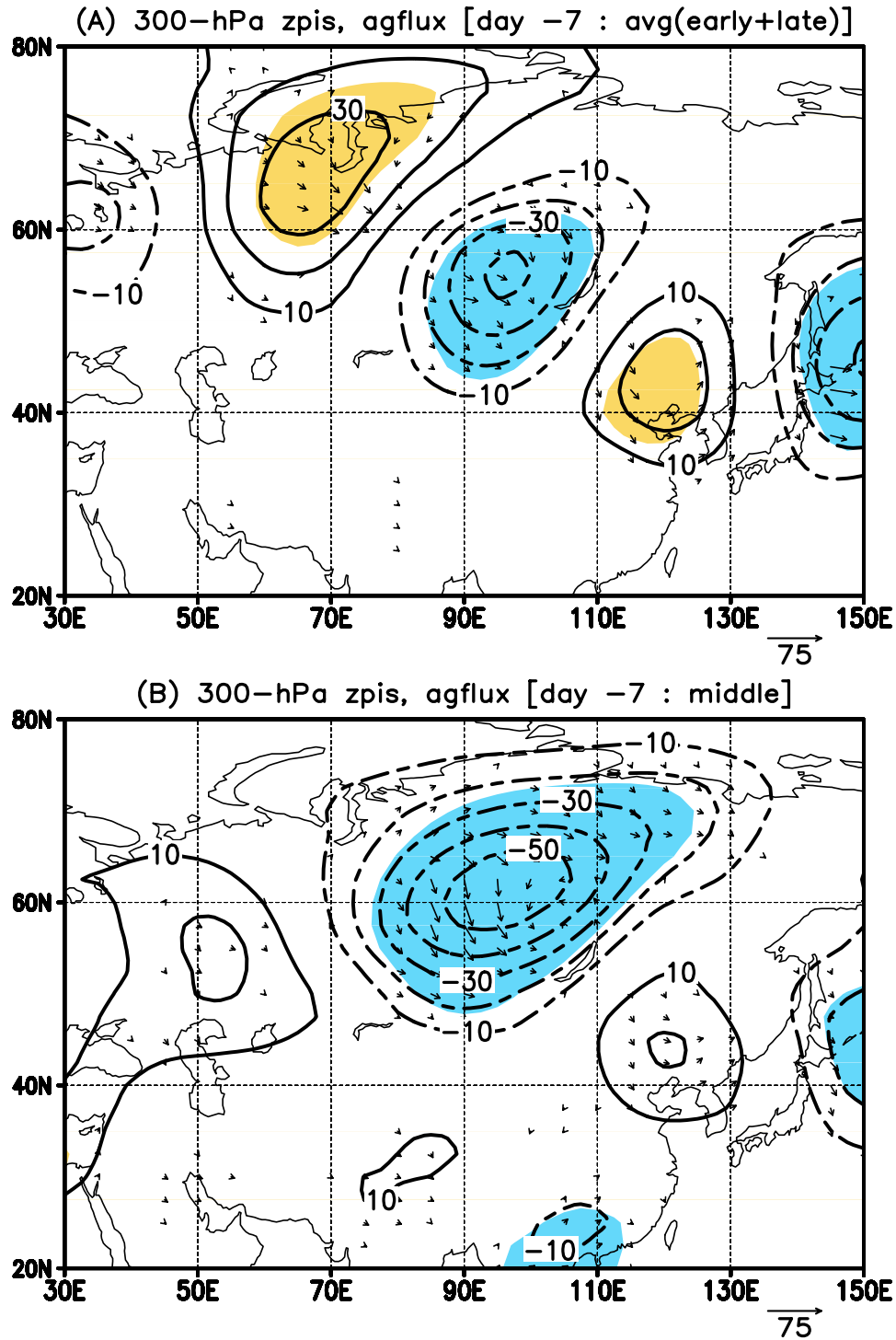


Figure 29: Regressed intraseasonal height anomalies (contour intervals: 20 m) at 300 hPa for Day -7 for (a) the average of the early and late stages and (b) the middle stage of the North Pacific cool season. Positive (negative) height anomalies significant at the 95% confidence level are shaded in orange (blue), which is based on a two-tailed Student's *t*-test derived from 300 cyclonic events for *each* stage). The ageostrophic flux vectors are plotted and a scale vector provided.

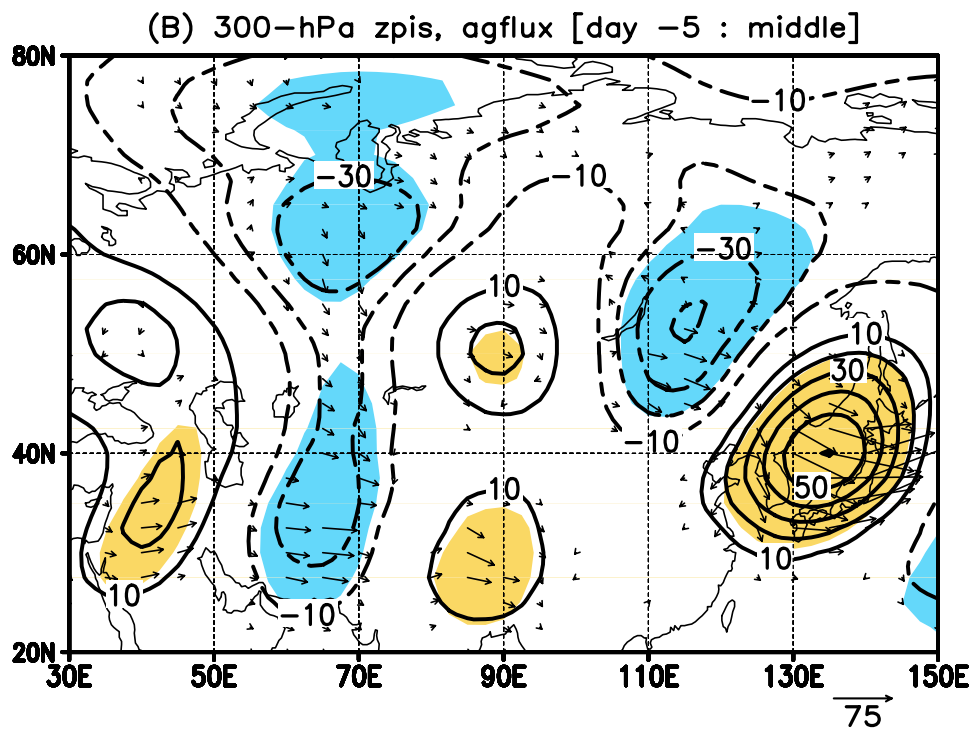
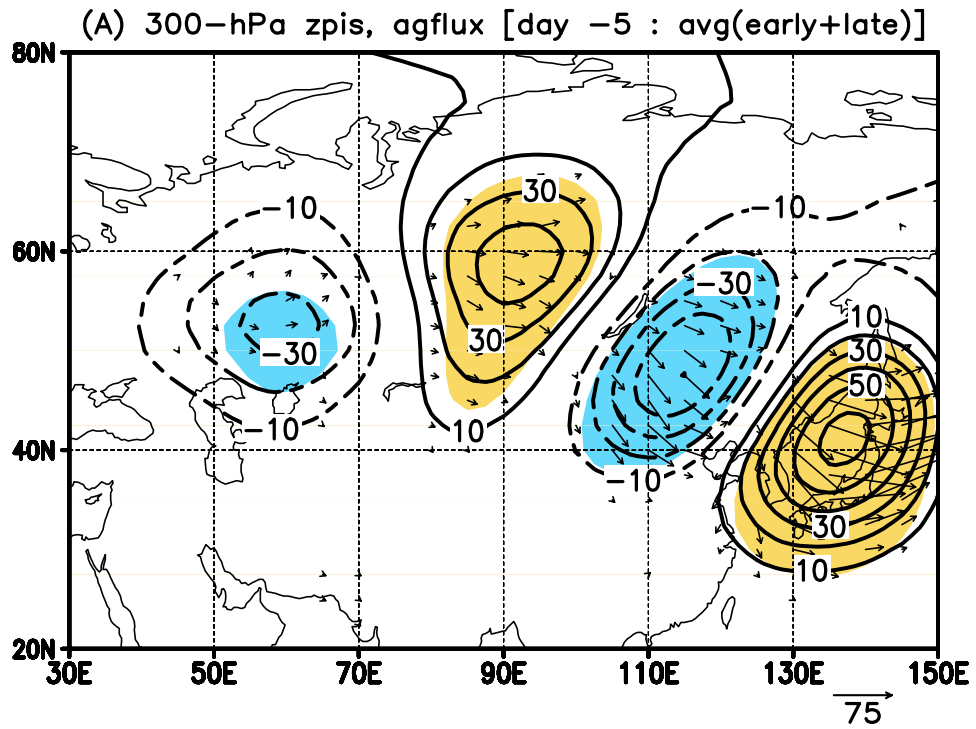


Figure 30: As in Figure 29 except for Day -5.

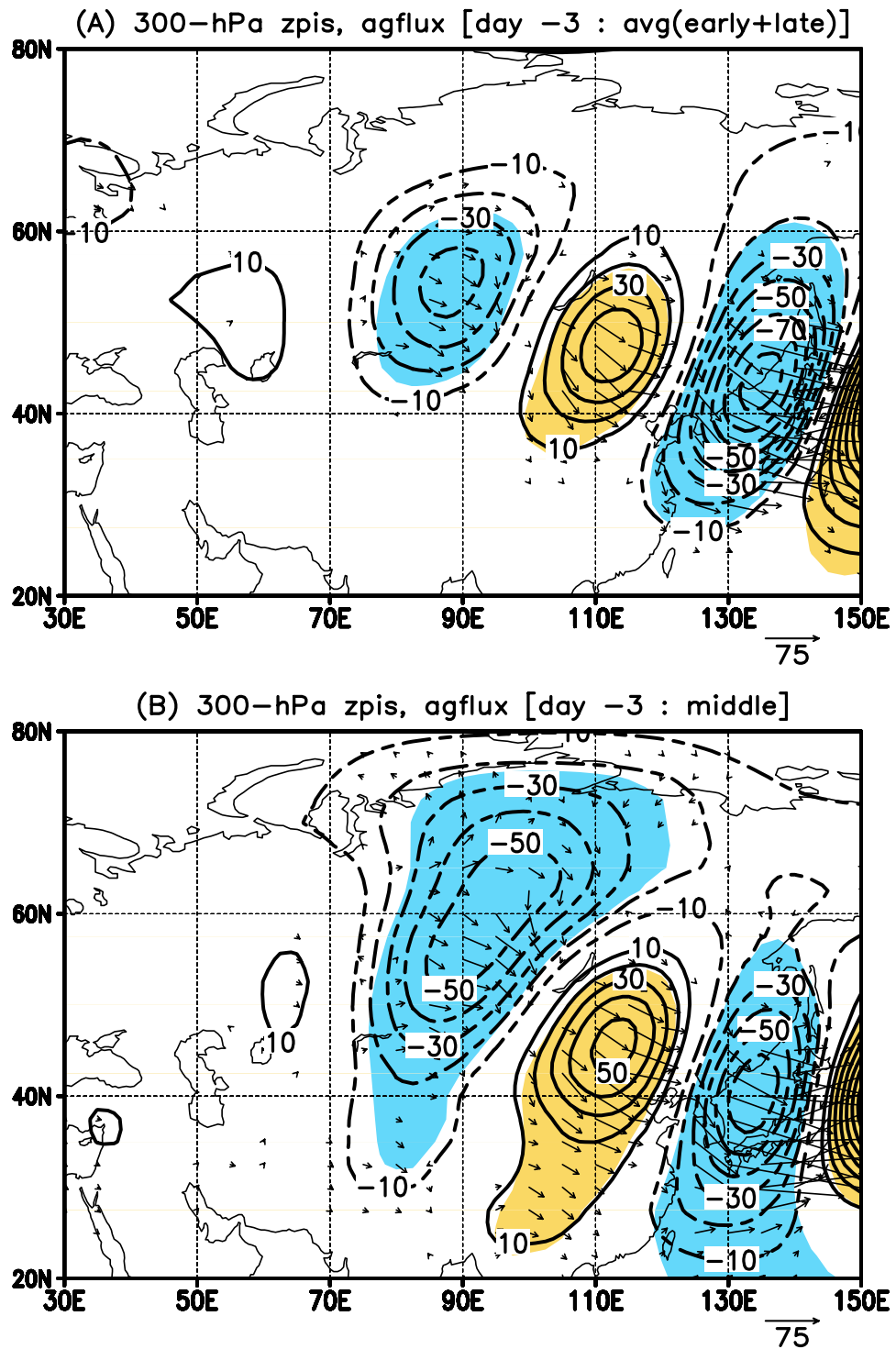


Figure 31: As in Figure 29 except for Day -3. The cyclone positioned at 130°E propagates to the core point of the Pacific storm track by Day 0.

anomaly. This low frequency cyclone gradually weakens and moves eastward after Day -7 (see Figs. 33b and 34b).

Significant synoptic-scale wave packets emerge along both the north and southern branches of the Asian waveguide at Day -5 (Fig. 30b). The two wave packets are longitudinally in phase with one another, favoring strong subsequent cyclogenesis downstream over the Pacific (Chang, 2005). The low frequency anomaly over Siberia is less evident at this time since it is out of phase with a ridge embedded within the northern synoptic wave packet. By Day -3 (Fig. 31b), all three features have come into phase with one another resulting in a robust Rossby wave packet over eastern Asia. Within this packet, the cyclonic circulation anomaly over the Sea of Japan is strengthening due to downstream development. Nonetheless, this seed for subsequent oceanic cyclogenesis remains weaker than its early-late stage counterpart.

We have shown that events during EL stages arise in rather simple fashion from synoptic wave packets propagating along the northern branch of the Asian waveguide. We also recognize that for MW cases the synoptic eddy precursors observed along the northern branch at Days -7 and -5 are less robust. To explore this behavior further we contrast the RMS-filtered (synoptic) 300 *hPa* geopotential heights during MW and EL by subtracting the latter from the former. This is displayed (shading) along with the winter-mean RMS high-pass height field (contours) in Figure 35. The western edge of the Pacific storm track (120–150°E) is distinguished by the midwinter suppression of synoptic eddy activity on its north side. This is simply the western portion of the well known Pacific midwinter suppression pattern (see Fig. 27a). However, in addition to this feature we observe a secondary suppression of synoptic wave activity located upstream over central Siberia. This is precisely the region from which synoptic scale wave packets emanate prior to EL cyclogenesis events. Thus, during MW we find a prominent general weakening in the amplitude of synoptic scale wave activity within a critical source region for the upper tropospheric seeding of Pacific cyclogenesis. Preceding strong cyclogenesis events during MW, synoptic wave packets along the northern branch of the Asian waveguide juxtapose with (a) a wave packet propagating along the southern branch of the Asian waveguide

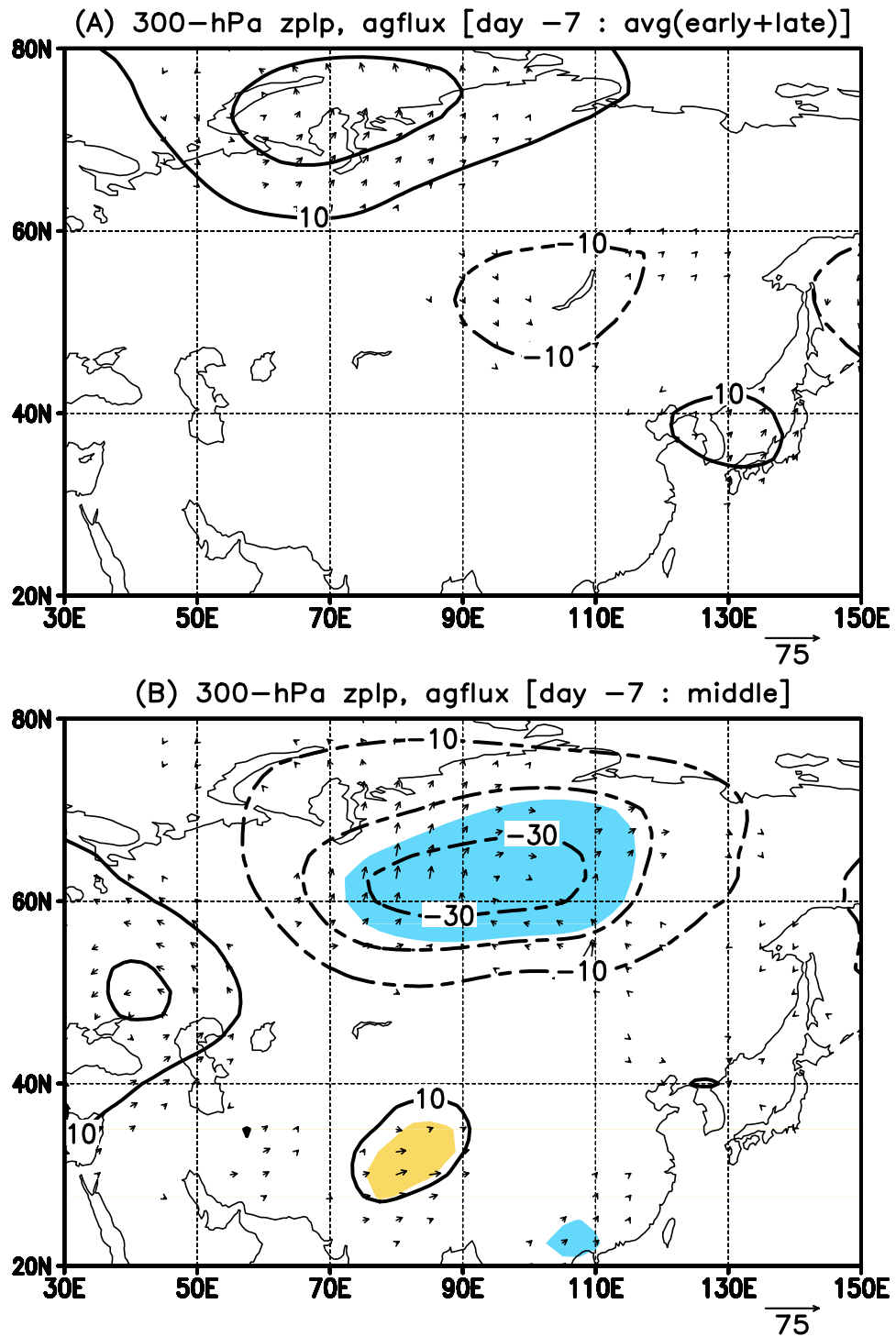


Figure 32: As in Figure 29 except for regressed lowpass height anomalies at Day -7.

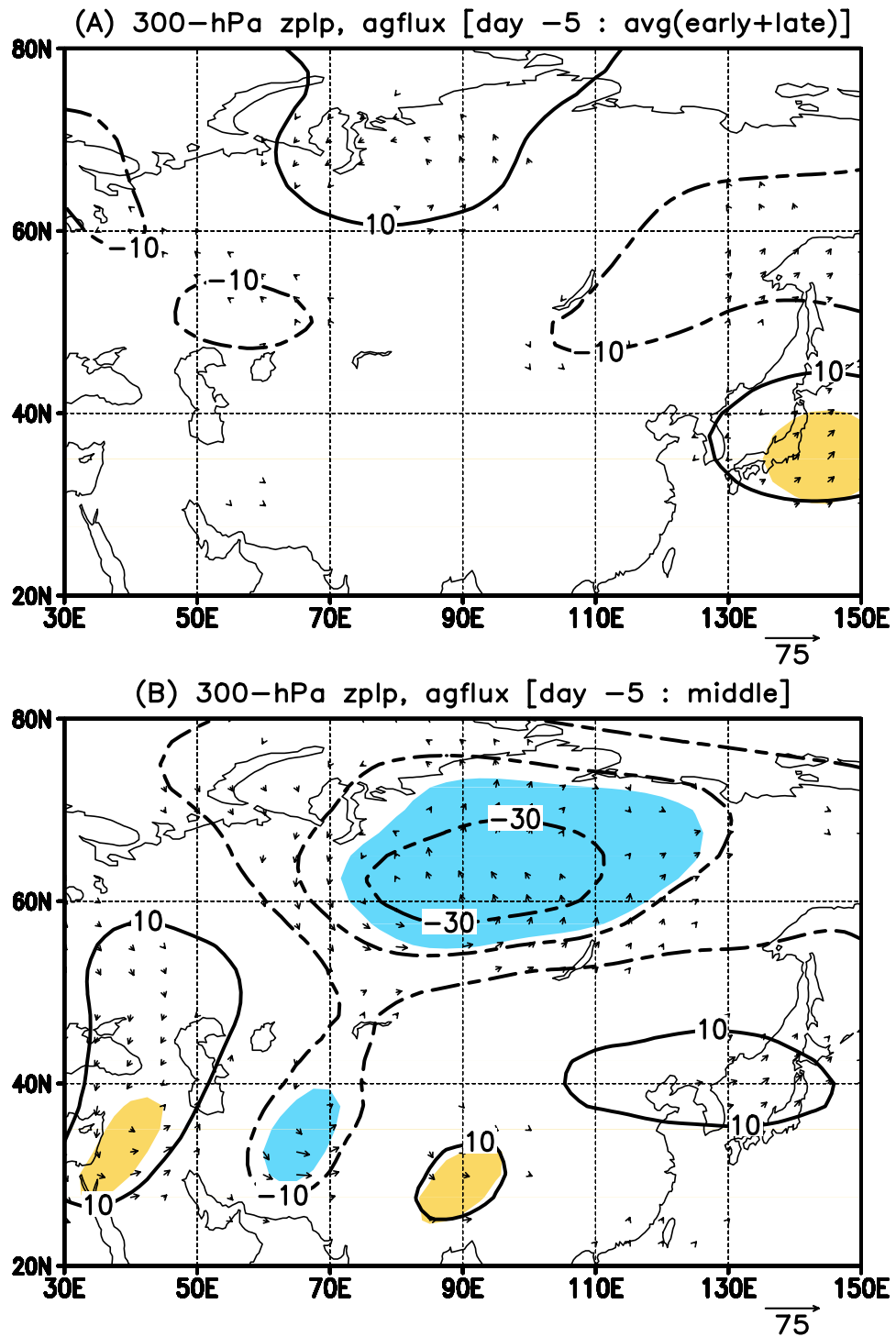


Figure 33: As in Figure 29 except for regressed lowpass height anomalies at Day -5.

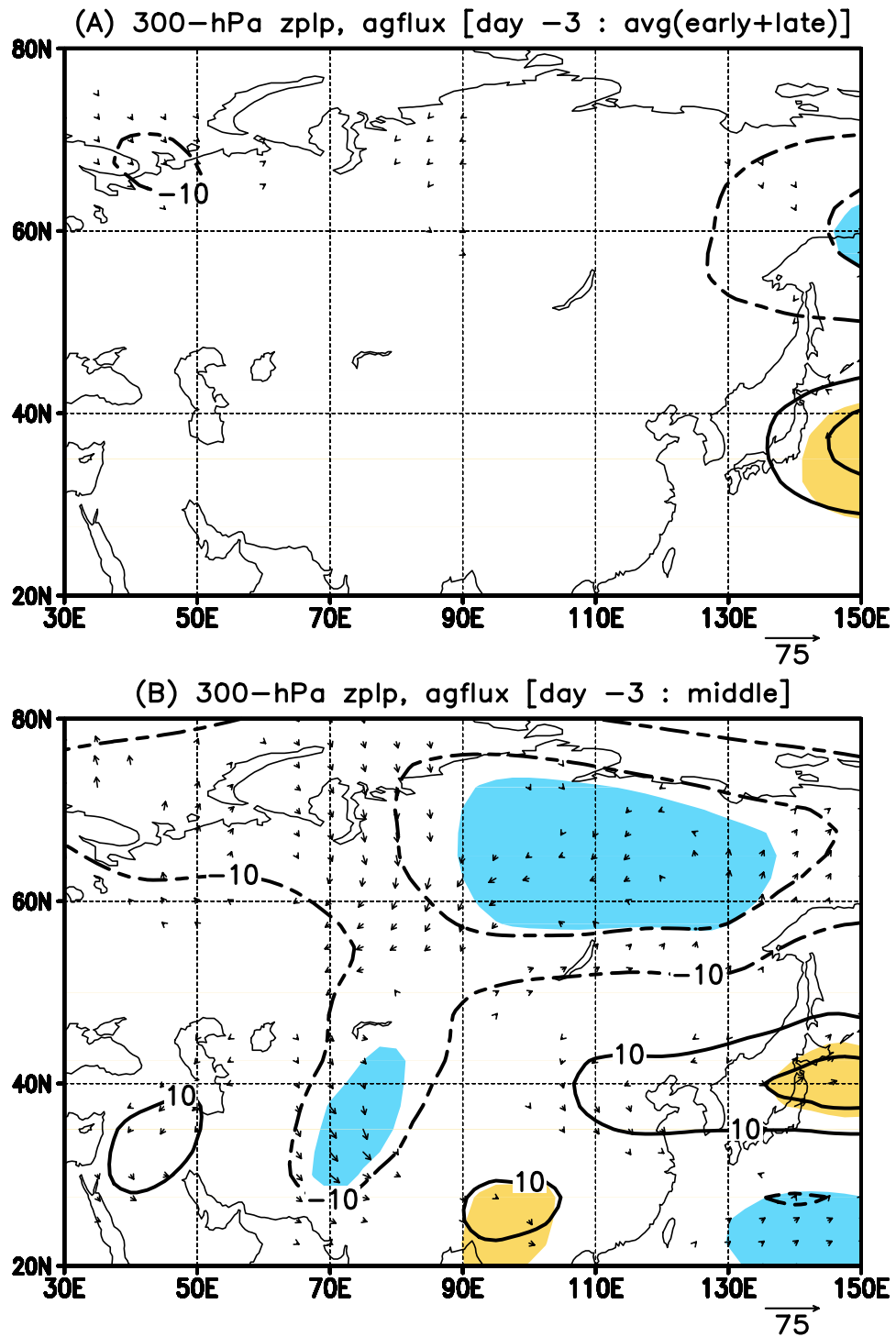


Figure 34: As in Figure 29 except for regressed lowpass height anomalies at Day -3.

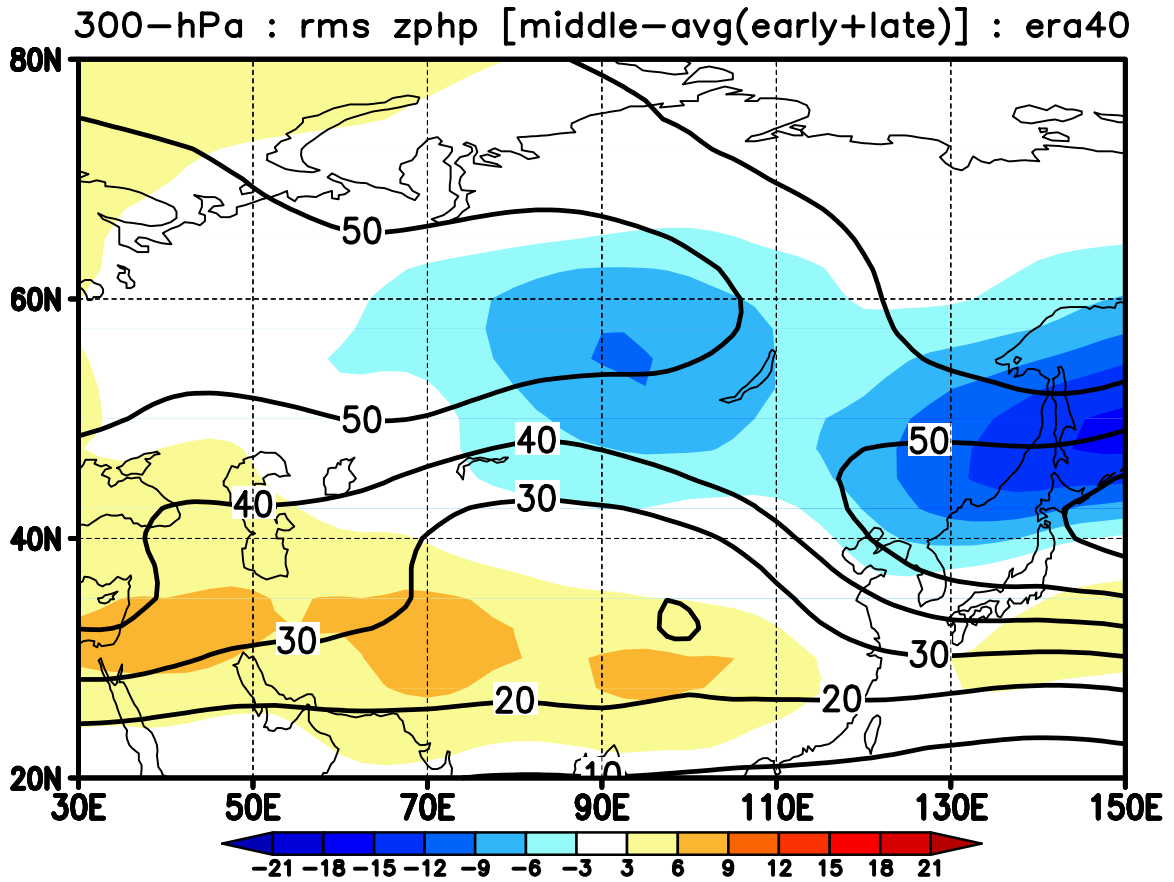


Figure 35: The rms highpass-filtered geopotential height anomalies for the DJF average (contour intervals: 10 *m*) and the difference between the middle period and an average of the early and late periods (color shaded regions: units *m*) at 300 *hPa*. Shaded regions less than zero signify a decrease in the standard deviation of high-frequency eddies during midwinter.

and/or (b) pre-existing low frequency anomaly over Siberia. Interestingly, the latter feature emerges from along the northern branch of the Asian waveguide, in the same general region characterized by a midwinter weakening of synoptic wave activity (compare Figs. 32b and 35). Thus within this region low frequency wave appear to “pick up the slack” in helping to promote downstream cyclogenesis during midwinter. However, these supplementary contributions are insufficient to overcome the midwinter suppression.

5.3 *Statistical analyses*

5.3.1 Monte Carlo testing

Our regression results show a significant linear relationship between the strength of mid-winter cyclones in the Pacific storm track and that of a low-frequency cyclone over Siberia up to 7 days preceding the event. However, significance from a regression does not necessarily imply a significance in the atmosphere. For example, a study by Chen (1981) illustrated that regression a randomly generated time series onto the 700 *hPa* height field produced more significant features than regression the Southern Oscillation Index at various lags. Consequently, one must take into account the degrees of freedom associated with the spatial variability in the atmosphere, which can be determined by employing a Monte Carlo technique discussed in Livezey & Chen (1983).

We define Day 0 when a cyclone in the core of the Pacific storm track attains a peak magnitude exceeding -1σ . For each stage of the cool season, the magnitudes of the mature cyclonic events are regressed onto field variables for negative lags relative to Day 0. To assess the "significance" of the significant regions in the regressions (chosen to be 95% based upon two-tailed t-test), we use a random number generator to define a new array of Day 0's. The magnitudes of the cyclonic events are now regressed onto field variables for negative lags relative to the random array of Day 0's. After each "random" regression, the area coverage of significance is computed. This technique is repeated 1000 times in order to create a distribution of area coverages. A true significance of the regression is assessed by comparing the areal coverage of significance from the "selected" regression to that derived from the random regressions. For this study, we focus on Asia, specifically the region depicted in Figs. 29–35.

As an example, the magnitude of MW cyclonic events are regressed onto the unfiltered geopotential height anomaly field for random days and for days that precede the event by one week. (These unfiltered anomalies exclude interannual variability.) Derived from the random regressions, selected percentiles of the area coverage of significance are listed in Table 8 along with the significant coverage and its associated percentile from the selected

Midwinter : Unfiltered height anomalies : Day -7			
Random Days		Selected Days	
Area coverage (m^2)	Percentile	Area coverage (m^2)	Percentile
52.55	70 th	59.91	76 th
59.18	75 th		
65.41	80 th		
73.94	85 th		
83.82	90 th		
103.40	95 th		
140.57	99 th		

Table 8: The left column lists selected percentiles of the area coverage (units: m^2) of significance derived from 1000 random cases. For each random case, the magnitude of mature cyclonic events in the Pacific storm track core during midwinter are regressed onto the unfiltered geopotential height anomaly field over Asia for randomly selected days. The right column lists the area coverage and associated percentile derived from regressing the events onto the unfiltered height field over Asia at 7 days preceding the event.

regression. Relative to using dates that precede MW cyclonic events by one week, regressing the magnitude of strong MW cyclones onto the height field over Asia for random result in larger regions of significance about 1 out of 4 times. In other words, the confidence that significant regions at Day -7 (as shown in Fig. 29) are associated with MW cyclonic events is about 75%.

This Monte Carlo method is applied to MW and EL for Days -7, -5, and -3 for the unfiltered, highpass-filtered, and lowpass-filtered geopotential height fields. The areal coverage and percentile of the selected regressions for each case are listed in Table 9. The significant regions for highpass-filtered height field are indeed significant up to one week preceding the events for EL and MW. However, significant regions from random regressions of the MW low-frequency height field over Asia is greater than that for selected days. Consequently even at a lag of 3 days, there is not much confidence when interpreting significant regions based solely from lag-regressions onto the lowpass-filtered height field.

5.3.2 Upstream Siberian indices

We propose that strong cyclogenesis events will likely preferentially occur during MW windows of opportunity when a cyclonic low frequency anomaly occurs over Siberia.

(a) Unfiltered height anomaly					
Early and Late Stages			Midwinter		
Day	Area coverage (m^2)	Percentile	Day	Area coverage (m^2)	Percentile
-7	87.83	90 th	-7	59.91	76 th
-5	189.80	99 th	-5	127.28	98 th
-3	168.15	98 th	-3	197.13	99 th

(b) Highpass-filtered height anomaly					
Early and Late Stages			Midwinter		
Day	Area coverage (m^2)	Percentile	Day	Area coverage (m^2)	Percentile
-7	261.37	99 th	-7	163.62	99 th
-5	337.95	99 th	-5	330.63	99 th
-3	363.31	99 th	-3	364.33	99 th

(c) Lowpass-filtered height anomaly					
Early and Late Stages			Midwinter		
Day	Area coverage (m^2)	Percentile	Day	Area coverage (m^2)	Percentile
-7	5.72	11 th	-7	17.22	27 th
-5	47.33	60 th	-5	31.02	47 th
-3	44.48	55 th	-3	32.07	48 th

Table 9: The area coverage and percentile of significant regions derived from a Monte Carlo technique during EL and MW at 7, 5, and 3 days preceding strong cyclonic events in the core of the storm track associated with regressions onto the (a) unfiltered, (b) highpass-filtered, and (c) lowpass-filtered geopotential height anomaly field over Asia.

However, the results of the Monte Carlo testing modifies the confidence of our conclusion based solely from the regression results. Therefore to further test our hypothesis, we create an index representing the mode of the Siberian anomaly of interest and conduct further statistical tests in order to determine how it relates to the level of baroclinic wave activity in the Pacific storm track. Two methods are used to produce a Siberian index: (i) projecting the Day -7 regressed low-frequency pattern (shown in Figure 32b) onto the geopotential height anomaly field and (ii) from conducting EOF analysis of geopotential height anomalies over Asia. The geopotential height anomalies used to create the indices are simply the raw field with the seasonal cycle removed, since the indices can be produced from the height field for a single day.

The first index is created by taking the regressed lowpass-filtered geopotential height patterns at Day -7 (Figure 32b) and projecting it onto the geopotential height anomaly field. This index represents the relative mode of the pattern in Figure 32b, where positive (negative) values of the index indicate a large-scale cyclone (anticyclone) over Siberia. This index is referred to as the "projected" Siberian (PS) index.

A second index is derived from an EOF analysis focusing on the region 20°N–80°N, 30°E–150°E (similar to the grid in Figs. 29–35). The EOFs of the daily-averaged unfiltered geopotential height anomaly at 300 *hPa* are computed for each stage of the cool season. Figure 36 illustrates the 300 *hPa* geopotential height anomalies regressed onto its first two EOFs for EL and MW. The percent variance explained by each EOF is listed in the figures. (EOFs 3–5 in EL and MW account for approximately similar variances of 7–9%, while the first two EOFs in each stage account for nearly one-third the total variance over Asia.) The first EOF in EL and MW (Figs. 36a,c) have similar patterns with the primary anomaly positioned in northwestern Russia near the coast of the Barents Sea. The pattern for the second EOF (Figs. 36b,d) is similar in EL and MW with the primary anomaly stretching across Siberia and centered around 100°E, similarly located to the midwinter low-frequency cyclone illustrated in Figs. 32b and 33b. The percent variance for EOF2 is largest during the middle stage. Thus, we compare the index for the second EOF (referred to as the E2 index) with the PS index and find that the two indices have a correlation of +0.746 (the

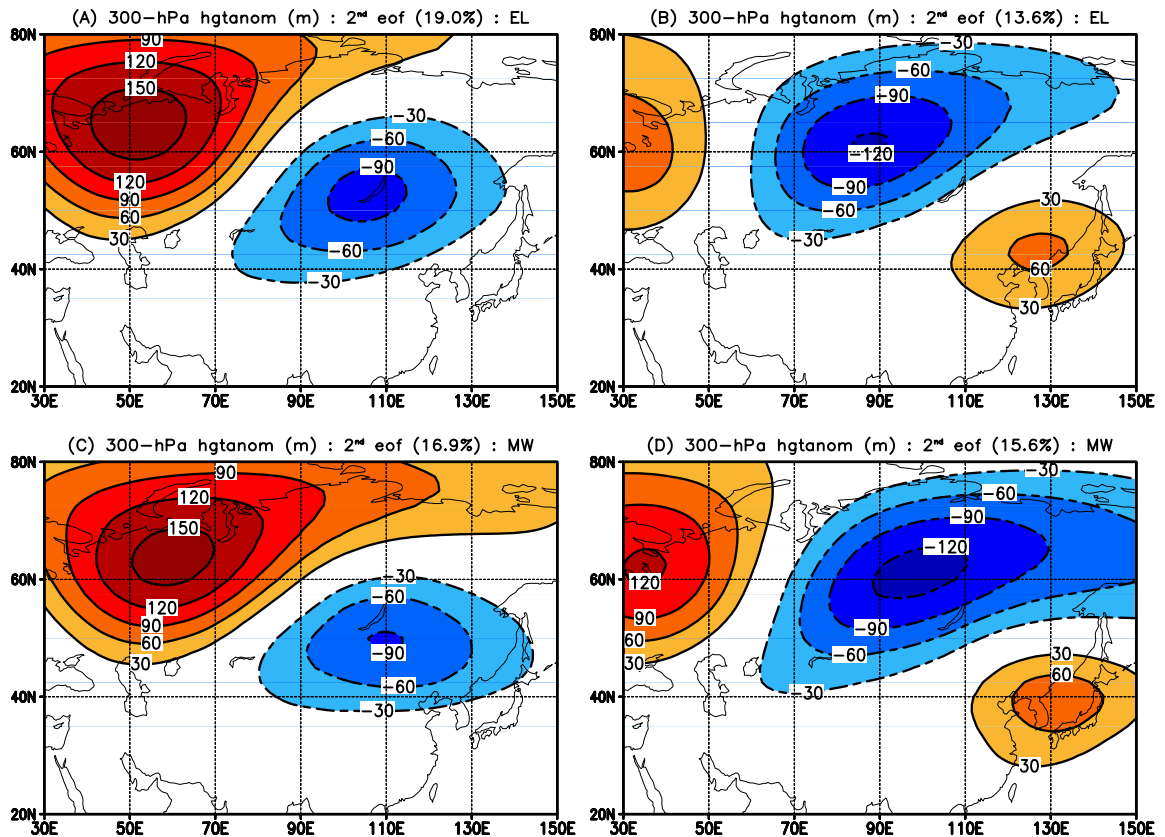


Figure 36: The first two EOF patterns of the 300 hPa geopotential height anomalies (shaded contour intervals: 30 m) over Asia for (a)–(b) EL and (c)–(d) MW. The percent variance associated with each EOF pattern is provided.

positive phase of the EOF indices are designated as the patterns shown in Fig. 36). This indicates that the midwinter Siberian low-frequency anomaly from our regression analysis is a principal mode of variability over Asia and plays a relatively enhanced role during midwinter.

One way to utilize the Siberian indices involves partitioning the indices into (i) positive and (ii) negative phases and plotting the probability distribution function (PDF) of the normalized synoptic-eddy amplitude in the Pacific storm track core for various positive lags. For EL and MW, the PDF's for the positive and negative phase of the PS index are plotted in Figure 37. The blue line with diamonds (red line) represents the PDF of synoptic-eddy amplitude for 5–8 days *after* observing a positive (negative) value of the PS index. Comparing MW from EL, there is typically a slightly higher probability of observing large-magnitude events in the Pacific storm track at 5–8 days following a positive value of

the PS index during MW.

The PDF plots imply a relationship between the phase of the PS index and the magnitude of cyclones *and* anticyclones in the Pacific storm track. However there are two issues arise from using the PDFs: (i) An uncertainty exists from potentially multi-sampling from cyclones and anticyclones within the same baroclinic wave packet, (ii) What is the significance of the difference between the two curves during MW? Thus at this point instead of focusing on individual cyclones or anticyclones, we now pursue further statistical analyses using the envelope function anomaly to depict the level of baroclinic wave activity relative to its seasonal mean. The envelope function incorporates cyclones and anticyclones into distinguishable, coherent wave packets (Nakamura & Wallace, 1990). We now employ a combination of Monte Carlo and hypothesis testing to assess the relationship between anomalously strong baroclinic wave activity in the Pacific storm track and the value of the PS and E2 indices beforehand.

An array of dates is defined when the envelope function anomaly in the core of the storm track exceeds zero. Preceding these dates, we create a distribution of the Siberian indices at different lags. We want to test if a certain phase of the Siberian indices tend to precede increased baroclinic wave activity in the storm track. We compare the "lagged" distribution of the Siberian indices with another distribution of Siberian indices created by randomly selecting dates.

As an example, Figure 39 displays a histogram of the PS index one week before increased levels of baroclinic wave activity during MW. The red line represents a least-squares Gaussian fit to the histogram of the PS index based upon randomly selected dates. A hypothesis test of the two distributions is conducted, where the null hypothesis (H_0) is defined as no difference between the two sample means. A two-tailed t-test determines the p-value, and if the p-value is less than 0.01, H_0 is rejected. $H_0 = 1$ ($H_0 = 0$) indicates that the null hypothesis is (not) rejected. In this case, $H_0 = 1$, suggesting there is a difference between the two distributions with 99% confidence.

Instead of assuming a normal distribution of Siberian indices based upon randomly selected dates, we repeat this process 1000 times and compute the percentage null hypothesis

rejection. In the example, the average PS index at 7 days preceding anomalously enhanced levels of baroclinic wave activity during MW is 0.205. For 1000 scenarios, this mean value is greater than that derived from randomly selected dates every single time (99th percentile).

The same procedure is applied for the PS and E2 indices at various lags during EL and MW. The observed mean Siberian indices and the percentage of null hypothesis rejection for each case are displayed in Table 10. For the PS index, rejections greater than 95% are observed for Days -8 to -1 (and extends to +1, but is not shown). For the E2 index, Days -9 to -5 exceed 95% rejection. We conclude with higher certainty that during MW, there is a unique relationship between increased levels of baroclinic wave activity and the value of the Siberian indices beforehand.

Constructing composite maps based upon values of the Siberian indices help illustrate the associated changes in the structure and magnitude of the Pacific storm track. The PS and E2 indices are partitioned into three categories: (i) index values $\leq -1\sigma$, (ii) values between $\pm 1\sigma$, and (iii) index values $\geq +1\sigma$. Since the indices are primarily associated with low-frequency patterns, we composite the envelope function, which depicts the low-frequency amplitude modulation of baroclinic wave packets.

For EL and MW, composite maps of the envelope function at 5–8 days following certain partitioned values of the PS index are illustrated in Figure 40. For values $\geq +1\sigma$ (Figs. 40a,b), positive anomalies exist in the entrance region of the climatological storm track during EL and MW, with slightly larger enhancements during MW. Figs. 40c,d illustrate the composite envelope function anomaly during EL and MW for PS index values $\leq -1\sigma$. In both stages negative anomalies exist over the northern part of the storm track, however the MW anomalies much more enhanced. Composites for PS index values between -1σ and $+1\sigma$ show only a slight enhancement the storm track core during MW and no patterns in EL (Figs. 40e,f).

Composites based upon the value of the E2 show fairly symmetrical and more distinct patterns in Figure 41. There is a clear northeastward (southeastward) shift in the storm track for E2 index values $\geq +1\sigma$ ($\leq -1\sigma$) that is relatively enhanced during MW. The shift in the storm track associated with the phase of the E2 index are indicative of the

Monte Carlo Results for Pacific storm track : Envelope Function Anomalies > 0

(a) PS Index

Early and Late Stages			Midwinter		
Date	Percentile	Sample Mean	Date	Percentile	Sample Mean
-10	1 st	-0.056	-10	90 th	+0.126
-9	1 st	-0.044	-9	98 th	+0.148
-8	1 st	-0.041	-8	99 th	+0.180
-7	1 st	-0.034	-7	99 th	+0.205
-6	1 st	-0.026	-6	99 th	+0.217
-5	2 nd	-0.019	-5	99 th	+0.218
-4	2 nd	-0.010	-4	99 th	+0.208
-3	3 rd	-0.004	-3	99 th	+0.191
-2	6 th	+0.004	-2	99 th	+0.167
-1	14 th	+0.018	-1	98 th	+0.151

(b) E2 Index

Early and Late Stages			Midwinter		
Date	Percentile	Sample Mean	Date	Percentile	Sample Mean
-10	3 rd	-0.022	-10	92 nd	+0.137
-9	6 th	-0.031	-9	96 th	+0.149
-8	4 th	-0.015	-8	98 th	+0.158
-7	2 nd	-0.012	-7	98 th	+0.161
-6	1 st	-0.016	-6	98 th	+0.158
-5	1 st	-0.008	-5	96 th	+0.148
-4	1 st	-0.005	-4	94 th	+0.137
-3	1 st	-0.004	-3	87 th	+0.123
-2	1 st	-0.002	-2	60 th	+0.095
-1	1 st	+0.010	-1	23 rd	+0.064

Table 10: Monte Carlo results during EL and MW for the value of the (a) P2 and (b) E2 indices for selected lags from days with anomalously enhanced levels of baroclinic wave activity. The percentiles are compiled from 1000 cases of hypothesis testing, where the null hypothesis assumes no difference between the selected mean and a random sample mean of the indices. The null hypothesis is rejected with 99% confidence and the percentile represents the percent of cases in which the null hypothesis is rejected.

cyclonic/anticyclonic wave breaking in the Pacific jet exit region (Orlanski, 2003).

5.4 Summary

We perform an observational lag regression analysis to study seasonal variations in the upstream evolution of upper tropospheric Rossby wave packets traversing Asia prior to strong cyclogenesis events in the North Pacific storm track. During early and late stages of the cool season (EL - when North Pacific storm track is strongest), coherent precursor synoptic scale wave packets can be traced upstream to the northern branch of the Asian waveguide as early as 7 days prior to Pacific cyclogenesis (Day -7). There is no evidence that the southern branch plays an important role in the EL events. Our results are quite different from midwinter (MW), which is initially characterized by a large-scale low frequency cyclonic anomaly over Siberia at Day -7. Synoptic wave packets subsequently emerge from along both the north and south branches of the Asian waveguide. These three anomaly features then merge at Day -3 to form the necessary upper tropospheric precursor to MW Pacific cyclogenesis events.

Further analyses reveal a general dampening of synoptic eddy amplitudes along the northern branch of the Asian waveguide during MW, which may be a primary contributing factor to the midwinter suppression phenomenon. We created two indices representing large-scale patterns of variability over Asia. One index was derived solely from an upper-tropospheric anomaly feature over Siberia, while the second index represented the second EOF of height variability in the upper-troposphere. A number of statistical tests were employed to further demonstrate that changes in the level of baroclinic wave activity in the midwinter Pacific storm track are indeed preceded by certain large-scale low frequency patterns over Asia. Specifically, a strong low-frequency anticyclone (cyclone) is present over Siberia one week prior to relatively large reductions (slight enhancements) in the Pacific storm track.

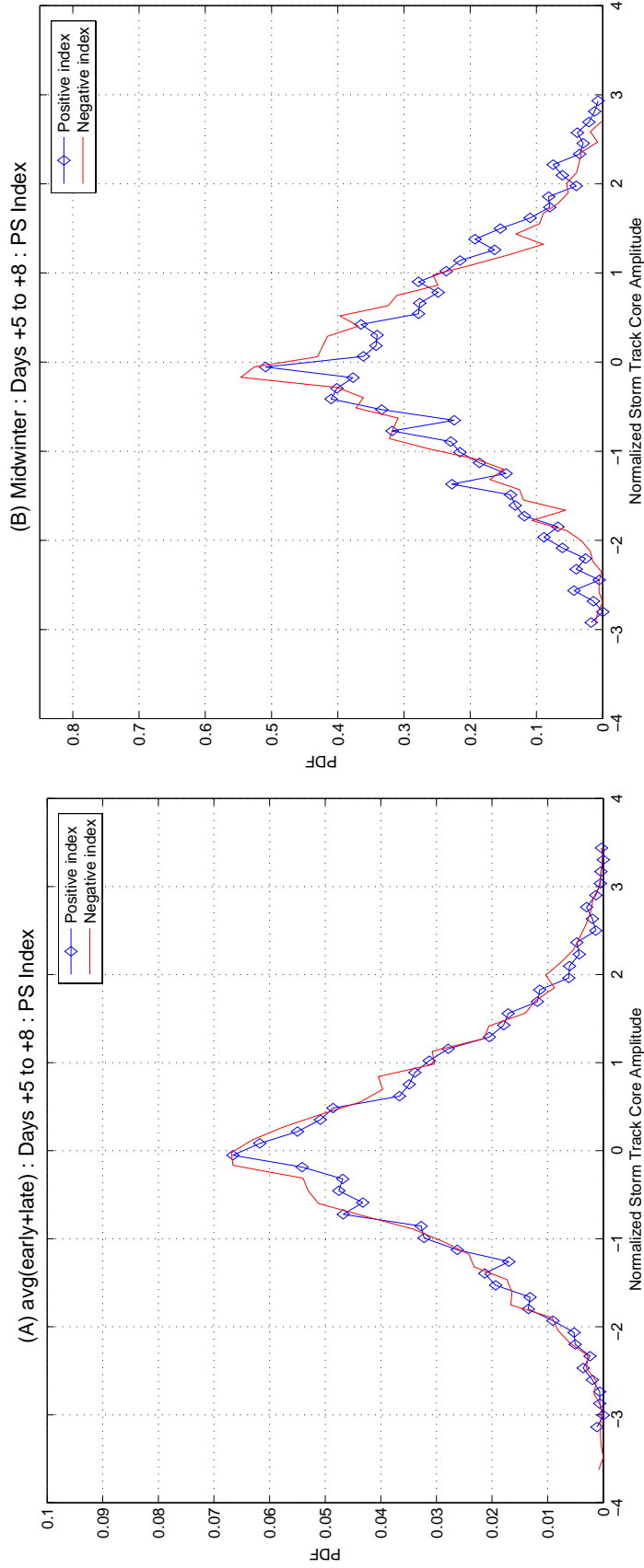


Figure 37: The probability distribution function of the standardized highpass-filtered geopotential height anomaly in the core of the Pacific storm track for 5–8 days after positive (blue line with diamonds) and negative (red line) values of the PS index for (a) EL and (b) MW. The PS index is derived by projecting the Day -7 low-frequency pattern in Figure 32b onto the unfiltered geopotential height anomaly field over Asia.

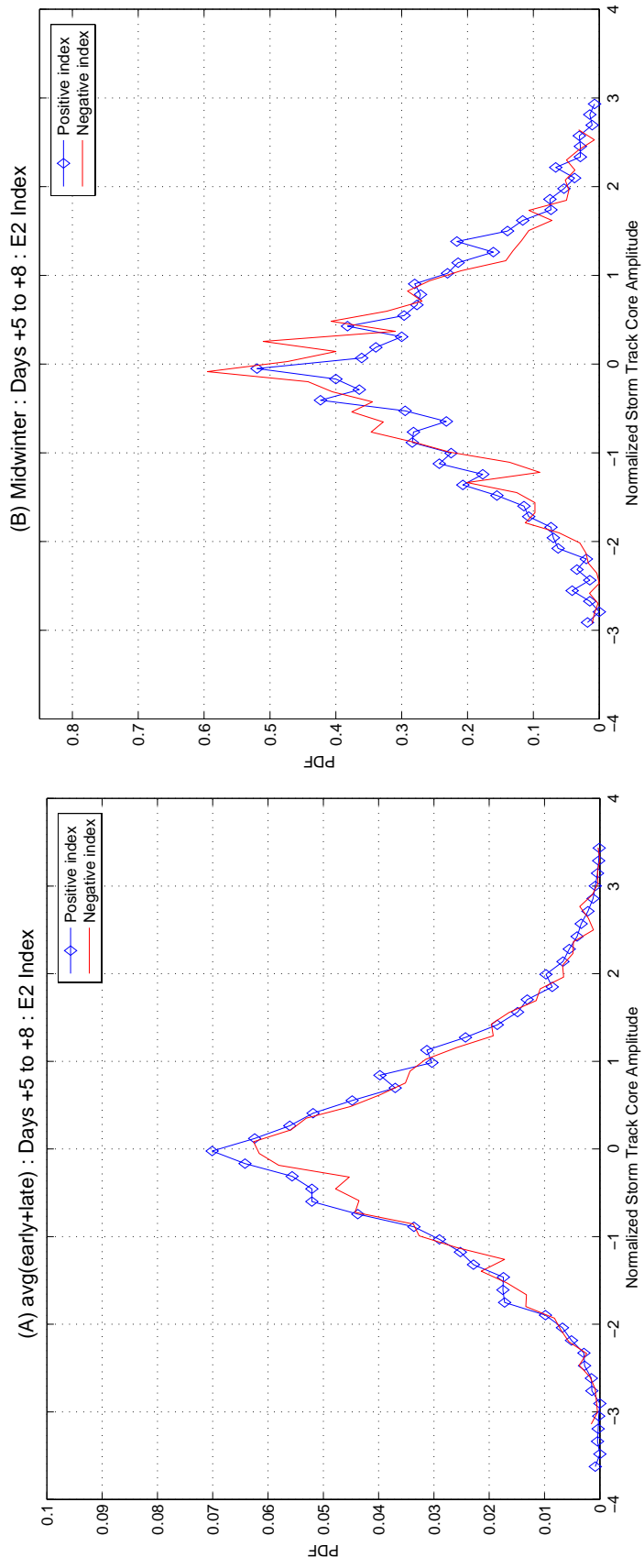


Figure 38: As in Figure 37 but for the E2 index. The E2 index is derived from the second EOF of unfiltered geopotential height anomaly over Asia.

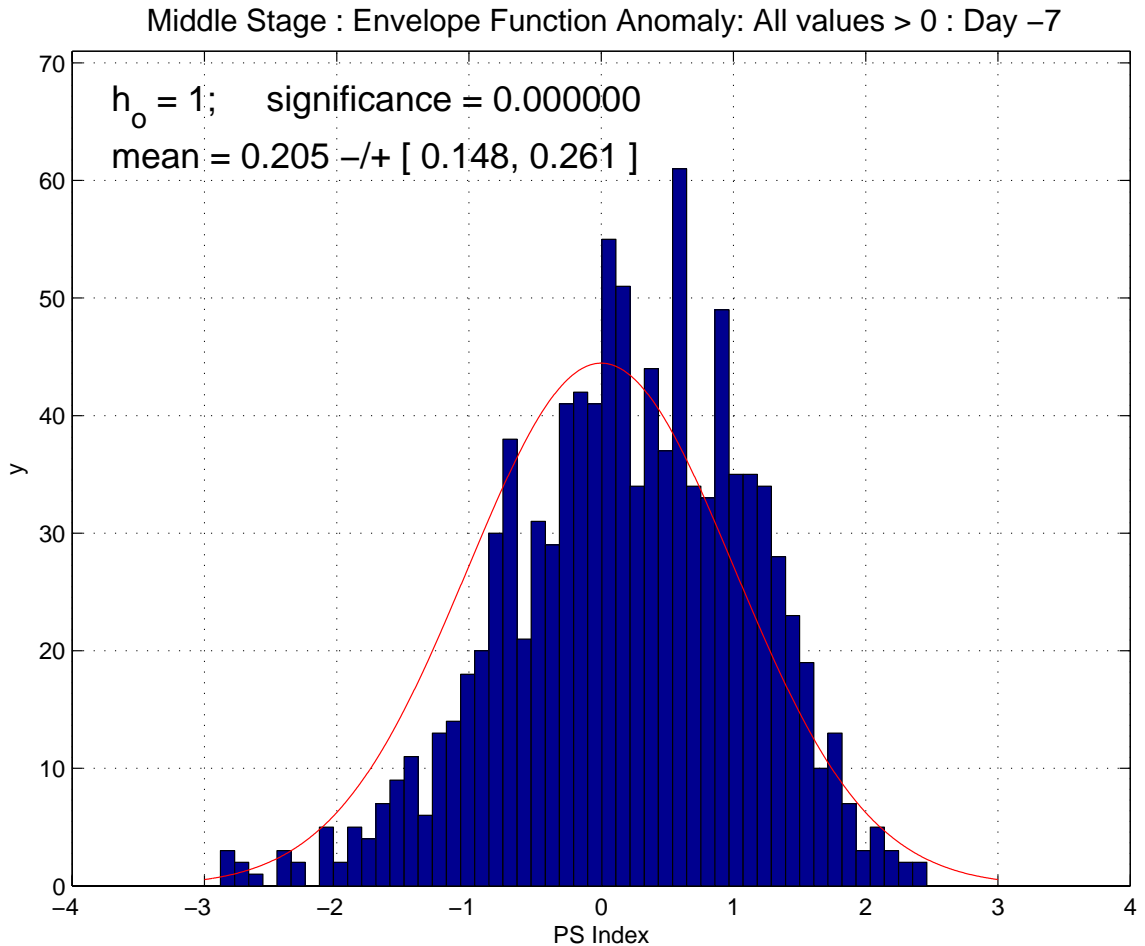


Figure 39: A histogram representing each days when the envelope function anomaly in the core of the MW storm track is greater than zero distributed over values of the PS index preceding the events by one week. The red curve represents a least-squares Gaussian fit to the histogram of the PS index based upon randomly selected dates. A null hypothesis (H_0) is defined as no difference between the mean of the two curves. In this case, the null hypothesis is rejected ($H_0 = 1$) with 99% confidence (significance α 0.01). The sample mean and 99% confidence levels are listed.

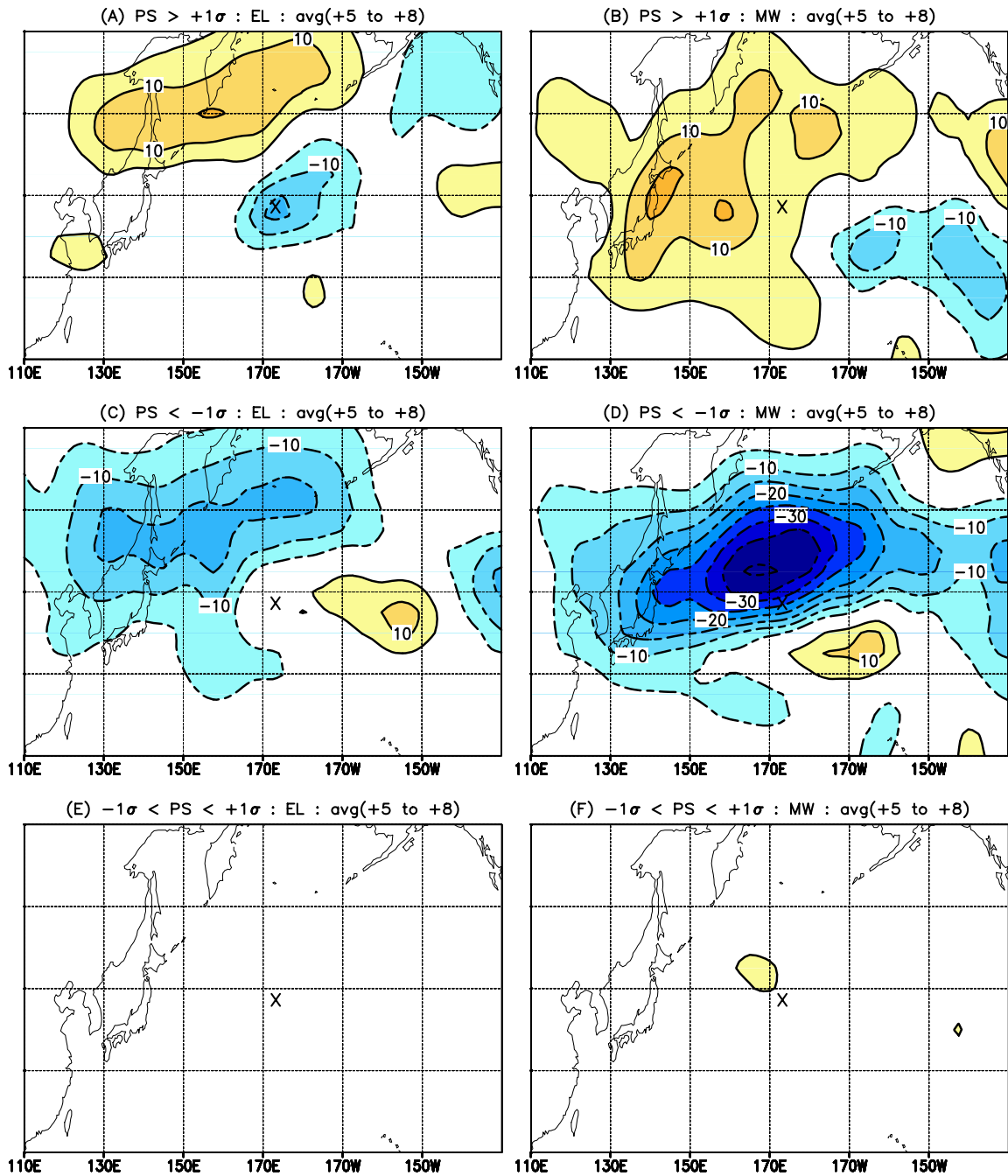


Figure 40: Composite maps of the 300 hPa envelope function anomaly (shaded contour intervals: $10^3 m^2$ during EL (left column) and MW (right column) for values of the P2 index values (a)–(b) $\geq 1\sigma$, (c)–(d) $\leq -1\sigma$, and (e)–(f) between $\pm 1\sigma$. For reference, core values of the Pacific storm track are approximately $140 \times 10^3 m^2$ depending on the stage of the cool season.

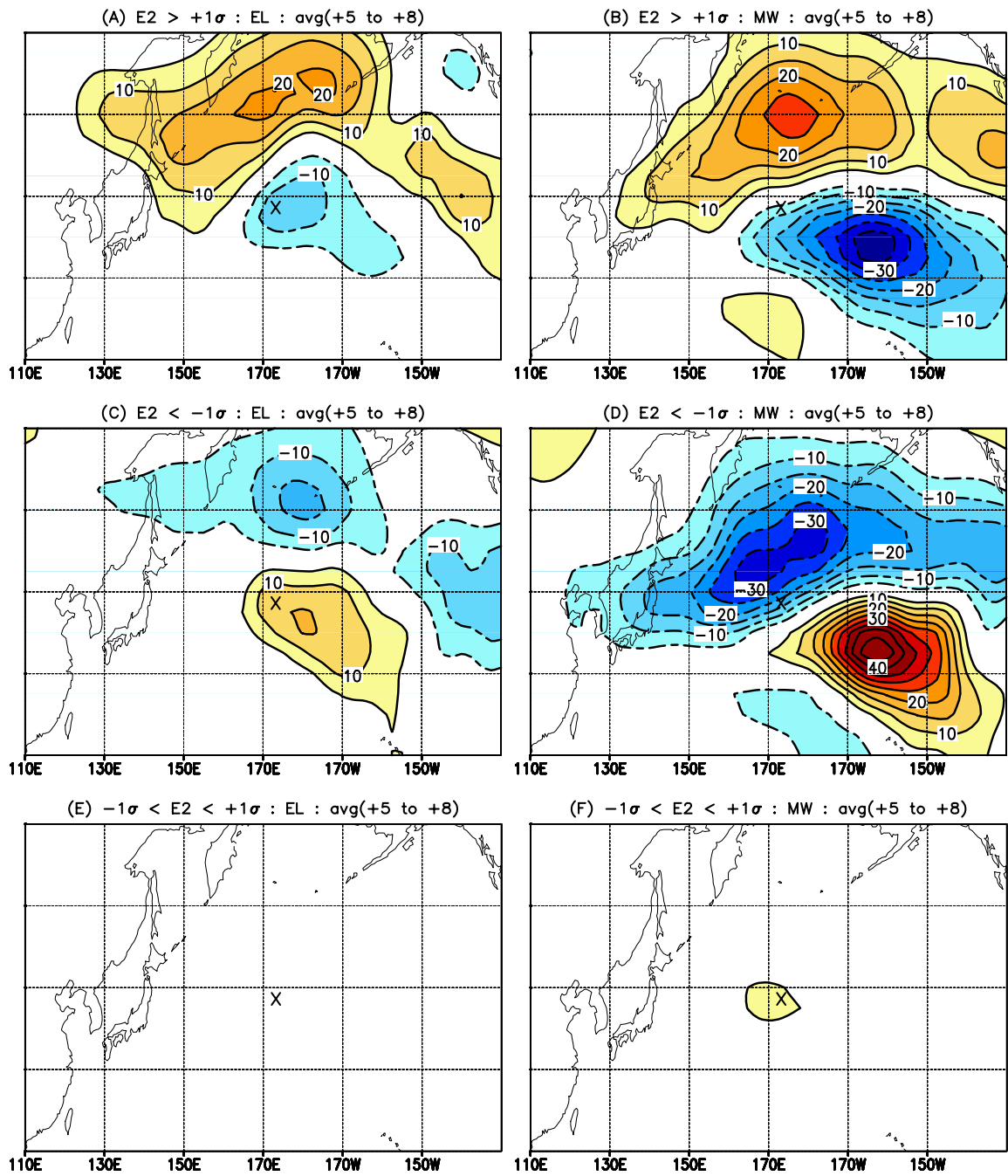


Figure 41: As in Figure 40 except for the E2 index.

CHAPTER VI

CONCLUSION AND CLOSING REMARKS

We used a broad suite of diagnostic methods to study the strengths and weaknesses of NASA GSFC GCMs in the simulation of subseasonal midlatitude variability. The winter-averaged statistics, three-dimensional structure, and dynamical features of storm tracks and large-scale weather regimes were examined in long-term GCM simulations and compared to parallel results derived from the NCEP-NCAR reanalyses dataset spanning the same multiyear time period. We also performed comparative diagnostic analyses of developing baroclinic disturbances upstream the Pacific and Atlantic storm tracks in observations and NASA GSFC GCM simulations.

Discrepancies are observed in the magnitude and location of the planetary stationary waves and climatological jet streams. The Pacific stationary ridge is anomalously strong (weak) in the NSIPP (NASCAR) simulation. In both models, this feature is shifted westward relative to observations with a corresponding upstream shift in the location of the Pacific jet exit region. We also note over the Atlantic region, the stationary ridges are well positioned but anomalously strong (weak) in the NASCAR (NSIPP) model. For the NASCAR model, the magnitude of the maximum zonal wind in the jet core regions are slightly larger than observations, while the local zonal wind maxima in the NSIPP model are typically 5–10 $m \cdot sec^{-1}$ greater in the core of the Pacific and Atlantic jets.

Profiles of the areally-averaged eddy kinetic energy illustrate that levels of subseasonal eddy activity in the GCMs are relatively weak throughout the mid- to upper-troposphere, particularly for synoptic-scale eddies. These deficiencies are also reflected in the magnitude of the simulated storm tracks. One notable discrepancy in the climatological storm track structure in both GCM simulations is the relative minimum that occurs over the eastern Pacific basin. This feature is attributed to a westward displacement and relative localization of the climatological barotropic deformation field in the model simulations [consistent with

the results of Black & Dole (2000)]. Though anomalously weak, the structure of the Atlantic storm track is much better represented by both GCMs.

Despite anomalously weak storm tracks, the GCMs successfully reproduce the North Pacific midwinter suppression, while the NSIPP model produces a midwinter suppression over the Atlantic storm track region. During midwinter, the magnitudes of the Atlantic jet core in the NSIPP model actually exceed $45 \text{ m} \cdot \text{sec}^{-1}$, the "threshold" of baroclinic development reported by Nakamura (1992). Thus, the GCMs faithfully reproduce the observed non-linear relationship between synoptic eddy activity and zonal wind speeds in the upper-troposphere.

These results confirm that the GCMs considered in the current study do a good job in simulating various intraseasonal aspects of the storm tracks. However, they also demonstrate the critical importance of properly representing the magnitude and structure of the basic-state flow field, especially regarding the $45 \text{ m} \cdot \text{sec}^{-1}$ threshold associated with baroclinic development. With anomalously strong zonal winds in the upper-troposphere (especially over the Pacific region), we posit that the anomalously weak storm tracks in the GCMs are attributed to relatively extended periods throughout the boreal winter when upper-tropospheric wind speeds exceed $45 \text{ m} \cdot \text{sec}^{-1}$.

With relatively extended periods of suppressed baroclinic wave activity, lower-frequency modes in the GCMs play a relatively larger role in the meridional transport of heat. This is illustrated in the composite results of persistent flow anomalies (PFAs) in the eastern Pacific of the GCMs. Three-dimensional structure analyses of Pacific PFAs indicate that model simulated anomaly structures are distinctly different from observed structures. Specifically, the composite PFA structures in the model simulations are markedly more horizontally isotropic and have greater westward vertical anomaly tilts. A qualitative analysis of energy conversions reveals that baroclinic (barotropic) interactions provide anomalously strong (weak) contributions toward the maintenance of simulated PFA events over the North Pacific.

Diagnostic analyses of the North Pacific storm track employed a novel seasonal stratification technique in order to isolate the period of midwinter suppression of synoptic eddy

activity. Composite structural analyses reveal that the most apparent difference between midwinter and early winter and late winter periods is that the *magnitude* of the growing cyclonic anomalies is weaker during midwinter. Thus during the midwinter suppression period, cyclonic perturbations entering the North Pacific storm track core are deficient in magnitude compared to early and late winter stages. We find that the North Pacific midwinter suppression feature, in both observations and model simulations, has a clear organized extension upstream into Siberia, the region from which the key upper-tropospheric short-wave features are believed to emanate (Hakim, 2003). Further, similar upstream behavior is observed in association with the parallel midwinter suppression of the North Atlantic storm track that is (erroneously) simulated in the NSIPP model (see 3.2.2).

The final portion of this work pursued to determine an upstream origin of the North Pacific midwinter suppression phenomenon. This was approached with an observational lag regression analysis studying intraseasonal variations in the behavior of upper tropospheric Rossby wave packets prior to strong cyclogenesis events in the North Pacific storm track. During the early and late stages of the boreal cool season, strong Pacific cyclogenesis is preceded by coherent synoptic scale wave packets that can be traced upstream to the northern branch of the Asian waveguide a week in advance. Our results are quite different from midwinter (MW), which is initially characterized by a large-scale low frequency cyclonic anomaly over Siberia at Day -7 (one week preceding cyclogenesis in the Pacific storm track core). Synoptic wave packets subsequently emerge from along both the north and south branches of the Asian waveguide. These three anomaly features then merge at Day -3 to form the necessary upper tropospheric precursor to MW Pacific cyclogenesis events. Conversely, the presence of a large-scale anticyclone over Siberia is followed by a significant area decrease in baroclinic wave activity over the Pacific storm track. This suppression in the Pacific storm track occurs beyond the range of synoptic variability (5–8 days).

Our result provides a "cause" to associated changes in the background flow field that eventually inhibit the growth of baroclinic waves during midwinter. Specifically, an anticyclone over Siberia intensifies the East Asian monsoon resulting in a deepening of the

planetary-wave trough coupled with a strengthening, narrowing, and southward shift in the observed East Asian jet. While the anticyclone inhibits upper-level wave packets along the northern branch, wave packets along the southern branch play a relatively enhanced role in seeding midwinter Pacific cyclogenesis events. Following the mechanistic proposal of Nakamura & Sampe (2002), the "subtropical" Pacific jet suppresses baroclinic growth by trapping the upper-level anomalies and weakening its interaction with the surface baroclinic zone. Thus during midwinter, we find an increased sensitivity of synoptic-scale wave packets with a large-scale flow pattern in the upper-troposphere over Siberia. This interaction with the large-scale pattern over Siberia results in a general dampening of synoptic eddy amplitudes along the northern branch of the Asian waveguide, which is proposed to be the contributing factor to the midwinter suppression phenomenon.

This "upstream weakening" hypothesis can be applied to the ensemble representation of synoptic eddies in the GCMs. The relative weakness in the amplitude of synoptic eddies in the storm track regions may be due to a relative weakness in the amplitudes of upper-level perturbations prior to entering the baroclinic zone in the simulated storm track regions. This discrepancy in upstream seeding in the models may ultimately be linked to relatively enhanced interactions of the upper-level wave packets with large-scale flow patterns over the continental regions. Perhaps this increased sensitivity is related to the anomalously cold temperatures observed in the high latitude regions in the models. The result is an extended "midwinter" scenario in the models, which leads to prolonged suppressions in baroclinic wave activity. Thus, we suggest that improving errors in the GCMs rely on improved simulation of the polar temperatures (More specific improvements on the polar climate simulation merits more extensive analyses focused on the high latitudes as in Briegleb & Bromwich, 1998).

Further, the "upstream" insight into the North Pacific midwinter suppression enhances the understanding of dynamic interactions not only for intraseasonal temporal scales but potentially for interannual to decadal time scales (e.g., Clark & Serreze, 2000; Chang, 2001; Nakamura *et al.*, 2002; Orlanski, 2005). We find significant shifts in the storm tracks associated with the large-scale Siberian patterns. These patterns may affect how synoptic eddies

ultimately decay over the eastern Pacific, impacting the phase of the Pacific–North American teleconnection pattern. Clearly this is a topic of interest for future work. It will also be of interest to conduct further analyses on (i) the upstream circulation features identified in our study, particularly the development of midwinter Siberian patterns, (ii) their dynamical interactions with upper-level wave packets, and (iii) examine why there is increased sensitivity of baroclinic wave activity to the upstream anomaly during midwinter.

Bibliography

- BLACK, R.X. 1990. *A diagnostic study of the life cycles of persistent flow anomalies*. PhD Dissertation, Massachusetts Institute of Technology, Department of Earth, Atmospheric, and Planetary Sciences.
- BLACK, R.X., & DOLE, R.M. 2000. Storm tracks and barotropic deformation in climate models. *Journal of Climate*, **13**, 2712–2728.
- BLACK, R.X., & EVANS, K.J. 1998. The statistics and horizontal structure of anomalous weather regimes in the Community Climate Model. *Monthly Weather Review*, **126**, 841–859.
- BLACKMON, M.L. 1976. A climatological spectral study of the 500 mb geopotential height of the Northern Hemisphere. *Journal of Atmospheric Sciences*, **33**, 1379–1405.
- BLACKMON, M.L., WALLACE, J.M., LAU, N.-C., & MULLEN, S.L. 1977. An observational study of the Northern Hemisphere wintertime circulation. *Journal of Atmospheric Sciences*, **34**, 1040–1053.
- BRANSTATOR, G. 1992. The maintenance of low-frequency atmospheric anomalies. *Journal of the Atmospheric Sciences*, **49**, 1924–1945.
- BRIEGLEB, B.P., & BROMWICH, D.H. 1998. Polar climate simulation of the NCAR CCM3. *Journal of Climate*, **11**, 1270–1286.
- CARLSON, T. N. 1998. *Mid-latitude Weather Systems*. Boston, Massachusetts: American Meteorological Society. Chap. 11, pages 265–283.
- CHANG, E.K.M. 1993. Downstream development of baroclinic waves as inferred from regression analysis. *Journal of Atmospheric Sciences*, **50**, 2038–2053.
- CHANG, E.K.M. 2001. GCM and observational diagnoses of the seasonal and interannual variations of the Pacific storm track during the cool season. *Journal of Atmospheric Sciences*, **58**, 1784–1800.
- CHANG, E.K.M. 2005. The impact of wave packets propagating across Asia on Pacific cyclone development. *Monthly Weather Review*, **133**, 1998–2015.
- CHANG, E.K.M., & FU, Y. 2002. Interdecadal variations in Northern Hemisphere winter storm track intensity. *Journal of Climate*, **15**, 642–658.
- CHANG, E.K.M., & YU, D.B. 1999. Characteristics of wave packets in the upper troposphere. Part I: Northern Hemisphere Winter. *Journal of Atmospheric Science*, **56**, 178–1728.
- CHANG, E.K.M., LEE, S., & SWANSON, K.L. 2002. Storm track dynamics. *Journal of Climate*, **15**, 2163–2183.
- CHARNEY, J.G. 1947. The dynamics of long waves in a baroclinic westerly current. *Journal of Meteorology*, **4**, 135–163.

- CHEN, W.Y. 1981. Fluctuations in northern hemisphere 700 mb height field associated with the Southern Oscillation. *Monthly Weather Review*, **110**, 808–823.
- CHEN, W.Y., & VAN DEN DOOL, H. 2003. Sensitivity of teleconnection patterns to the sign of their primary action center. *Monthly Weather Review*, **131**, 2885–2899.
- CHENG, X., & WALLACE, J.M. 1993. Cluster analysis of the Northern Hemisphere wintertime 500-hPa height field: spatial patterns. *Journal of the Atmospheric Sciences*, **50**, 2674–2696.
- CHRISTOPH, M., ULBRICH, U., & SPETH, P. 1997. Midwinter suppression of Northern Hemisphere storm track activity in the real atmosphere and in GCM experiments. *Journal of Atmospheric Sciences*, **54**, 1589–1599.
- CLARK, M.P., & SERREZE, M.C. 2000. Effects of variations in East Asian snow cover on modulating atmospheric circulation over the North Pacific ocean. *Journal of Climate*, **13**, 3700–3710.
- DOLE, R.M. 1986. Persistent anomalies of the extratropical Northern Hemisphere wintertime circulation: Structure. *Monthly Weather Review*, **114**, 178–207.
- DOLE, R.M., & BLACK, R.X. 1990. Life cycles of persistent anomalies. Part II: The development of persistent negative height anomalies over the North Pacific Ocean. *Monthly Weather Review*, **118**, 824–846.
- DOLE, R.M., & GORDON, N.D. 1983. Persistent anomalies of the extratropical Northern Hemisphere circulation: Geographical distribution and regional persistence characteristics. *Monthly Weather Review*, **111**, 1567–1586.
- EADY, E.T. 1949. Long waves and cyclone waves. *Tellus*, **1**, 33–52.
- EVANS, K.J. 2000. *A quantitative analysis of the physical mechanisms governing the life cycles of persistent flow anomalies*. PhD Dissertation, Georgia Institute of Technology, Department of Earth and Atmospheric Sciences.
- FARRELL, B.F. 1989. Transient development in confluent and diffluent flow. *Journal of the Atmospheric Sciences*, **46**, 3279–3288.
- FUENZALIDA, H., & ROSENBLÜTH, B. 1990. Prewhitening of climatological time series. *Journal of Climate*, **3**, 382–393.
- HAKIM, G.J. 2003. Developing wave packets in the North Pacific storm track. *Monthly Weather Review*, **131**, 2824–2837.
- HARTMANN, D. L. 1974. Time spectral analysis of mid-latitude disturbances. *Monthly Weather Review*, **102**, 348–362.
- HIGGINS, R.W., & SCHUBERT, S.D. 1994. Simulated life cycles of persistent anticyclonic anomalies over the North Pacific: Role of synoptic-scale eddies. *Journal of Atmospheric Sciences*, **51**, 3238–3260.
- HOSKINS, B.J., JAMES, I.N., & WHITE, G.H. 1983. The shape, propagation and mean-flow interaction of large-scale weather systems. *Journal of Atmospheric Sciences*, **40**, 1595–1612.

- KALNAY, E., & COAUTHORS. 1996. The NCEP/NCAR 40-Year Reanalysis Project. *Bulletin of the American Meteorological Society*, **77**, 437–471.
- KAUROLA, J. 1997. Some diagnostics of the northern wintertime climate simulated by the ECHAM3 model. *Journal of Climate*, **10**, 201–222.
- KUSHNIR, Y., ROBINSON, W.A., BLADE, I., HALL, N.M.J., PENG, S., & SUTTON, R. 2002. Atmospheric GCM response to extratropical SST anomalies: Synthesis and evaluation. *Journal of Climate*, **15**, 2233–2256.
- L. KUO, H. 1949. Dynamic instability of two-dimensional nondivergent flow in a barotropic atmosphere. *Journal of Atmospheric Sciences*, **6**, 105–122.
- LAU, N.-C. 1988. Variability of the observed midlatitude storm tracks in relation to low-frequency changes in the circulation pattern. *Journal of Atmospheric Sciences*, **45**, 2718–2498.
- LEE, S., & KIM, H.-K. 2003. The dynamical relationship between subtropical and eddy-driven jets. *Journal of Atmospheric Sciences*, **60**, 1490–1503.
- LIM, G.H., & WALLACE, J.M. 1991. Structure and evolution of baroclinic waves as inferred from regression analysis. *Journal of Atmospheric Sciences*, **48**, 1718–1732.
- LIN, S.-J., & ROOD, R.B. 1997. An explicit flux-form semi-Lagrangian shallow water model on a sphere. *Quarterly Journal of the Royal Meteorological Society*, **123**, 2477–2498.
- LIVEZEY, R.E., & CHEN, W.Y. 1983. Statistical field significance and its determination by Monte Carlo techniques. *Monthly Weather Review*, **111**, 46–59.
- MAK, M., & CAI, M. 1989. Local barotropic instability. *Journal of the Atmospheric Sciences*, **46**, 3289–3311.
- MARTIN, J.E., GRAUMAN, R.D., & MARSILI, N. 2001. Surface cyclolysis in the North Pacific Ocean. Part I: A synoptic climatology. *Monthly Weather Review*, **129**, 748–765.
- NAKAMURA, H. 1992. Midwinter suppression of baroclinic wave activity in the Pacific. *Journal of Atmospheric Sciences*, **49**, 1629–1642.
- NAKAMURA, H., & SAMPE, T. 2002. Trapping of synoptic-scale disturbances into the North Pacific subtropical jet core in midwinter. *Geophysical Research Letters*, **29**, 1761, doi:10.1029/2002GL015335.
- NAKAMURA, H., & WALLACE, J.M. 1990. Observed changes in baroclinic wave activity during the life-cycles of low-frequency circulation anomalies. *Journal of Climate*, **15**, 1100–1116.
- NAKAMURA, H., & WALLACE, J.M. 1993. Synoptic behavior of baroclinic eddies during the blocking onset. *Monthly Weather Review*, **121**, 1892–1903.
- NAKAMURA, H., IZUMI, T., & SAMPE, T. 2002. Interannual and decadal modulations recently observed in the Pacific storm track activity and East Asian winter monsoon. *Journal of Climate*, **15**, 1855–1874.
- ORLANSKI, I. 1998. Poleward deflection of storm tracks. *Journal of Atmospheric Sciences*, **55**, 2577–2602.

- ORLANSKI, I. 2003. Bifurcation in eddy life cycles: implications for storm track variability. *Journal of Atmospheric Sciences*, **60**, 993–1023.
- ORLANSKI, I. 2005. A new look at the Pacific storm track variability: sensitivity to tropical SSTs and to upstream seeding. *Journal of Atmospheric Sciences*, **62**, 1367–1390.
- ORLANSKI, I., & KATZFEY, J. 1991. The life-cycle of a cyclone wave in the southern hemisphere. Part I: eddy energy budget. *Journal of Atmospheric Sciences*, **48**, 1972–1998.
- ROTUNNO, R., MURAKI, D.J., & SNYDER, C. 2000. Unstable baroclinic waves beyond quasi-geostrophic theory. *Journal of Atmospheric Sciences*, **57**, 3285–3295.
- SIMMONS, A.J., WALLACE, J., & BRANSTATOR, G. 1983. Barotropic wave propagation and instability, and atmospheric teleconnection patterns. *Journal of Atmospheric Sciences*, **40**, 1363–1392.
- SUAREZ, M., & TAKACS, L. 1995. Documentation of the Aries/GEOS Dynamical Core Version 2. Page 46 pp of: CENTER, NASA/GODDARD SPACE FLIGHT (ed), *NASA Technical Memo. 104606, Vol. 4*. Greenbelt, MD: NASA/Goddard Space Flight Center.
- TRENBERTH, K.E. 1991. Storm tracks in the Southern Hemisphere. *Journal of Atmospheric Sciences*, **48**, 2159–2178.
- WALLACE, J. M., & HOBBS, P. V. 1977. *Atmospheric Science: An Introductory Survey*. San Diego, California: Academic Press. Chap. 9, pages 412–450.
- WALLACE, J.M., & GUTZLER, D.S. 1981. Teleconnections in the geopotential height field during the Northern Hemisphere winter. *Monthly Weather Review*, **109**, 784–812.
- WALLACE, J.M., LIM, G.-H., & BLACKMON, M.L. 1988. Relationship between cyclone tracks, anticyclone tracks and baroclinic waveguides. *Journal of Atmospheric Sciences*, **45**, 439–462.
- WHITAKER, J.S., & DOLE, R.M. 1995. Organization of storm tracks in zonally varying flows. *Journal of Atmospheric Sciences*, **52**, 1178–1191.
- ZHANG, Y., & HELD, I.M. 1999. A linear stochastic model of a GCM's midlatitude storm tracks. *Journal of Atmospheric Sciences*, **56**, 3416–3435.